A High-Resolution Radio Continuum Study of the Dwarf Irregular Galaxy IC10

Jonathan Westcott

A report submitted in partial fulfilment of the requirements of the University of Hertfordshire for the degree of Master of Science by Research

This programme of research was carried out in the Centre for Astrophysics Research, School of Physics, Astronomy and Mathematics, University of Hertfordshire

October 2014

Project Supervisors: Prof Elias Brinks & Dr Robert Beswick

Acknowledgments

I would like to express my thanks to those who have supported me throughout the course of this MSc project. Especially thanks to Prof Elias Brinks for all of the time spent showing me the basics of interferometry, calibration and radio astronomy and for the time spent helping me to write and proof read the thesis.

I would also like to thank the staff at the University of Manchester Physics department and the staff at Jodrell bank for their help in teaching me the calibration process for e-MERLIN, especially Dr Robert Beswick and Dr Pierre Emmanuelle-Belles for their time and hospitality at a busy time of year.

Finally I would like to thank Dr Brian May for awarding me the Brian May scholarship, without which I would not have been able to complete this thesis to as high a standard.

Abstract

Dwarf galaxies are a significant contributor to the current star formation rate for the Universe as a whole, yet little is understood of what drives star formation in these low gas density environments. IC10 is a nearby dwarf irregular galaxy that is currently in a starburst phase making it an ideal place to study star formation and its effects on the interstellar medium in a low density setting. We present new high resolution (~1 pc) radio continuum maps of IC10 at λ=20cm (ν = 1.5GHz) taken with the e-MERLIN array. Maps were produced by reducing and combining data taken in two observational epochs, one in February and the other in November 2013. Inspection of the final maps reveal 8 compact sources coincident with extended emission, 4 of which are classified as HII regions and 4 as supernova remnants (SNR). We summarise some characteristic parameters for these candidates. Due to the lack of short baselines we detect much less flux than single dish observations, however the star formation derived from counting the individual SNR reveals a star formation rate consistent with the literature. Nearly all spatially resolved sources are coincident with regions of H-alpha emission, suggesting that they are the sites of current star formation. Interestingly, no compact sources were detected within the star forming non-thermal superbubble, either supporting that it is indeed a hypernova remnant or suggesting that SNRs within this region are too dim to be detected. Further information such as the spectral index of each observed source as well as higher resolution images will be required for further analysis.

Contents

1: Introduction

1.1: Dwarf Galaxies

Galaxies are large collections of stars bound together by gravity. They form within dark matter halos that were seeded through instabilities in the very early universe. These regions can be traced through temperature fluctuations in the Cosmic Microwave Background (CMB). After decoupling from the photon-baryon fluid, baryonic matter was able to collapse gravitationally into these dark matter halos to form proto-galaxies. Larger galaxies are formed through bottom-up processes as smaller progenitors merge together to form larger galaxies (**Searle & Zinn 1978**). However there are some problems with this model of the universe. Currently the Lambda Cold Dark Matter (ΛCDM) model offers the best description of the universe, but this model underestimates the number of spiral galaxies that are observed (**Steinmetz & Navarro 2002**). This model predicts large numbers of mergers which would disrupt or destroy many disk structures and leave elliptical and irregular remnants.

There are several different types of galaxies, ranging in size from super massive galaxies containing trillions of stars to dwarf galaxies containing a few tens of millions of stars. Galaxies are usually classified according to their visual morphology. Spiral galaxies are characterised by flat, rotating, dusty disks with a bulge in the centre. These types of galaxies normally have spiral arm features, incited by density waves leading to bouts of massive star formation throughout the galactic disk (**Lin & Shu 1964**). The spiral arms are naturally a blue colour as they consist of young Population I stars whereas the central bulge normally contains older Population II stars, yielding a redder colour. Elliptical galaxies have a roughly ellipsoidal shape and a smooth nearly featureless brightness profile. These types of galaxies are usually found in areas of higher galaxy density such as the centres of galaxy clusters and consist of old, low-mass Population II stars. There is very little star formation within elliptical galaxies. These two observations hint that elliptical galaxies are a product of galactic merger events (**Cole et al. 1994**) and support hierarchical formation theories of galaxy formation. Galaxies with a shape that does not fall into any of the regular classes within the Hubble sequence are known as Peculiar galaxies. These galaxies have disturbed appearances and are thought to be created when spiral or elliptical galaxies gravitationally interact.

Dwarf galaxies are on the lower end of the mass spectrum of galaxies. Due to the hierarchical nature of the formation of structure in the ΛCDM model, the majority of galaxies in the universe are dwarf galaxies (**Marzke & da Costa 1997**) and are close analogues to the building blocks of galaxy formation at high redshifts (**Lagos et al. 2009**). These objects have a similar classification scheme to normal galaxies,

with objects such as dwarf ellipticals (dE), dwarf spheroidals (dSph) on one hand and dwarf irregulars (dI) on the other.

Dwarf galaxies cause interesting problems for simulations of galaxy formation. In the hierarchical approach, low mass galaxies including dwarf galaxies form early. Simulations fail to account for the observed specific star formation rates, producing too little star formation at later times (**Silk & Mamon 2012**). It is important to understand why current models differ from observed parameters and dwarf galaxies are an optimal place to start.

Star formation is the process of by which large dense clouds of gas collapse to form stars. Empirical data suggests that the primary requirement for star formation is an abundance of cold gas (**Elmegreen 2012**). This cold gas is normally found in regions that are shielded from strong sources of (ionising) radiation. A cloud of gas can collapse under its own gravity if the cloud reaches its Jeans mass, the mass at which the gravitational force overcomes the gas pressure of the cloud characterised by its velocity dispersion (**Jeans 1902**). The Jeans mass depends on both the temperature and the density of the gas with colder, denser gas more prone to collapse.

Processes which either reduce the temperature or increase the density of a gas cloud such that the Jeans mass is reached are known as star formation triggers. In massive galaxies, star formation is normally incited in shock fronts where interstellar gas clouds are compressed, increasing their density. These processes include galaxy interactions, global spiral density waves (**Roberts 1969**), the presence of a bar potential in a galaxy and the shocks fronts generated in supernova explosions (**Deharveng et al. 2010**), among others.

In dwarf galaxies however, there are no obvious triggers for star formation. Major star formation triggers such as density waves are absent and the gas densities are low. **Kennicutt (1989)** showed that star formation has a threshold at low gas surface densities (3-4 $M_\odot$ / pc^2), with factors such as the galactocentric radius of the star formation region and the dynamical properties of the region determining the trigger threshold for star formation. This result was based on the Toomre criterion (**Toomre 1964**) **Hunter et al. (1998)** discovered that star formation does occur in dwarf galaxies, even where the gas density is lower than the threshold determined through observations of disk galaxies.

Dwarf galaxies are therefore important for understanding how star formation occurs in systems that are globally below the trigger threshold for star formation. Also, they can shed light on a wide range of astrophysics including star formation in low metallicity environments, galaxy morphological transformations, the coupling between dark and baryonic matter , and the mechanisms by which galaxies gas

reserves are depleted. Lastly, they are relevant to study the interactions between host and satellite systems (**Weisz et al. 2014**).

1.2: IC10

IC10 (see **Figure 1.1**) was initially discovered by **Swift (1887)** and was determined to be extra-galactic by **Mayall (1935)**. **Hubble (1936)** suspected that IC10 was a part of the local group, but this was not confirmed for many years. Radial velocity measurements by **Roberts (1962)** and an investigation by **Yahil et al. (1977)** revealed that IC10 is travelling towards the Milky Way, offering strong evidence for membership of the Local Group, but it was not confirmed until direct distance measurements using Cepheid variables were undertaken by **Saha et al. (1996)**. However, there is still much debate on the true distance measurement to IC10, due to it being located close to the Galactic

Figure 1.1: Inverted Hα image of IC10 taken from Hunter & Elmegreen (2004).

midplane (b = −3.∘3) with obscuring spiral arms of the Milky Way making distance measurements challenging (**Massey et al. 1992** and **Sanna et al 2008**). Within the thesis we have adopted a distance to IC10 of 0.7Mpc, as listed by **Hunter et al (2012)**. IC10 was classified as an IBm galaxy by **de Vaucouleurs & Freeman (1972)**.

IC10 is well studied in the literature (see **Table 1.1**), with many investigations taking covering many different wavelengths. Here is a summary of the studies that have been carried out on IC10.

IC10 is well studied at X-ray wavelengths due to the presence of a black hole-Wolf-Rayet binary system, IC10 X-1. The black hole is the largest stellar mass black hole discovered, with an estimated mass of 23-24$M_\odot$ (**Silverman & Filippenko 2008**). IC10 X-1 was discovered by **Brant et al. (1997)** whilst observing the Wolf-Rayet stars within IC10. Since then there have been many studies at X-ray wavelengths by **Wang et al. (2005)**, **Prestwich et al. (2007)**, **Pasham et al. (2013)** and many others.

The low galactic latitude of IC10 makes it difficult to study it at UV and optical wavelengths with reliable optical data only being available in Hα. There have nonetheless been several studies of IC10 at optical wavelengths such as **de Vaucouleurs & Ables (1965)**, **Karachentsev & Tikhonov (1993)**, **Massey & Armandroff (1995)** and **Tikhonov & Galazutdinova (2009)**. These studies are primarily focused on measuring the photometric distance to IC10 and to study the

Wolf-Rayet stars, but also reveal information about star clusters within IC10. Isochrone analysis on H-R diagrams reveal that IC10 has an enhanced metallicity over other dwarf galaxies of the same mass. Hα studies of IC10 have been focused on studying the HII regions associated with regions of star formation (**Hodge & Lee 1990**). All of these features yield strong evidence that IC10 is in a starburst phase.

Property	Value	Reference
RA (J2000)	00 20 17.3	Jarrett et al. (2003)
DEC (J2000)	+59 18 13.6	
Galactic Longitude (l)	118.96	
Galactic Latitude (b)	-3.33	
Galaxy Type	IBm	de Vaucouleurs & Freeman (1972)
Angular Size (Major Axis)	11.68'	Jarrett et al. (2003)
Angular Size (Minor Axis)	7.12'	
Position Angle	132	
Radial Velocity	-348 kms^{-1}	Huchra et al. (1999)
Distance	0.7 Mpc	Hunter et al. (2012)
Metallicity (log 0/H + 12)	8.2	Lozinskaya et al. (2009)
Integrated Star Formation Rate	0.35$M_\odot$yr^{-1}	Bell (2003)
Absolute Visual Magnitude	-19.08	Gil de Paz & Madore (2005)
Baryonic Mass	5×10^8 $M_\odot$	Vaduvescu et al. (2007)
Dynamical Mass	1.7×10^9 $M_\odot$	Mateo (1998)

Table 1.1: *Properties of IC10.*

There have been several studies of IC10 at infrared wavelengths. Initial infrared photometry was taken by **Wilson et al. (1996)** , observing Cepheid variables to measure its distance. Photometric studies taken by **Borissova et al. (2000)** and followed up by **Kim et al. (2009)** reveal more information about the reddening and distance to IC10 as well as the age and other relevant information about the star forming regions of IC10.

IC10 was first observed in HI by **Roberts (1962)**. These observations revealed a large cloud of neutral hydrogen surrounding the optically visible part of IC10. However due to the large beamwidth and frequency resolution of the observation, no structure of the cloud was resolved. This was followed up by several single dish observations by **Epstein (1964)**, **Gouguenheim (1969)**, **Bottinelli et al. (1972)** and **Dean & Davies (1974)**. Although these single dish measurements did not possess a high enough resolution to reveal any structure of the cloud, they did reveal that the HI envelope is rotating. Later single dish observations by **Huchtmeier (1978)** and **Nidever et al. (2013)** revealed that the HI envelope is more than 20 times the size of the optical counterpart and is at an inclination of $i \sim 45^o$. The observations also revealed that the gas is rotating at the same inclination as the central region but in the opposite direction, implying that IC10 could be the result of an interaction with another galaxy or intergalactic cloud, or that the galaxy is still in formation,

accreting surrounding gas (the former being more generally accepted). The first interferometer measurements of IC10 were undertaken by **Rogstad et al. (1967)** using a 2 element interferometer. These observations dramatically improved the spatial resolution of the observations. There have been many other interferometry observations of the HI envelope by **Shostak (1974)**, **Shostak & Skillman (1988)** , **Wilcots & Miller (1998)** and **Hunter et al. (2012)**. These observations reveal structure in the HI in the central region, including the presence of HI holes. These holes are characteristic of dwarf galaxies and are associated with energetic star formation rates (**Brinks and Bajaja 1986**).

IC10 was first studied at radio continuum wavelengths by **Klein et al. (1982)** and followed up by **Klein & Gräve (1986)**. These studies revealed that most of the bright radio emission is found adjacent to HII regions and indicated the presence of non-thermal radiation. **Yang & Skillman (1993)** revealed the presence of a large non-thermal 'bubble' which they interpreted as a result of many supernova remnants. Another interpretation includes a hypernova remnant **(Lozinskaya & Moiseev 2007)**. More recently, studies by **Heesen et al. (2011)** had much finer resolution than previous studies and revealed information about the magnetic fields and star formation rates within IC10.

We will be studying IC10 using the e-MERLIN array at 20cm (1.5 GHz). Due to the galaxy being in starburst phase, we should be able to see synchrotron radiation radiated by supernova remnants (SNR) and Bremsstrahlung emitted by HII regions. This study is at much higher resolution than any previous study allowing us to image individual supernovae.

2: Radiation Mechanisms

2.1: Introduction

In order to understand the properties of radio sources, it is necessary to develop an understanding of the radiation mechanisms behind them. This section of the thesis will focus on explaining the major radio emission mechanisms and sources which radiate by them. This section will start by discussing what will be referred to as the spectral index and will then go on to explaining the emission pattern from a moving charge (Larmor radiation). The rest of the section will be applications of this concept including blackbody radiation and, Thermal and Non-Thermal radiation mechanisms.

2.2: Spectral Index

The spectral index, α, of a source is a measure of how the flux density, S, of a source depends on frequency, v. The spectral index is given by:

$$S \propto v^{\alpha}$$

Spectral indices are an important diagnostic used to identify the mechanisms behind observed radiation. For example, a perfect black body will have a spectral index of α=2 on the Rayleigh-Jean tail. However the main source of black body radiation at radio wavelengths is dust, which is not a perfect blackbody. In this case the spectrum is approximated with an additional factor, β, such that α=2 + β. For free-free emission or Bremsstrahlung, the slope is of order α = -0.1 at radio wavelengths. Finally, non-thermal emission or synchrotron radiation has a spectral index of at least α=-0.6 but is often much steeper, usually between -0.7 and -1.0 depending on the properties of the electrons (injection spectrum, age, magnetic field strength etc).

2.3: Larmor Radiation

Electromagnetic radiation is produced by accelerating charges, all of the radiation produced in the radio spectrum at cm and m wavelengths is produced ultimately by this mechanism. It is therefore important to understand this mechanism and how it applies to different situations. The following is taken from **Longair (pg 155-158)**.

Consider a point charge, q, initially moving at a speed, $v_0 \ll c$, which then decelerates uniformly over a time t_0. At a time $T \gg t_0$ after this has happened, the pulse of radiation reaches a radius of $R = cT$ (see **Figure 2.1**).

At angle θ, the geometry of the 'kink' in the field requires that the ratio of the transverse field to the radial field be:

$$\frac{E_t}{E_r} = \frac{v_0 T \sin \theta}{c t_0}$$

The radial component of the field is simply the Coulomb field associated with the charged particle which is given by:

$$E_r = \frac{q}{4\pi\epsilon_0 R^2}$$
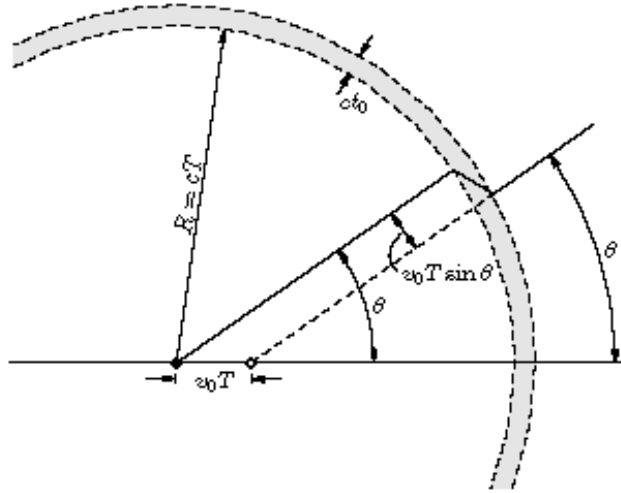
Figure 2.1: *Schematic showing the geometry of Larmor radiation. This diagram shows how the kink in the electric field which generates a transverse component of this field. Diagram taken from **Schroeder (1999)**.*

Therefore substituting in E_r and $T = \frac{R}{c}$, the transverse electric field is given by:

$$E_t = \frac{q \sin \theta}{4\pi\epsilon_0 R c^2} \dot{v}$$

Where $\dot{v}$ is the acceleration of the particle given by $\dot{v} = \frac{v_0}{t_0}$.

This equation shows an interesting result, that the transverse electric field is proportional to R^{-1} whereas the radial electric field is proportional to R^{-2}. This means that at large R, the transverse electric field will contribute to the radiation field and the radial field will not. Also due to the sinusoidal component to this equation, the transverse wave will be invisible in the direction that the particle is accelerating in.

To find the total power emitted by an accelerating charge, we can use the Poynting flux, **S** (units are Js⁻¹m⁻²), which is defined by:

$$S = \frac{1}{\mu_0} E \times B = \varepsilon_0 c^2 E \times B$$

16

Where μ_0 is the permeability of a vacuum, ε_0 is the permittivity of a vacuum and the bold text indicates a vector quantity.

Assuming the magnetic field has the same amount of energy stored as the electric field, using $E = cB$ (**Hecht pg 47**), the Poynting flux can be changed to:

$$|\boldsymbol{S}| = \varepsilon_0 c E^2 = \frac{q^2 \sin^2\theta}{16\pi\varepsilon_0 c^3 R^2}\dot{v}^2$$

In order to find the total power emitted by the charged particle, P, we integrate over all directions to yield:

$$P = \frac{q^2\dot{v}^2}{6\pi\varepsilon_0 c^3}$$

This last equation is called Larmor's equation. This equation states that any charged particle emits radiation when accelerated and the power is proportional to the square of the acceleration.

This formulation of the equation is non-relativistic and only works when $v \ll c$. At relativistic speeds $v \approx c$, this equation represents the radiation emitted in the instantaneous rest frame of the particle and must be transformed to the observer frame to obtain the observed power.

The radiation from Larmor's equation has a dipolar form. The electric field strength varies with sin θ and the power radiated varies with sin²θ. As a result there is no radiation emitted in the direction of acceleration.

This equation also does not take into account quantum mechanical effects, for example Larmor's equation predicts electrons will quickly radiate their kinetic energy and spiral into the atomic nucleus.

2.4: Blackbody Radiation

All objects at any temperature emit electromagnetic waves in the form of thermal radiation (see **Jewett & Serway pg 1154**). This is due classically to the accelerations that charged particles undergo whilst thermally agitated. A blackbody is an ideal material, in thermodynamic equilibrium, which absorbs all radiation incident on it. A blackbody in thermodynamic equilibrium is also an ideal emitter at all frequencies and radiates isotropically. The radiation such a material emits is called blackbody radiation. Blackbody radiation has a characteristic spectrum which depends only on the temperature of the material. The spectrum of such an object can be represented by the Planck Function:

$$I(\nu, T) = \frac{2h\nu^3}{c^2}\frac{1}{e^{\frac{h\nu}{kT}} - 1}$$

Where h is Planck's constant, v is frequency, c is the speed of light, k is the Boltzmann constant and T is the temperature of the blackbody. An example blackbody curve is given in **Figure 2.2**.

It is often convenient to approximate the Planck function by some simpler form (see **Wilson et al. pg 12-13**). At lower frequencies, $hv \ll kT$, the exponential term can be approximated by a Taylor expansion to the first order (other terms becoming too small to consider).

$$e^x = 1 + x + \frac{x^2}{2!} + \frac{x^3}{3!} + \cdots$$

The Planck function simplifies to:

$$I(v, T) \approx \frac{2kTv^2}{c^2}$$

This is called the Rayleigh-Jeans approximation. It was derived independently by Lord Rayleigh and Sir James Jeans before Planck proposed his function. This formula is good at describing the low frequency tail of the blackbody spectrum, but tends towards infinity at high frequencies.
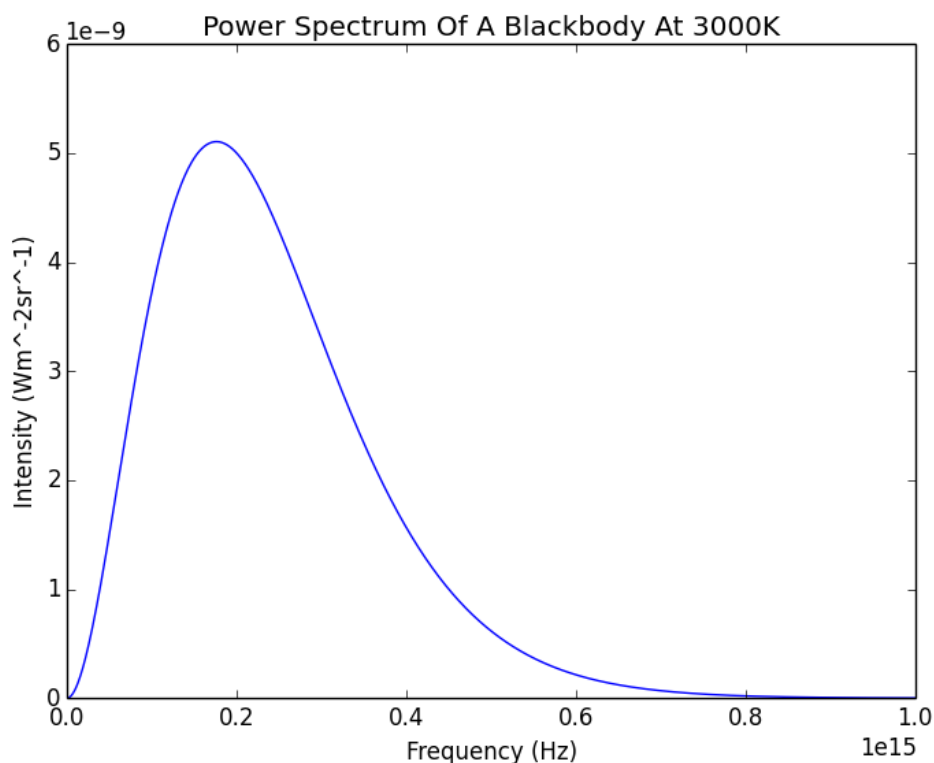
Figure 2.2: *Diagram of the Planck function for a blackbody at 3000K. There is a characteristic power law rise followed by an exponential tail.*

18

Within the Rayleigh-Jeans approximation, the brightness of a blackbody and its thermodynamic temperature are proportional. Within the radio astronomy community it has become customary to measure the brightness of a source by measuring a brightness temperature which is given by:

$$T_b = \frac{c^2}{2k\nu^2} I_\nu$$

This temperature is the temperature required to give a source the equivalent brightness it would have if it were a blackbody at temperature T.

A perfect blackbody, according to the Rayleigh-Jeans approximation, has a spectral index α=2. There are very few perfect blackbodies in the universe, but there are many close approximations. These can be approximated by a grey body which has a spectral index of α=2+β where β is a correcting factor.

For example, grey-body radiation at radio wavelengths can be radiated by large dust clouds.

2.5: Thermal Emission

Thermal emission (Bremsstrahlung) is produced by the deceleration of a charged particle whilst interacting with another charged particle. According to the Larmor equation, any charged particle which undergoes an acceleration emits electromagnetic radiation. This argument can be applied to many particles at once in an ionized plasma to yield a broad spectrum.

Bremsstrahlung emitted in an ionized plasma is usually referred to as free-free radiation. This is due to electrons interacting with the positive ions in the plasma but not getting captured by the ions in the process.

The electrons in the plasma are much less massive than the ions. If the plasma is in local thermodynamic equilibrium (LTE), the electrons and ions will have the same average kinetic energy. This means that the electrons will be travelling much faster and will contribute much more to the radiation field. Some particle interactions do not radiate significantly as the accelerations each particle experiences will be equal in opposite directions. The net electric field disturbance due to this type of interaction will approach zero at large distances.

If we assume that the electrons are the only contributor to the free-free radiation field, we can calculate what the spectrum should look like. If we assume that the speeds of the electrons in the gas can be represented by a non-relativistic Maxwellian distribution $f(v)$:

$$f(v) = \frac{4v^2}{\sqrt{\pi}} \left(\frac{m}{2kT}\right)^{\frac{3}{2}} \exp\left(-\frac{mv^2}{2kT}\right)$$

where v is the speed of the electron, T is the temperature of the plasma, m is the mass of the particle and k is the Boltzmann constant.

Bremsstrahlung is called thermal emission because of this dependence on the temperature of the plasma.

By considering the opacity of the gas as a function of frequency, τ_v, we can derive a resulting power spectrum.

$$\tau_v = \int -\kappa_v ds \propto \int \frac{N_e N_i}{v^{2.1} T^{\frac{3}{2}}} ds$$

κ_v is the absorption coefficient, N_e is the number density of electrons, N_i is the number density of ions, v is the frequency of the radiation and T is the temperature of the plasma. For a derivation, see **Appendix A**.
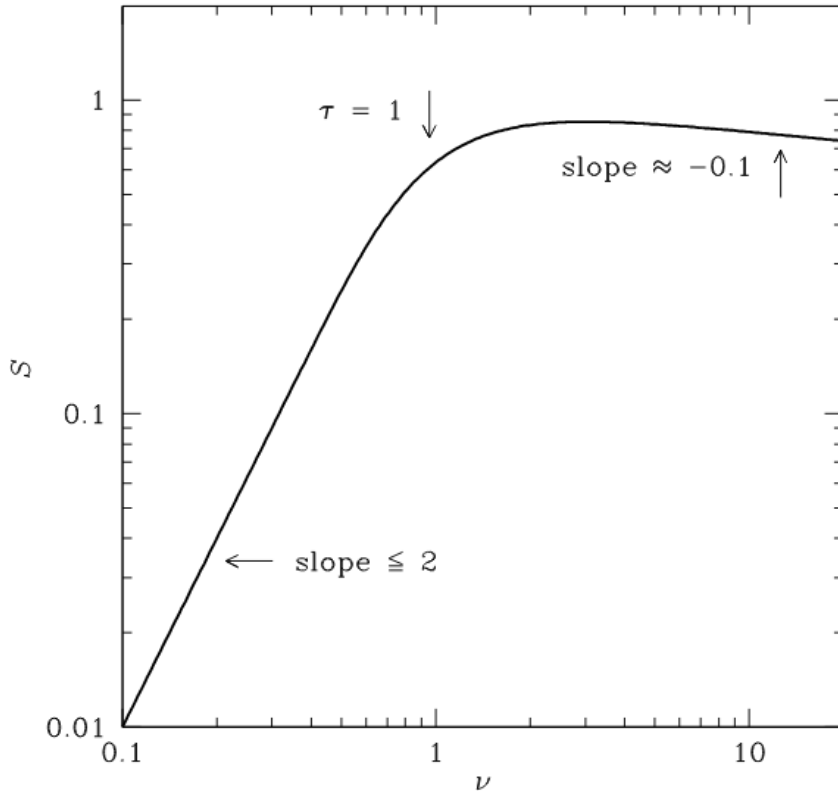
Figure 2.3: *This diagram shows the radio spectrum for a HII region with frequency (v) on the x axis in GHz and spectral flux on the y axis in Jy . At low frequencies, it behaves like a blackbody with a spectral index $\alpha \approx 2$. At the frequency where the optical depth approaches 1, the function turns over to a spectral index of $\alpha - 0.1$. Diagram was taken from* **Condon & Ransom (2007)** *.*

At low frequencies, the opacity gets large ($\tau_\nu \gg 1$) and the plasma behaves like a blackbody, with a spectral index of α≈2. This is basically the Rayleigh-Jeans tail of the blackbody spectrum. At higher frequencies, the opacity of the plasma drops ($\tau_\nu \ll 1$) and the plasma becomes transparent. The spectral index for this case is α≈-0.1. This is an important result for classifying radio sources.

Figure 2.3 is a plot showing the power spectrum of Bremsstrahlung. It is apparent that the spectrum is dominated by a blackbody curve at low frequencies and has a flat spectrum at higher frequencies.

Bremsstrahlung is found in highly ionized areas. One such source is the intracluster medium found at the centre of galaxy clusters. Here the plasma is extremely hot and emits strongly in X-rays.

On smaller scales, Bremsstrahlung is found in HII regions. HII regions are highly ionized regions of space around massive stars. These stars give out copious amounts of radiation at UV wavelengths and ionize the surrounding hydrogen. Because these stars are short lived, observations of HII regions allow us to trace where star formation is occurring. Observing this radiation as well as having an assumption about the mass distribution of new stars, we can estimate the star formation rate of an HII region. As we are observing at the radio end of the spectrum, the measurements do not suffer from extinction so observing at radio frequencies is a good way to measure the star formation rate of other galaxies (**Condon 1992**).

Bremsstrahlung can also be found in planetary nebulae. Here the star at the centre is an extremely hot white dwarf star which ionizes their ejected envelopes of hydrogen. They offer information about the low mass star formation in a region but are not particularly bright at radio wavelengths.

2.6: Non-Thermal Emission

Radiation can be produced from the centripetal acceleration of a charged particle whilst interacting with a magnetic field. According to the Lorentz force law, the particle will accelerate in a direction perpendicular to the direction of the velocity vector of the particle and the direction of the magnetic field, resulting in a circular motion. If the particle has a component of motion in the same direction as the magnetic field, it will follow a helical path (see **Figure 2.4**). This centripetal acceleration generates radiation according to Larmor's equation. Non-Thermal radiation is known as cyclotron radiation when the charged particle has low velocities (i.e., $v \ll c$) and it is known as synchrotron radiation when the charged particle is at ultra-relativistic velocities ($v \approx c$).

As electrons are low mass particles, it takes a small amount of energy for them to become ultra-relativistic. Thus the main source of synchrotron radiation is from these ultra-relativistic electrons.

The following arguments were taken from **Longair (pg 193-219)**, **Pacholczyk (pg 77-98)** and the NRAO Essential Astronomy Course (**Condon & Ransom 2007**). The easiest way to tackle the spectra of synchrotron radiation is to first consider a single electron travelling at relativistic speeds. The power radiated from such an electron is given by:

$$P = 2\sigma_{\mathrm{T}} c \beta^2 U_{mag} \gamma^2 \sin^2 \alpha$$

Where σ_{T} is the Thompson cross section, c is the speed of light, β is the ratio of the velocity of the particle to the speed of light, U_{mag} is the magnetic energy density, γ is the Lorentz factor and α is the angle between the velocity vector of the electron and the direction of the magnetic field (see **Appendix B** for more details).
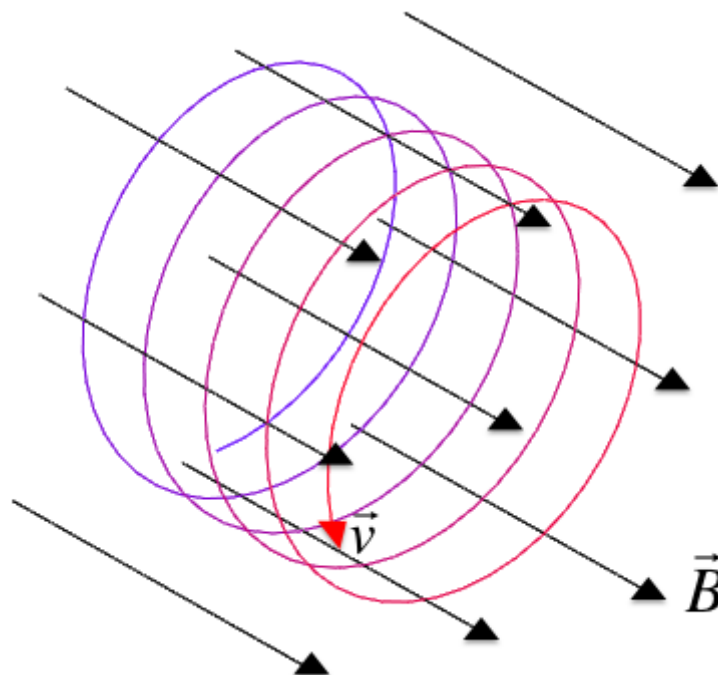
*Figure 2.4: Schematic of the path that a charged particle takes whilst interacting with a magnetic field. The Lorentz force law dictates that any component of the velocity perpendicular to the magnetic field will give rise to circular motion. Any velocity component parallel to the magnetic field is unaltered and leads to the particle pursuing a helical path following the magnetic field. Image taken from **Dawber (2013)**.*

When the electron is travelling at relativistic speeds, relativistic effects must be taken into account. For a non-relativistic electron, the Larmor equation predicts that the electron will radiate its energy in a dipole pattern perpendicular to the direction of acceleration. When an electron is travelling speeds close to c, the Lorentz transformations (**Appendix C**) predict that the power pattern will be enhanced in the direction of motion (see **Figure 2.5**).

Not only is the power enhanced in the direction of motion, but the power pattern is confined to a much narrower beam. The Lorentz transformations lead to the following expression for the angular transformation:

$$\sin\theta = \frac{\sin\theta'}{\gamma(1 + \beta\cos\theta')}$$

The primed notation refers to the angle measured in the electron's frame of reference. For synchrotron dipole radiation, the directions of zero emission are located at $\theta' = \pm\frac{\pi}{2}$. After the transformation however, this changes to $\theta \approx \pm\frac{1}{\gamma}$. The faster the electron travels, the narrower the power distribution becomes.
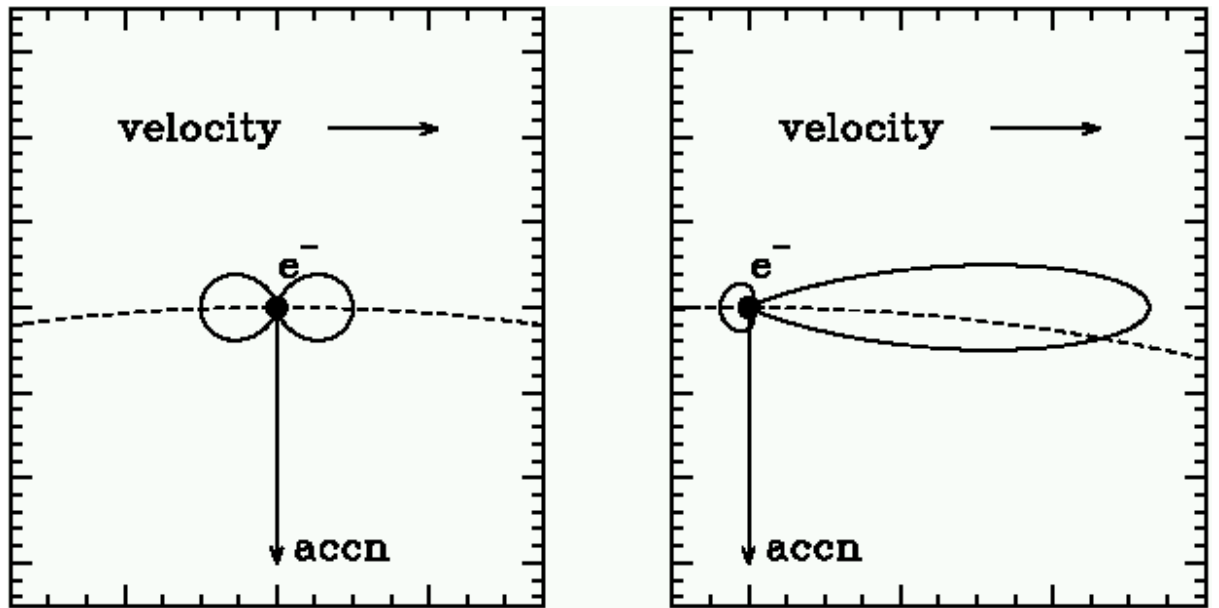
Figure 2.5: *Two diagrams demonstrating the effect of relativistic beaming. The diagram on the left shows the dipole radiation pattern for a non-relativistic electron and the diagram on the right shows the power pattern for an electron travelling at a relativistic speed. Not only is the power pattern enhanced in the direction of motion, the power is radiated in a much narrower beam. This diagram was taken from* **Flynn (2005)**.

As the electron spirals along the magnetic field, a spike of emission will be detected every time the electron is travelling directly towards the observer. The power spectrum is simply the Fourier transform of this pulse train. The majority of power will be emitted at the gyro-frequency of the electron's motion. The power spectrum for a single electron comes out as:

$$P(v) = \frac{\sqrt{3}e^3 B\sin\alpha}{m_e c^2}\left(\frac{v}{v_c}\right)\int_{v/v_c}^{\infty} K_{5/3}(\eta)d\eta$$

Where B is the magnetic field strength, m_e is the rest mass of an electron, v_c is the critical frequency and $K_{5/3}$ is a modified Bessel function. More information, including a plot of a single electron energy spectrum can be found in Appendix B.

To find the spectrum due to an ensemble of electrons, an energy distribution of the electrons is required. The electron energy spectrum is non-thermal and therefore the electrons do not follow a simple Maxwellian speed distribution. The energy spectrum can be approximated by a power law:

$$N(E)dE = kE^{-\delta}\,dE$$

Where E is the energy of the electrons and k and δ are constants.

Eventually, the emission coefficient of synchrotron radiation can be determined. It is found to be proportional to both frequency and magnetic field strength. To see how this result is derived, see **Appendix B**.

$$\varepsilon_\nu \propto B^{\frac{\delta+1}{2}} \nu^{\frac{1-\delta}{2}}$$

Once the initial injection spectrum is known, the spectrum of synchrotron radiation can be found. The spectral index of a synchrotron source comes out as $\alpha = (1 - \delta)/2$. That is the spectral index of synchrotron radiation depends on the initial injection energy spectrum of the electrons. The spectrum of a synchrotron source is shown in **Figure 2.6**.
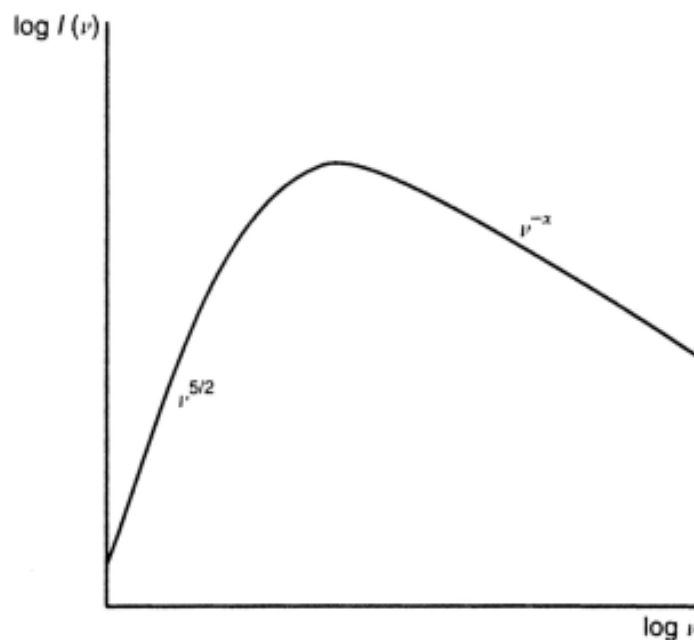
*Figure 2.6: Diagram showing the spectrum of a synchrotron radiation source. At low frequencies, self-absorption becomes an important effect, suppressing the power emitted. At higher frequencies, the spectrum follows a negative gradient as described earlier. Diagram taken from **Longair pg 219**.*

At lower frequencies, the spectrum of a synchrotron source has a steep slope with a spectral index of $\alpha = \frac{5}{2}$. This is due to synchrotron self-absorption (see **Chevalier 1998**) and is independent of the spectrum of the emitting electrons as long as the

24

magnetic field they are travelling through is uniform. After a critical frequency, the spectrum turns over to a negative gradient which is entirely dependent on the initial energy spectrum of the electrons. Typically, the spectral index of a synchrotron source is α=-0.6.

Synchrotron radiation is normally found in supernova remnants (SNR). Here electrons are shock accelerated to ultra-relativistic speeds by the shock wave from the supernova and then spiral around the magnetic fields from the surrounding interstellar medium, emitting synchrotron radiation. If equipartion of energy is assumed (the cosmic ray energy density is equal to the magnetic energy density), the strength of the magnetic fields in synchrotron sources can be estimated.

Now that each of the radiation mechanisms has been discussed, we can now use them to investigate the nature of various radio sources. **Figure 2.7** shows how each of the components come together in the radio power spectrum of M82.
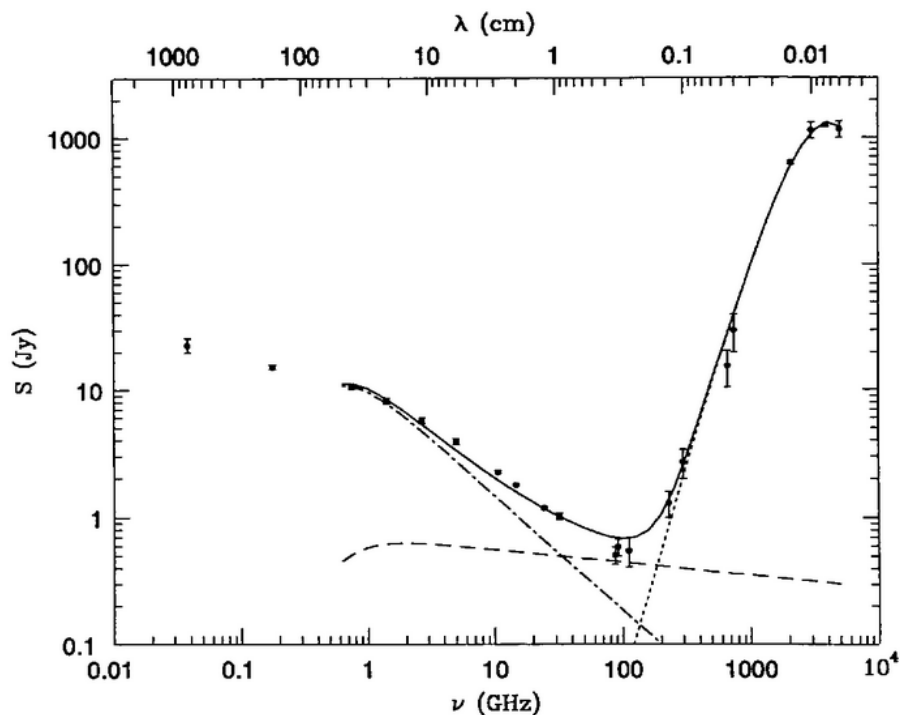
*Figure 2.7: Observed radio/FIR spectrum of M82 taken from **Condon (1992)**. Synchrotron radiation is signified by the dot-dash line, Bremsstrahlung is represented by the dashed line and the radiation due to dust is represented by the dotted line. The solid line represents the sum of these components.*

2.7: Radio Evolution of Supernovae and Supernova Remnants

A supernova (SN) is an extremely luminous, stellar explosion that massive stars undergo at the end of their nuclear burning lifetimes. After the nuclear fuel sources within the star are exhausted, the core can no longer support itself against gravitational collapse. For intermediate mass stars, the collapse is halted by neutron degeneracy pressure, leaving a neutron star in the process. For high mass

stars, the core cannot support itself with neutron degeneracy and collapses into a singularity (black hole). As a star collapses, outer envelopes fall onto the dense core and rebound at supersonic speeds (creating bow shocks in the interstellar medium). At the base of the shock, the densities are so high that neutrinos are generated and transfer away the majority of the gravitational energy of the collapse, creating a neutrino wind. The supernova becomes visible once the shock wave has breached the outer envelope of the collapsing star. The temperature is extremely high and initially radiates in the UV, but as the supernova expands and cools, the SN becomes optically visible and eventually, visible at radio wavelengths (**Philips pg 171-204**).

SNe are split into two main categories: Type I, which are SN without hydrogen absorption lines and Type II SN, which are SN with hydrogen absorption lines. The Type I SN can be further split into Type Ia Type Ib, and Type Ic supernova. Type Ia SN are a result of a white dwarf accreting matter from a binary star until its core mass overcomes the Chandrasekhar limit and undergoes collapse (**Branch & Nomoto 1986**). These supernovae always happen at the same mass and have the same magnitude, making them excellent standard candles. Type Ib SN are thought to be core collapse in a hydrogen stripped star, for example, an exploding Wolf-Rayet star (**Schaeffer et al. 1987**). Type Ic SN are similar to Type Ib SN except they lack Helium lines as well as Hydrogen. A classification scheme for Type Ib SN is given in **Porter & Filippenko (1987)**.

Type II SN can also be split into two categories, Type II-L (linear) SN and Type II-P (plateau). These classifications are based entirely on the light curve of the SN. A SN is classified as a Type II-P if the light curve temporally flattens roughly 30-80 days after maximum light (optical), otherwise it is known as a Type II-L. A classification scheme for Type II SN is given in **Barbon et al. (1979)**.

Type Ib, II-L and II-P SN are found associated with star forming regions in galaxies, near HII regions and dust. This indicates that these types of SN are due to young massive stars which evolve quickly (**Maza & van den Bergh 1976**). Type Ia SN do not have this dependence and can be found anywhere in the galaxy and are usually associated with old low mass stars. A summary of each of the different types of SN can be found in **Table 2.1**.

When a SN explodes, a high energy density shell is generated and interacts with circumstellar material. This circumstellar material arises from a pre-supernova stellar wind which may not be uniform (**Weiler et al. 1990; Spyromilio 1994**). The expanding density shell is Rayleigh-Taylor unstable which drives turbulent motion, which amplifies magnetic fields and accelerates electrons to ultra-relativistic speeds (**Chevalier 1982**). The electrons in the expanding plasma are accelerated giving rise to cosmic ray electrons (CRe). The acceleration is through a first-order Fermi

mechanism(see **Bell 2004**), which involves a travelling magnetic field reflecting the electrons to higher and higher speeds, giving the electrons a non-thermal energy spectrum. The combination of ultra-relativistic electrons with magnetic fields results in the production of synchrotron radiation, which is the major emission mechanism of SNe at radio wavelengths.

Characteristic	Type Ia	Type Ib	Type II-L	Type II-P
Definition	No hydrogen	No hydrogen	Hydrogen	Hydrogen
Location	All galactic types, interarm and halo	Late-type galaxies, near H II regions	Late-type galaxies, near H II regions	Late-type galaxies, near H II regions
Optical spectrum	P Cygni lines, deep $\lambda6150$ Å absorption (Si II $\lambda6355$ Å)	P Cygni lines, no $\lambda6150$ Å absorption (Si II $\lambda6355$ Å), "prematurely old," distinct He lines	P Cygni lines, complex spectrum	P Cygni lines, complex spectrum
Ejection velocity	$\geq 10^4$ km s^{-1}	$\geq 10^4$ km s^{-1}	$\leq 10^4$ km s^{-1}	$\leq 10^4$ km s^{-1}
Absolute magnitude ($H_0 = 50$ km^{-1} s^{-1} Mpc^{-1})	-20^m homogeneous	-18^m0---18^m5 homogeneous?	$\leq -18^m$ heterogeneous	$\leq -18^m$ heterogeneous
Light curve form in B light[1]	Sharp rise, decay $\sim 0^m1$ d^{-1} to ~ 30 days, then $\sim 0^m02$ d^{-1} exponential decay	Same general form as Type Ia, but possibly slower > 30 day decay	Sharp rise, decay $\sim 0^m05$ d^{-1} to ~ 100 days, then $\sim 0^m01$ d^{-1} exponential decay	Sharp rise, decay $\sim 0^m03$ d^{-1} to ~ 30 days, then plateau to ~ 80 days, then 0^m05 d^{-1} to ~ 125 days, then $\sim 0^m006$ d^{-1} exponential decay
Infrared	Second H-band maximum at ~ 30 days, fast decay $\sim 0^m05$ d^{-1}	Peaks near optical maximum, no second maximum, slow decay $\sim 0^m03$ d^{-1}	Thermal, heated dust at late times	Thermal, heated dust at late times
Radio	No detections	Strong, steeper spectrum $\alpha \sim -1$, rapid decay $t^{-1.6}$	Strong, flatter spectrum $\alpha \sim -0.6$, slow decay $t^{-0.7}$	No well-studied cases

*Table 2.1:This table summarizes the identifying features of SN. It was taken from **Weiler & Sramek 1988**, and does not include Type Ic SN.*

The spectrum of a SN is very much dependent on time. As the circumstellar shell is ionized and dense, it is optically thick at radio wavelengths. The SN will not become visible until the shock wave has passed far enough through the shell such that the optical depth at a given frequency approaches 1. The shock wave travelling through the shell accelerates the electrons, generating radio emission.

Then the spectrum will evolve as the optical depth changes, due to the density gradient of the shell declining whilst expanding. Emission at progressively longer

wavelengths 'turn on' , producing a radio power spectrum of the form $S \propto \nu^{\alpha} t^{\beta}$ (**Weiler & Sramek 1988**). This is due to a combination of free-free absorption and synchrotron self absorption in the ionized circumstellar medium (See **Figure 2.8**).
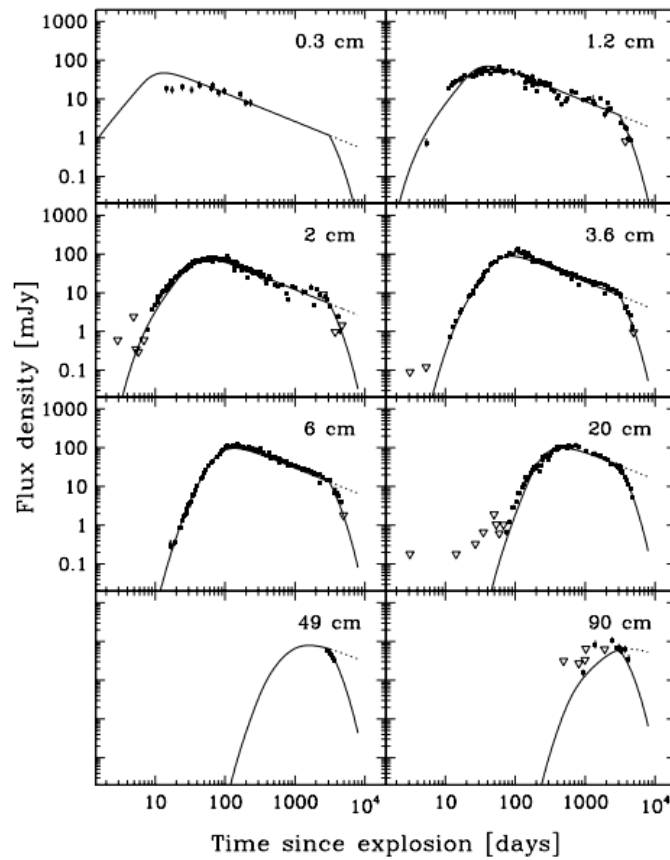
Figure 2.8: *Radio light curves of SN 1993J plotted from left to right and top to bottom at 0.3, 1.2, 2, 3.6, 6, 20, 49 and 90cm taken from **Weiler et al. (2010)** . The solid line represents the best fit from a model which combines synchrotron self-absorption and free-free absorption. It can be seen from the diagrams that the emission 'turns on' and shorter wavelengths first and 'turns on' later for longer wavelengths.*

This happens for all frequencies, SNe are usually detected optically and can then be observed at longer wavelengths later on. Radio SN (RSN) occur when the SN 'turn on' at radio wavelengths. This can occur within a time period from days to years after the optical SN. Both the intensity and the time scale for radio emission are entirely dependent on the properties of the circumstellar material, and can be used to probe mass-loss rates of SN progenitors.

The spectral index of a source also evolves with time (see **Figure 2.9**). At early times, free-free absorption is invoked to describe the spectral index and later on, synchrotron self absorption is called upon to describe the change in spectral index (**Weiler et al. 2007**). The spectral index settles on a value when the circumstellar envelope becomes progressively optically thin to longer wavelengths and the spectral index is solely due to the synchrotron emission from the SN.
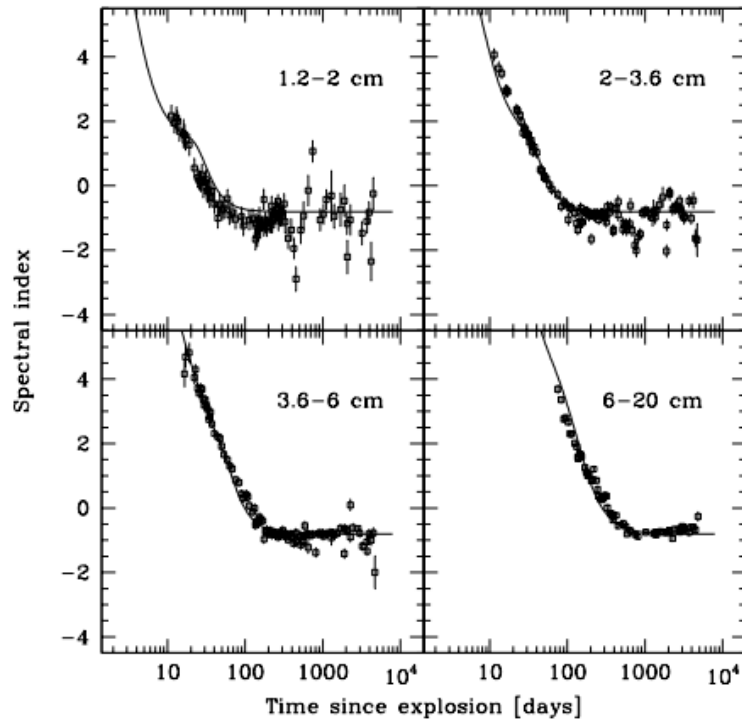
Figure 2.9: *These diagrams, taken from **Weiler et al. (2010)**, show the spectral index, α ($S \propto \nu^{\alpha}$) evolution for SN 1993J between 1.2 and 2cm (top left), between 2 and 3.6cm (top right), between 3.6 and 6cm (bottom left) and between 6 and 20cm(bottom right). The solid lines represent the best fit from a model combining synchrotron self-absorption and free-free absorption. It can be seen that the spectral index flattens out later for longer wavelengths.*

Supernova remnants (SNR) are the resulting structure from a SN after some period of time has passed (hundreds to thousands of years. During expansion, the SNR will go through 4 main phases of expansion into a uniform medium (**Green 1984**):

- Phase I expansion, known as free expansion, occurs just after the SN explodes. In this phase, the mass that is swept up in the ISM is less than the ejected mass. In this phase, the diameter of the remnant is directly proportional to the age of the remnant, i.e., $D \propto t$.

- Phase II expansion, known as Sedov expansion, occurs when the mass that is swept up in the ISM is greater than the ejected mass. The expansion is decelerated such that $D \propto t^{\frac{2}{5}}$.

- Phase III expansion, known as isothermal expansion, occurs when the radiative cooling of the expanding shell becomes important. The shell is also decelerating as it pushes further into the ISM.

- Finally, Phase IV expansion, known as the extinction phase occurs when the remnant merges into the surrounding ISM.

The radio emission coming from a SNR can be seen coming from the shock front expanding into the ISM, as this is where the electrons are accelerated.

29

SNRs can be split into 4 different classifications: Balmer-dominated, Oxygen-rich, Plerionic-composite and Evolved (**Weiler & Sramek 1988**). Balmer-dominated SNRs are defined by strong Balmer lines of hydrogen but weak emission in [OIII] and [SII] (**Mathewson et al. 1983**). This can be understood as a high-velocity, non-radiative collision-less shock encountering neutral gas in the ISM.

These SNR are thought to be the result of a Type Ia SN. Oxygen-rich SNR are found near HII regions and are thought to be from the SNe of massive stars (< 25 $M_{\odot}$) where the oxygen rich spectrum comes from processed material from within the stellar interior. Plerionic-composite SNR are SNR that show a surrounding shell and a filled interior (**Wilson & Weiler 1976**). These SNR are thought to have a central neutron star which provides energy to the centre of the SNR via rotational energy losses. Finally, Evolved SNR are classified as having a [SII] to Hα ratio greater than 0.7. This category represents the final evolution of a SNR. These SNR fade slowly until they are no longer detectable.

3: Calibration and Imaging

3.1 Introduction

All observations of astronomical sources at any wavelength require calibration. It is important to standardise the data observed so that they can be properly compared to other data in the literature. A unique advantage of measuring at radio wavelengths is that amplitude, phase and polarization of individual photons can be measured and recorded. This allows data editing and calibration to take place at a later date than when the observation took place. As the entire dataset is stored, many iterations of calibration can be carried out until optimal solutions are determined. Also due to the Fourier nature of the observations, unique problems can arise when averaging and imaging the data. In this section, the major steps of calibration and imaging of radio interferometry data are described along with problems that can limit the sensitivity of the observations.

3.2: AIPS

The NRAO Astronomical Image Processing System (*AIPS*) is a program for calibration and editing of radio interferometry data and the analysis of astronomical images constructed using Fourier synthesis techniques. *AIPS* was originally developed in the 1980's for the calibration of data from the Very Large Array (VLA) but has since been adapted for use on many other instruments including e-MERLIN.

Calibration is carried out in *AIPS* through the use of tasks that operate on the data and associated tables. Corrections are recorded in tables so that the original data remains unaltered. If a calibration solution is deemed incorrect, the corresponding table can simply be deleted. Calibration corrections can be applied to the data 'on the fly' by many tasks but once the final corrections have been found, they can be applied to the original data creating a new, calibrated dataset in the process. This improves the speed at which subsequent operations can be completed (such as imaging).

 Some of the important tables and associated tasks are detailed in **Table 3.1**.

The tables used in *AIPS* are useful for the calibration process. Many different versions of the tables can be saved at once through the use of extensions. This makes it easy to come back to previous versions of the calibration if newer versions are flawed. This is especially powerful when dealing with CL tables after a bout of self-calibration (see section **3.4.5**).

Table	Name	Description	Example Tasks
HI	History Table	Keeps a record of the tasks and arguments used in those tasks.	PRTHI
AN	Antenna Table	Contains information about the antennae used within the observation including co-ordinates and properties of the dishes.	PRTAN
SU	Source Table	Contains information about the sources used within the observation, including information about the source position and flux density.	SETJY, GETJY
FQ	Frequency Table	Contains information about the frequencies, channel spacings, bandwidth and IFs used within the observation.	LISTR
FG	Flag Table	Contains information about bad data that are to be removed from the data.	TVFLAG, SPFLAG, CLIP
SN	Solution Table	Contains corrections for the antenna delay, rate and complex gain corrections that are solved for in various tasks.	CALIB, FRING
BP	Bandpass Table	Contains corrections for the bandpass used in the observation.	BPASS
CL	Calibration Table	Contains the complex gain corrections to be applied to the dataset. Is comprised of the corrections calculated in the other tables.	CLCAL

Table 3.1: *Some of the main tables that are used in the AIPS calibration process The name of the table, a description of what it contains and some example tasks which use or alter the tables.*

3.3: Calibrator Sources

When calibrating radio interferometry data, it is necessary to use calibrator sources. In most radio observations, two calibrator sources are used, a primary calibrator and a secondary calibrator.

Primary calibrators are bright compact sources which have a stable emission spectrum over long periods of time. These sources are well studied in the literature with accurate flux measurements and models available. Interferometers cannot measure the absolute flux of a source, only an instrumental flux. The primary calibrator is required to assign the instrument flux to an absolute value (see section **3.4.3**). The primary calibrator is also used to determine the bandpass corrections for the observation (see section **3.4.4**). As the primary calibrator is used to determine the flux scale for the observation it only needs to be observed once, usually at the start or end of the observing run and does not need to be in the same area of sky as the source.

Secondary calibrators are bright compact radio sources which are located close to the source that is being observed. These sources are usually intrinsically variable but can be used if they vary on a timescale much longer than the observation length. The primary objective of using a secondary calibrator is to keep track of the variability of the atmosphere and antennas as the source moves across the sky (see section **3.4.2**). The timescales of phase variability are usually tens of minutes and so

the observation runs need to be planned accordingly. The secondary calibrator is periodically observed for a short period of time followed by a longer observation of the source.

Calibrator sources are vital for the calibration process and are selected depending on the position of the source to be observed.

3.4: Calibration

In this section, the various problems that need to be corrected by calibration are detailed along with the steps that are taken to solve them. The general calibration technique is detailed in section **3.4.6**.

3.4.1: Flagging and Clipping

Radio Frequency Interference (RFI) can be problematic for the calibration of a dataset. These are signals received by the telescope which are not to do with the source that is being observed. RFI is mainly from external sources but some RFI comes from the telescope itself, from faults in the receivers, signal path or correlator. As much of this interference as possible needs to be removed before the calibration process can start.

For e-MERLIN, the data is initially passed through a Python based pipeline which automatically flags known problems with the telescopes. The flagging that is undertaken by hand mainly removes external sources of RFI.

Due to the nature of interferometry, some of the weaker sources of RFI are automatically filtered out. The delay of a telescope in a 2 element interferometer is tuned to the source that is being observed. If a source of RFI gets picked up by both telescopes, the delay causing the signals will likely be out of phase when combined in the correlator.
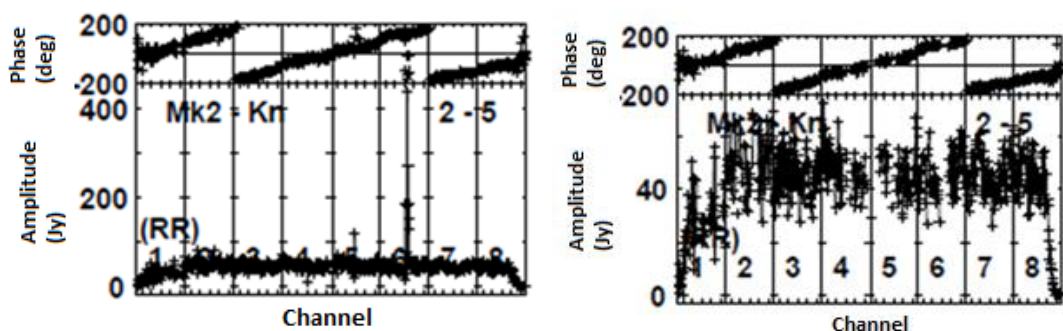
Figure 3.1: Diagrams showing the phase and amplitude before (left) and after (right) flagging on the phase calibrator 0027+5958 on a representative baseline. The top diagram shows the phase against channel and the lower shows the flux against channel. The IFs are indicated across the bottom of each diagram. The diagram on the left shows the data after it had been through the pipeline and had the known faults with the telescopes flagged. In this diagram there is still interference which can be seen as large spikes in the data. On the diagram on the right, the majority of these large spikes have been removed , eliminating obvious interference.

If the RFI is sufficiently strong, it can nonetheless enter the system, creating bright streaks across the data. These bright streaks must be flagged by hand before the calibration process can begin. This operation can be completed in *AIPS* using the commands TVFLG and SPFLG. TVFLG plots the baselines against time for each of the selected IF/channel combinations, to reveal any RFI that has hit particular telescopes at particular times. SPFLG plots channel against time, for each baseline, and can reveal any faulty channels that were used within the observation. Both are useful in finding and removing faulty data.

The data can also be 'clipped' in order to remove any outlying points that were not removed in the flagging runs. This involves setting a limit and removing all points either above or below that limit. Clipping can be done using the *AIPS* program CLIP. It is useful to clip the data after flagging using TVFLG and SPFLG to remove any residual RFI.

3.4.2: Phase Calibration

The next stage in the calibration process is to calibrate the phase delay for each baseline over the duration of the observation. This is necessary because if the phases for the source are not correctly aligned, the resulting synthesised maps will be distorted with both resolution and signal being lost.
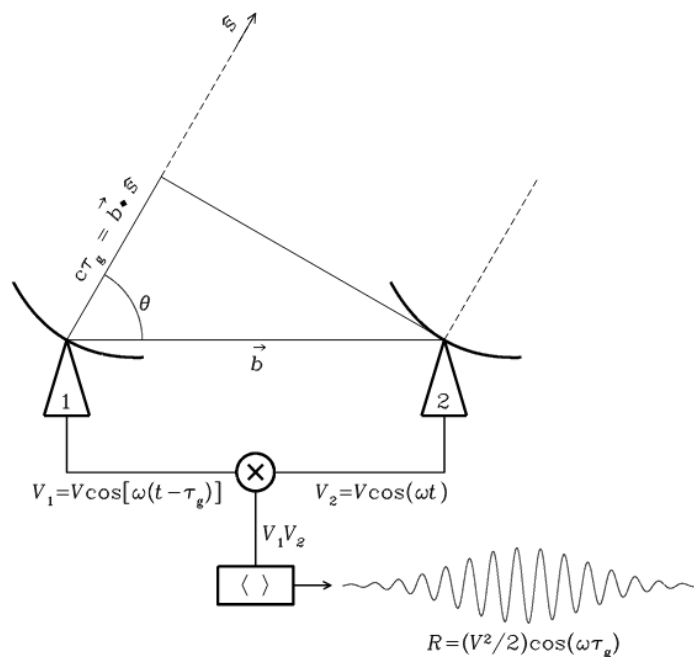
*Figure 3.2: Schematic taken from **Condon & Ransom (2007)** showing a simple two element interferometer system observing in a narrow frequency range centred on $\nu = \omega/2\pi$. The outputs V_1 and V_2 are multiplied and averaged in the correlator to yield an output response R. $\vec{b}$ represents the baseline vector and $\hat{s}$ is a unit vector in the direction of the source. Plane waves must travel an additional $\vec{b} \cdot \hat{s} = b \cos\theta$ to reach antenna 1. At longer baselines, a small change in θ causes a larger change in path length difference compared to short baselines, resulting in a steeper phase gradient.*

If the phase of the raw data is plotted against time, an apparent phase gradient can be seen. This is caused by errors in the geometrical time delays used in the observation. These delays change as the observed source moves across the sky over the duration of the observation. At longer baselines, small shifts in observing angle of the source result in larger changes to the path length difference compared to shorter baselines (see **Figure 3.2**). Therefore, at larger baselines the effect becomes more apparent and the resulting phase gradient is much steeper.

At extremely long baselines such as those in e-MERLIN and in Very Long Baseline Interferometry (VLBI), the phase 'rate' becomes much quicker, that is the phase gradient is much steeper and can go through several full "turns" within a short time span.

This effect needs to be corrected at the start of the phase calibration process using a fringe fitting algorithm. This algorithm searches for patterns in the phase and starts with a Fourier transform approach to find an approximate solution for the phase. This is then followed by a method of least squares to nail down the optimal solution. This process is undertaken by the *AIPS* task FRING. Details of this algorithm can be found in **Schwab & Cotton (1983)**. Theoretically, it is possible to exactly calculate the error due to geometric delay but in practice, errors in the telescope pointing and errors in the propagation time of the signal to the correlator result in residual phase errors.
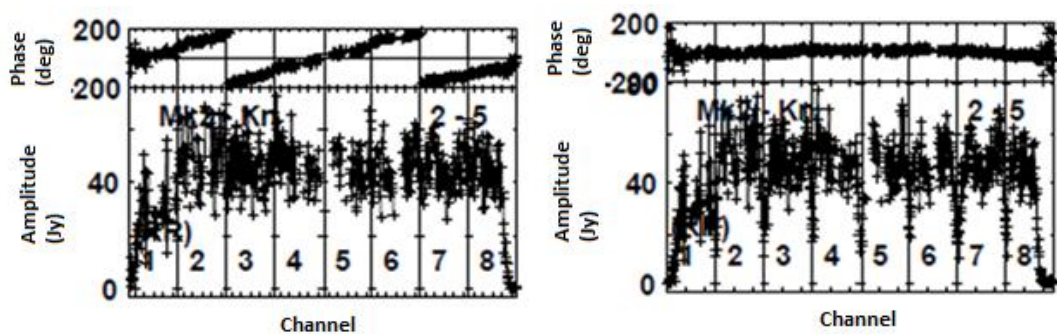
Figure 3.3: These diagrams show the phase and flux of the phase calibrator 0027+5958 on a representative baseline . The top part of both diagrams shows the phase against channel and the lower part of both diagrams show the flux against channel. The IFs are indicated across the bottom of each diagram. The diagram on the left (*3.3a*) shows the phase gradient that is produced before phase calibration and the diagram on the right (*3.3b*) shows the resulting phase after calibration using FRING.

Another source of phase errors that needs to be corrected is a phase gradient that is dependent on the frequency of the observation. This occurs because the interferometer is tuned to observe at a specific frequency, but the observation covers a wide frequency range. As the frequency changes, the path length difference also changes resulting in a slowly changing phase error (see **Figure 3.3a**). This can be corrected for by an additional frequency dependent delay which can be easily calculated.

After correcting for geometric and frequency dependent effects, residual phase errors remain. These errors are caused by errors in the telescope pointing, errors in the time delay used and random fluctuations in the atmosphere (ionosphere). These can be accounted for with the use of the secondary calibrator. The secondary calibrator and the source in question are observed alternately for the duration of the observation. This is so that the telescopes look through the same part of atmosphere for both the observations of the secondary calibrator and source. The phase corrections for these residual phase errors are determined using the *AIPS* task CALIB, using the fact that the phase of a calibrator which is at the centre of the field, should be constant at zero for all observed wavelengths. The corrections between observations of the secondary calibrator are found through interpolation using the task CLCAL. Once the corrections for the secondary calibrator are found, they can be applied to the source itself and remove the major phase errors. Additional steps can be taken to further improve the phase calibration (see section **3.4.5**).

3.4.3: Flux Calibration

Once the phase has been calibrated, it is necessary to calibrate the flux of the sources. This is done through observing a primary calibrator and comparing the instrumental flux to the literature.

Interferometers do not measure the absolute flux of a source. This is because of the Fourier nature of the measurement. As there is no measurement of the u-v plane at (0,0), the total flux within the field observed will integrate to 0. However, it is possible to compare the brightness of a source with another source. This is where a primary calibrator is required.

The primary calibrator is a source which has a known flux which is constant with time. Usually this is an unresolved source as the amplitude should be constant for all baselines in the array, but extended sources can be used with the use of a source model. The primary calibrator is usually observed at the beginning or at the end of an observation. The primary calibrator (and the observed visibilities in general) are observed in instrumental units. This instrument flux is then compared to the physical flux from the literature, in Jy, to determine the conversion factor for the entire observation to physical flux density units (see **Figure 3.4**).
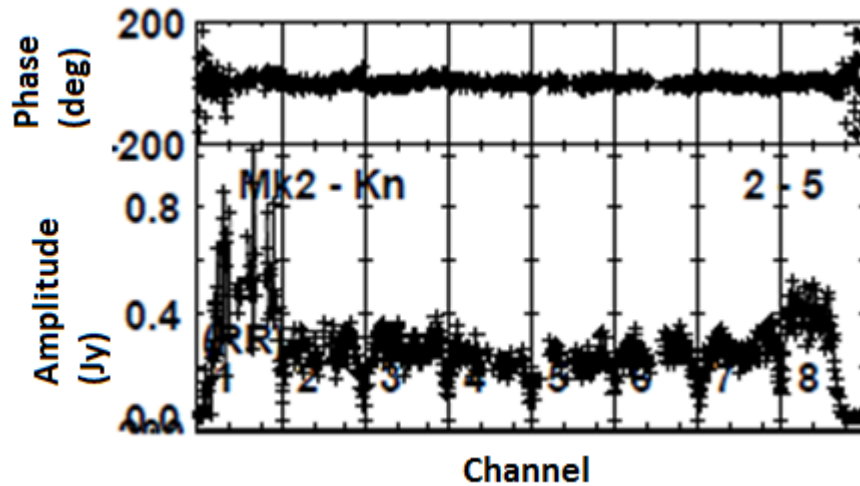
Figure 3.4: *Diagram showing the corrected flux of 0027+5958. The major difference from **Figure 3.3b** is that the scale of the flux has changed to reflect a physical value, i.e. Jy. The flux drops off in-between each IF which represents the bandpass response across each IF and will need to be corrected for before the data is fully calibrated.*

The primary calibrator is used along with the secondary calibrators in a process called 'bootstrapping' to help calibrate the source flux. In this process the same conversion is applied to the secondary calibrator to assign it a physical flux first after which it then can be used as the sole reference for the flux calibration of the source.

3.4.4: Bandpass Calibration

Bandpass calibration is the process of measuring and correcting the frequency dependence of the filter response of each antenna used in the observation. The bandpass calibration is applied to both the amplitude and phase of the filter response.

Bandpass calibration is required to reveal detailed spectral features in radio spectra (see **Figure 3.5**). Bandpass calibration can also be a limiting factor in the dynamic range in a continuum observation. Frequency dependent phase errors can result in positional offsets across the band, with the effect of a slight blurring of the resulting maps.

The bandpass corrections can be found by using the *AIPS* task BPASS. BPASS can work in two separate modes of operation. In the first mode, a full complex bandpass response function (amplitude and phase) can be determined by decomposing the baseline-based cross-power spectra into antenna-based complex functions. This is usually done through a method of least squares and is analogous to self-calibration. In the second mode, the real (amplitude only) part of the bandpass response function can be found by analysing the autocorrelation data.

This mode sets the phase correction of the bandpass function to zero, which is a major limitation.

The bandpass response functions can be best found by observing bright, flat-spectrum sources with featureless spectra. Point sources do not have to be used provided there is sufficient signal on each baseline to reliably determine the bandpass correction. As the bandpass response is inherent to the telescopes themselves, the calibrator does not have to be near the source that is being observed in the sky. Normally the primary calibrator is used for this process.
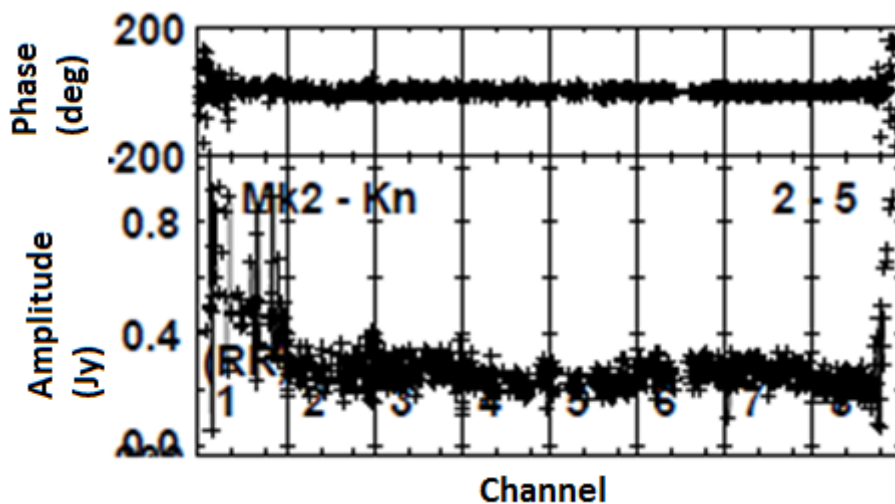
*Figure 3.5: This diagram shows the profile of 0027+5958 after bandpass calibration. Compared to **Figure 4.4**, the profile has been adjusted so that the flux no longer drops between IFs. This diagram shows that IF 1 and the end of IF 8 still contain significant RFI. This data was deleted from the dataset.*

Once the bandpass response functions have been determined, they are applied to the data using the adverb DOBAND in tasks such as SPLIT and SPLAT. This adverb has many options relating to how to apply these corrections to the data.

3.4.5: Self-Calibration

Even after the extensive calibration detailed above, there might still be some small residual errors, most often related to the phase. These errors are associated with the antenna complex gain measurements which vary too rapidly to be calibrated with the calibrator sources alone. In such cases a self-calibration method can be used to fine tune the corrections to further improve the phase calibration.

If the phase calibration is not optimal the resulting images will be distorted. Both resolution and sensitivity will be lost as well, there will be an increase of unwanted sidelobes. If a source has sufficiently high signal to noise ratio, self-calibration can be used to improve the dynamic range of the resulting images. This process can sharpen images, reveal extended emission around bright sources and reveal fainter sources.
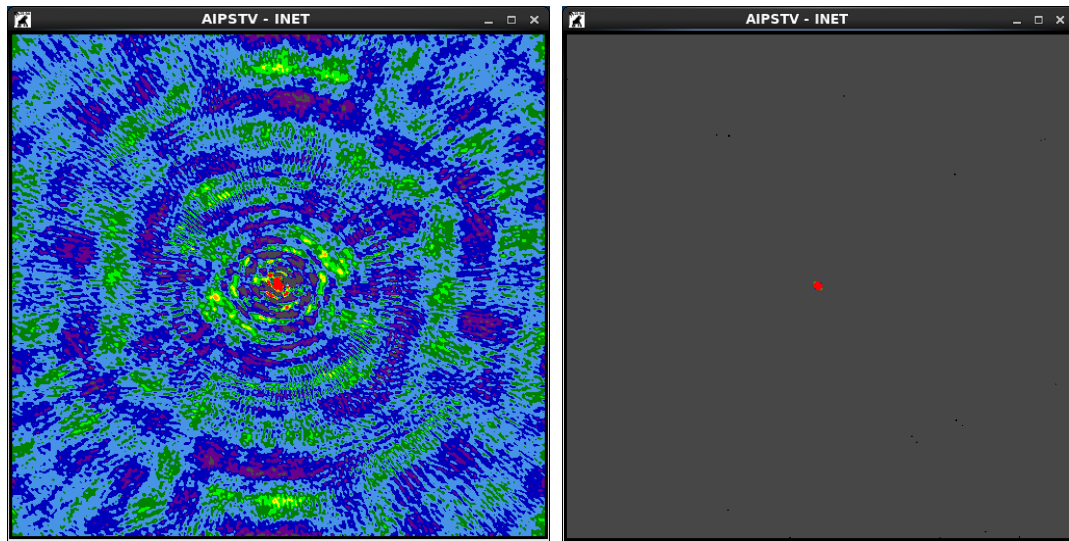
Figure 3.6: *The above images show the effect of self calibration on the phase calibrator 0027+5958. The image on the left prominently shows the source in the centre of the field, but also shows there is a ring of side lobes surrounding the source. The image on the right shows the same source after self calibration. The source is still shown in the centre but the side lobes have now significantly decreased in amplitude. Both images have the same colour scale.*

Self-Calibration is an iterative process which follows a simple algorithm. The steps are detailed below:

1. Make an initial model of the source including constraints on the source structure.
2. Solve for complex gains, resulting in incremental phase (and amplitude) corrections.
3. Apply these corrections to calculate corrected visibilities
4. Form a new model using the corrected data using the same constraints as in step 1.
5. Iterate until satisfied with new model.

Principally, this is done in *AIPS* through the repeated use of the tasks IMAGR and CALIB. As a first step, the data are imaged and cleaned (see section **3.5**). The clean components represent a source model of the sky. CALIB compares the input data against the predictions based on this source model and calculates corrections to the amplitudes and phases. These corrections are then applied to the data to correct it and the data is reimaged and cleaned to form a new model. This new model can then be used again in CALIB to further improve the data. The aim is that the results will finally converge to an optimal value.

The results of self-calibration can be seen in **Figure 3.6**. This technique can only be used if the source has a good signal to noise ratio. If the data is dominated by noise,

and no good source model can be extracted, self-calibration can make matters worse.

3.4.6: Calibration Technique

The calibration techniques indicated above need to be carried out in order to properly calibrate a data set. However, it is important that they are carried out in the correct order, for example, if the flux calibration is carried out before faulty data is removed, the resulting flux measurements on the source will be unreliable.

The general order that calibration is carried out is shown in **Figure 3.7**. Each of these steps is carried out in *AIPS* through the use of tasks. Each of the steps will be discussed in more detail along with explaining the relevant tasks that are used.

Load Data Into *AIPS*

This first stage covers the processes required to convert the raw data collected by the antennae themselves to an *AIPS* friendly format. This is done through the use of tasks such as: FITLD, a task which loads FITS files into *AIPS*, INDXR, a task which indexes the data to speed up access time in *AIPS* and UVFIX which sorts the co-ordinate system of the observation. This step is necessary as without it, there would be no data to calibrate!

Initial Data Editing

The second step in the calibration is to flag and edit the data. This is required to remove particularly noisy data that will cause problems in the rest of the calibration and imaging. This process is described in detail in section **3.4.1**. Initial data editing is done through tasks such as TVFLG, SPFLG and CLIP which can be used to easily find and flag noisy data. The data that is flagged in these tasks is written into the FG (flag) table, a table which keeps a track of the data to be ignored in the rest of the calibration process.

SETJY For The Primary Calibrator

After the data has been flagged, the flux scale for the primary calibrator is set. This is done through the use of the task SETJY. Here the task finds and enters information, from the literature, about the primary calibrator into the SU (source) table. The primary calibrators are well studied sources which do not vary, so a flux density for these sources is known in the literature. This step is further discussed in the section **3.4.3**.
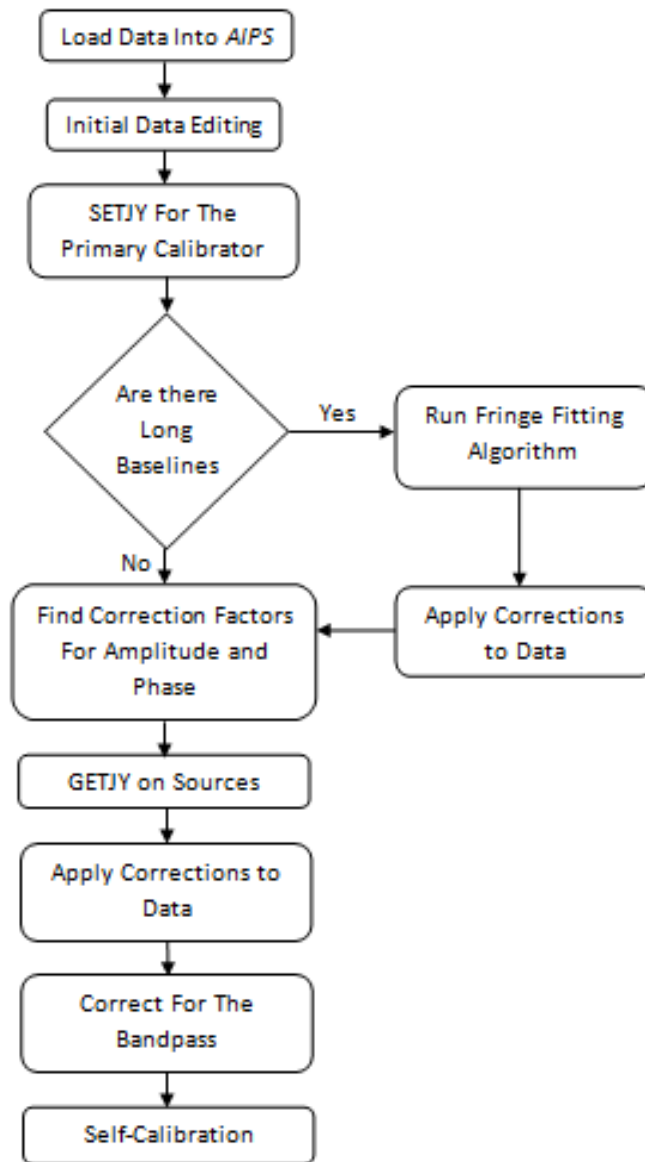
Figure 3.7: *Flow diagram showing the major steps required for the calibration of radio interferometry data.*

Run Fringe Fitting Algorithm

In order to initially calibrate the phase errors associated with the geometric delays in the observation, a fringe fitting algorithm is used (see section **3.4.2**). This error affects all baselines but is more apparent on longer baselines. At shorter baselines, this step can be ignored as the phase rate is much slower and the phase corrections can be found by interpolation. This process is chiefly carried out through the use of the *AIPS* task FRING. The solutions that FRING finds are stored in the SN (solution) table where they can be reviewed. If the solutions are satisfactory, the corrections can be applied to the data through the use of the task CLCAL. CLCAL transfers the solutions from the SN table to the CL (calibration) table. The CL table keeps a track of the solutions that are to be applied to the data.

Find Correction Factors For Amplitude and Phase

The remaining phase error corrections are found through the use of the secondary calibrator. This is done through the use of the task CALIB. This task finds the phase and amplitude corrections required for the secondary calibrator and applies these corrections to the source via interpolation (see section **3.4.2**). The solutions found are written in the SN table.

GETJY on Sources

Now that the amplitude and phase corrections have been determined, the instrument flux still needs to be assigned a physical value. These values are assigned through the use of the task GETJY. GETY uses the results from CALIB in the SN tables to determine the flux density for the secondary calibrator and source and write the results to the SU (source) table. Once the phase and flux corrections have been determined in the SN table, they need to be applied to the calibration table. This is done through the use of the task CLCAL.

Correct for the Bandpass

One of the final stages in the calibration is to correct for the bandpass for each antenna baseline used in the observation. This process is completed through the use of the tasks BPASS and DOBAND and is discussed in detail in section **3.4.4**. The solutions for the bandpass are stored in the BP (bandpass) table and is applied directly to the data.

Self-Calibration

The final step in the calibration of the data is the use of self-calibration. This acts to further modify the phase corrections to an optimal value and is described in detail in section **3.4.5**. This process is described in the self-calibration section. Self-calibration is carried out in an iterative process involving many uses of the task CALIB and CLCAL and acts to improve the dynamic range and sharpen the final maps.

3.5: Imaging

After the calibration of the dataset has been completed, the data needs to be imaged. In this section, the basic imaging algorithm is discussed along with several issues that are related to the imaging of the data.

3.5.1: Imaging Algorithms

In order to create an image of the data, it must first be converted from the raw visibility data to an observed sky brightness. This is done through a Fourier transform. The following was adapted from *Synthesis Imaging In Radio Astronomy II*. From the fundamentals of interferometry section, the Fourier transform relationship between the sky brightness, I, the primary beam pattern, A, and the observed visibility, V is given by:

$$A(l,m)I(l,m) = \int_{-\infty}^{\infty}\int_{-\infty}^{\infty} V(u,v)e^{2\pi i(ul+vm)}dudv$$

The correction for the primary beam pattern can be made easily at the end of the calibration so the quantity $A(l,m)I(l,m)$ will be represented by the modified sky brightness $I(l,m)$.

This equation applies if there is a continuous distribution of visibilities on the (u,v) plane. Practically, it is impossible to measure the entire (u,v) plane with an interferometer (see **Figure 3.8**) and so, the above equation needs to be modified to account for the observed discrete measurements of the (u,v) plane:

$$I^D(l,m) = \int_{-\infty}^{\infty}\int_{-\infty}^{\infty} S(u,v)V'(u,v)e^{2\pi i(ul+vm)}dudv$$

Where I^D is the discrete approximation of the sky brightness otherwise known as the 'dirty image', S is the sampling function and V' is the observed visibility with the prime notation representing that the visibility data is corrupted by noise.

The sampling function is can be expressed in the terms of the two-dimensional Dirac delta function:

$$S(u,v) = \sum_{k=1}^{M} \delta(u - u_k, v - v_k)$$

The Dirac delta functions in the sampling function, $S(u,v)$, correspond to averaged measurements on the (u,v) plane (see **Figure 3.8**).

From Fourier theory, the convolution theorem states that the Fourier transform of a product of functions is the convolution of the individual function's Fourier

transforms. Therefore the 'dirty map' can be represented as a convolution of the sampling function with the visibility function:

$$I^D = F\{S\} * F\{V'\}$$

Here the $F\{\}$ represents the Fourier transform of the function within the brackets and $*$ represents the convolution.
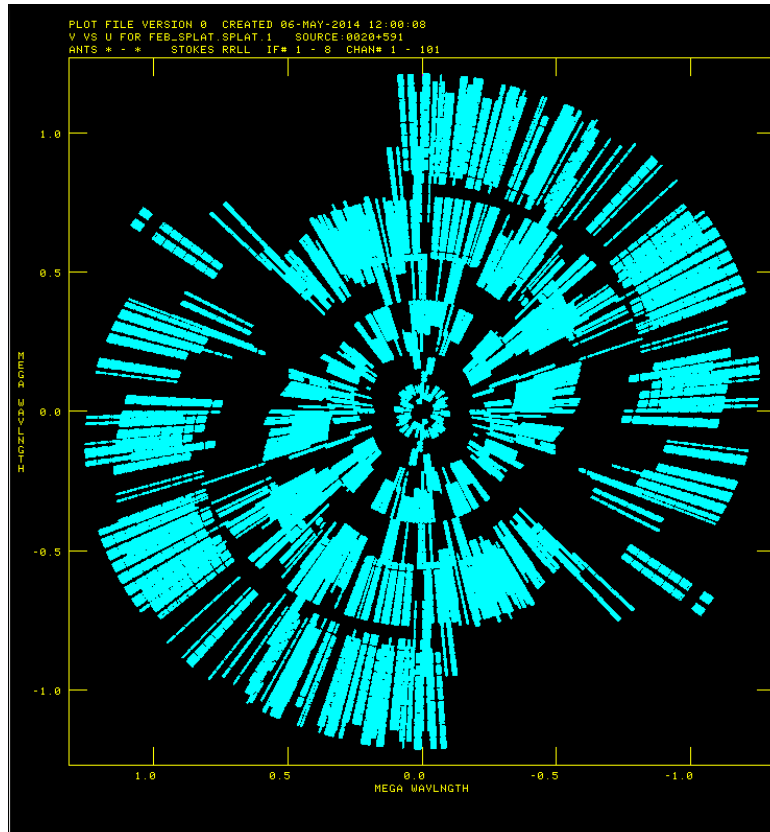
Figure 3.8: *The observed (u,v) plane of the IC10 in the February observation using e-MERLIN. u is plotted on the x-axis and v is plotted on the y-axis.*

The Fourier transform of the sampling function (the dirty beam), however will have a similar form to a sinc function with multiple points in the function having negative values. Therefore the resulting 'dirty map' will be plagued with unwanted sidelobes as a result of the convolution.

Initially interferometers were designed to minimise the sidelobes by measuring a more complete sample of the (u,v) plane (for example, the Westerbork telescope). However algorithms have since been developed to clean the dirty maps of unwanted sidelobes. The basic image cleaning algorithm is detailed in **Högbom (1974)** and follows these steps:

1. Find the strength and position of the peak on the dirty map I^D. If it is required, this can be carried out only on a specified area of the image.

2. Subtract from the dirty image at the position of the peak, the dirty beam multiplied by the peak strength and a damping factor known as the loop gain.
3. Record the position and magnitude of the point source subtracted from the image.
4. Go back to step 1 unless the remaining peak is below a user specified level. What is left of the dirty image is known as the residuals.
5. Convolve the recorded point sources with a clean beam (usually a Gaussian fitted to the central lobe of the dirty beam) to form the cleaned image.
6. Add the residuals from the dirty image to the cleaned image.

A Gaussian is used as a 'clean beam' because it is a well defined function that does not have any negative values. This reduces the negative sidelobes on the maps from the sources themselves that are created from the 'dirty beam'.

This basic algorithm has been extended and improved upon in several ways to speed up the process. A Fast Fourier Transform method is detailed in **Clark (1980)** and a variation working on un-gridded visibility data is detailed in **Schwab (1984)**.

In *AIPS*, the Fourier transform and cleaning is carried out in the task IMAGR. The position and magnitude of the point sources are noted in the Clean Components (CC) table and the clean is carried out using an algorithm described in **Schwab (1984)**. This algorithm also notes negative clean components in the CC table, but this is normally a correction for too much flux being removed from a cell or an attempt to represent a point source which does not lie on a grid cell. CC filtering can be used to remove these negative clean components.

3.5.2: Source Subtraction

Often when imaging wide fields, bright unwanted sources (confusing sources) are also imaged. These sources contribute unwanted sidelobes which can significantly increase the noise in the region of interest. In order to image the interesting region with greater sensitivity, the confusing sources must also be imaged and cleaned to remove their unwanted sidelobes.

There are several solutions to remove the effect from these unwanted sources. A simple solution is to image the entire region and restrict the deconvolution to the areas of interest. This solution however is very computer intensive and not very practical. A faster solution is to only image the regions of interest along with the confusing sources. This reduces the area for deconvolution, improving the computational time, but is only useful if the majority of the wide field is empty. There exists an even better solution where the unwanted sources are simply removed from the (u,v) dataset, removing the unwanted sidelobes entirely. This

removes the need to image the bright sources every time the region of interest is imaged, saving time.

In order to remove confusing sources from the (u,v) dataset, they must first be imaged to yield clean components. These clean components represent the model of the source to be removed. This model is inverse Fourier transformed and is then subtracted from the (u,v) dataset. In the optimal case, this will remove the bright unwanted source entirely from the dataset. In reality however, the model will not perfectly match the source due to noise. The cleaning algorithm cleans down to a level just above the noise, so there will be some remnants of the source which are known as residuals in the final map. Although these residuals are unwanted, the sidelobes they produce are small and indistinguishable from the general map noise. The results of subracting a source can be seen in **Figure 3.9**.
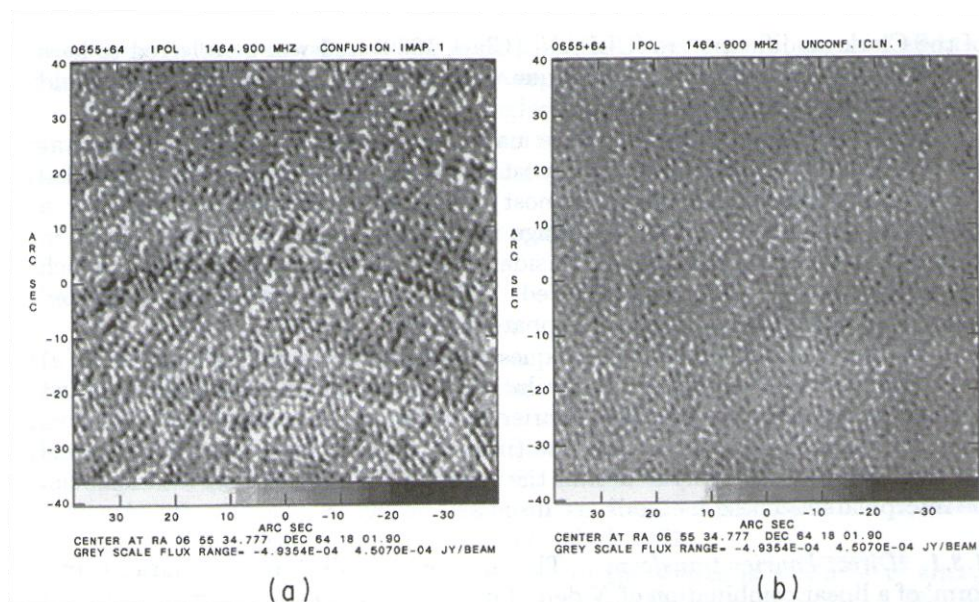
Figure 3.9: Diagrams taken from **Taylor et al. (1999)** *showing the region around a pulsar observed with the VLA at 1.4 GHz. The diagram on the left shows the interfering sidelobes from bright distant sources. The diagram on the right shows the same region as the diagram on the left but with the bright unwanted source removed. The rms noise level in the left diagram is 109 μJy and is 62 μJy on the right, showing that source subtraction greatly reduces noise due to sidelobes in the final image.*

 In *AIPS*, this is done through the use of the task UVSUB which subtracts the model from the (u,v) dataset.

3.5.3: Curvature of the Sky Problem

Because of the Fourier nature of synthesis imaging, an unusual co-ordinate system is required to construct synthesised images. Baselines within the array have components (u,v,w) where w points in the direction of interest (towards a position s_0 which will become the centre of the synthesised image), and u and v are in directions to the East and North. Each of these co-ordinates is dimensionless and measured in units of wavelength at the centre frequency of observed bandwidth.

Positions on the sky are defined in a different co-ordinate system with components (l,m,n) where l and m are direction cosines measured with respect to the u and v axis and n is a directional cosine with respect to the w axis. A synthesised image in the (l,m) plane represents a projection of the celestial sphere onto a tangent plane at the (l,m) origin (see **Figures 3.10 & 3.11**).

Distances in l and m are proportional to the sines of the angles measured from the origin. In these co-ordinates, it can be shown that:

$$\frac{v\mathbf{b} \cdot \mathbf{s}}{c} = ul + vm + wn$$

$$\frac{v\mathbf{b} \cdot \mathbf{s}_0}{c} = w$$

$$d\Omega = \frac{dldm}{n} = \frac{dldm}{\sqrt{1 - l^2 - m^2}}$$

where v is the frequency observed at, $\mathbf{b}$ is the baseline vector, $\mathbf{s}$ is the vector representing the direction of observation and c is the speed of light.

Using these co-ordinate systems, the complex visibility of a source can be expressed as:

$$V(u, v, w) = \int_{-\infty}^{\infty} \int_{-\infty}^{\infty} A(l, m) I(l, m) e^{-2\pi i [ul + vm + w(\sqrt{1 - l^2 - m^2} - 1)]} \frac{dldm}{n}$$

Where A is the normalized antenna reception pattern and I is the intensity distribution (map).

If the field to be observed is small enough, that is:

$$\left(\sqrt{1 - l^2 - m^2} - 1 \right) w \approx -\frac{1}{2} (l^2 + m^2) w \approx 0$$

That is the w term can be ignored and the 3-dimensional Fourier transform simplifies to 2-dimensional Fourier transform . This approximation can be used to image compact sources quickly and accurately.
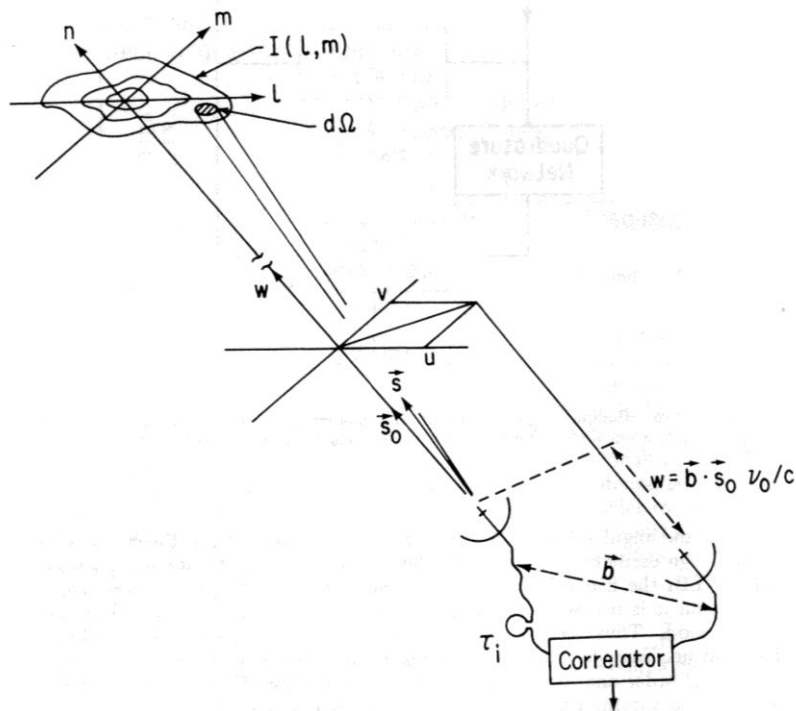
*Figure 3.10: Schematic taken from **Taylor et al. (1999)** showing the two different co-ordinate systems used in synthesis imaging. The (u,v,w) co-ordinates are used to express the interferometer baselines and (l,m,n) are used to express the source brightness distribution.*

In wide-field imaging however, this approximation breaks down and errors due to image distortions can arise if the *w* term is ignored. These errors manifest themselves as positional errors (smearing) in the synthesised maps (see **Figure 3.11a**) with sources farther from the phase-tracking centre suffering more than those close to the phase centre and is due to the projection errors of a curved surface on a flat plane. Another distortion that arises is that the *w* term introduces phase errors which in turn result in a position shift. For a summary of these issues see **Clark (1973)**.

There are several techniques that can be used to avoid this distortion. The simplest solution is to use the 3-dimensional Fourier transform to find the intensity distribution. However, this solution is extremely CPU intensive and it is not practical to be used for wide-field imaging.

A less computer intensive solution is to mosaic the images. Many smaller fields, taking advantage of the small field approximation, are centred on regions of interest. The data is modified so that for each imaging run, the centre of each smaller field becomes a new phase tracking centre. This minimises the distortions for the sources of interest but the sources relative positions are still distorted.
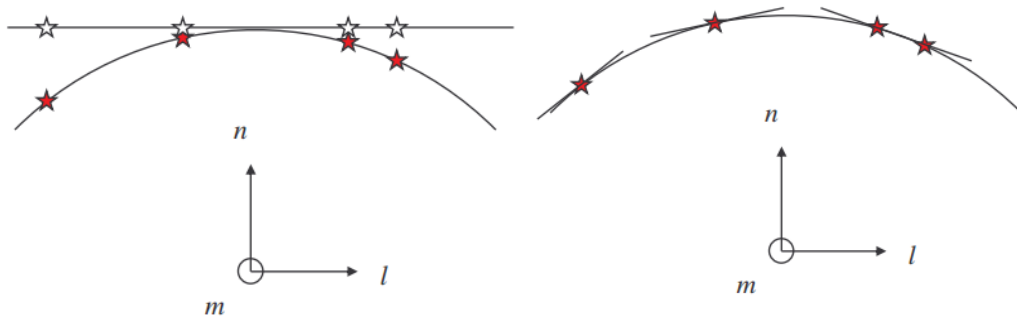
Figure 3.11: *The diagram on the left (**3.11a**) shows the positional distortions that arise if the w term isn't taken into account. The red stars represent discrete sources as a part of the sky brightness and the white stars show the positions of the sources recovered after projection. The projected separation is different from the actual separation. The diagram on the right (**3.11b**) represents the results from the faceted solution. The distortions due to projection are almost entirely removed.*

A final solution is to use facets so that the curvature of the sky can be represented by many smaller tangent subfields, centred on regions of interest (see **Figure 3.11b**). The centre of each sub field has the correct *n* position. This solution is still limited by the small field approximation so distortions do arise if these subfields get too big. This solution is a good compromise between 3-dimensional Fourier transforming and mosaicing as relative positions are preserved along with being relatively computationally inexpensive.

3.5.4: Primary Beam Attenuation

After imaging, the maps produced have still to be corrected for primary beam attenuation. For instruments where all of the dishes are identical, for example the JVLA, the primary beam is well defined as it corresponds to the power pattern of an individual element. If a model of the primary beam is available, the final maps can be easily corrected by simply dividing by the primary beam pattern.

For e-MERLIN however, there is a wide range of dishes with varying shapes, such as the elliptical Mark II telescope and the 80 m Lovell telescope. This means that the primary beam is much harder to define and varies on a per baseline basis.

Many additional factors must be taken into account to find the exact primary beam such as the frequency the observation was taken at (**Wrigley 2011**). When analysing very wide-band observations, the primary beam pattern changes appreciably across the band.

From the e-MERLIN observation guide, the primary beam without the Lovell telescope can be approximated by a Gaussian with a FWHM of 30 arcmins at a frequency of 1.5 GHz (see **Figure 3.12**). If the Lovell telescope is included, the primary beam would need to be evaluated on a per baseline basis.

IC10 is roughly 10 arcmins across, which is comfortably smaller than the FWHM of the correcting Gaussian. At the maximum distance from the centre of the galaxy, the correcting factor is roughly 4% so, primary beam corrections will not dramatically alter the results. Nonetheless, the correction factors for each of the detected sources are applied in **Table 4.4**. The primary beam correction becomes more important when wider fields are considered.
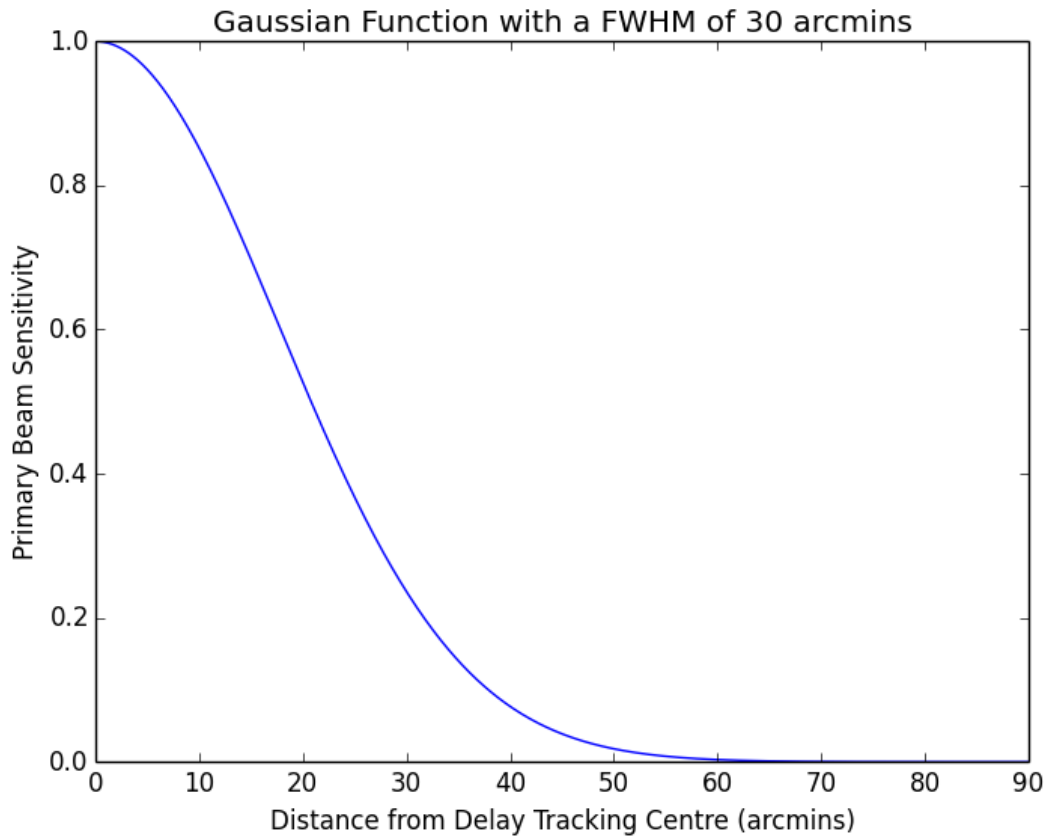
Figure 3.12: *Diagram showing the primary beam approximation that can be used to correct maps from primary beam attenuation. This Gaussian function has a FWHM of 30 arcmins.*

3.5.5: Averaging

A further step that can be taken in the calibration of the data is to average the data. The data can be averaged in bandwidth and/or time to dramatically speed up the imaging process. However distortions can arise if the data are averaged too much. These distortions are a function of angular distance from the delay and phase tracking centres of the synthesized images, and as a result will not be removed by cleaning algorithms or self calibration. If the data are averaged too much smearing occurs. There are two types of smearing, bandwidth smearing and time-averaging smearing , both are briefly discussed here:

Bandwidth Smearing

Modern interferometers observe with wide bandwidths split into several sub bands known as IFs (Intermediate Frequencies), with each IF being split into many narrow channels. Observing in this format has many advantages including improving the sensitivity of an observation (wide bandwidth) and enhancing (u,v) plane coverage, resulting in a cleaner synthesized beam. The sensitivity is improved simply because more data is being taken and the (u,v) plane coverage enhancement can be understood as follows. The easiest way to gain better (u,v) coverage is to move the telescopes. This is not practically feasible, however altering the observed frequency has the same effect. Imaging over a wide bandwidth is analogous to measuring with many antenna at many different baselines and in effect fills in the (u,v) plane. Many channels, covering a wide frequency range are used as well in order to gather spectral index information about the source that is being observed.
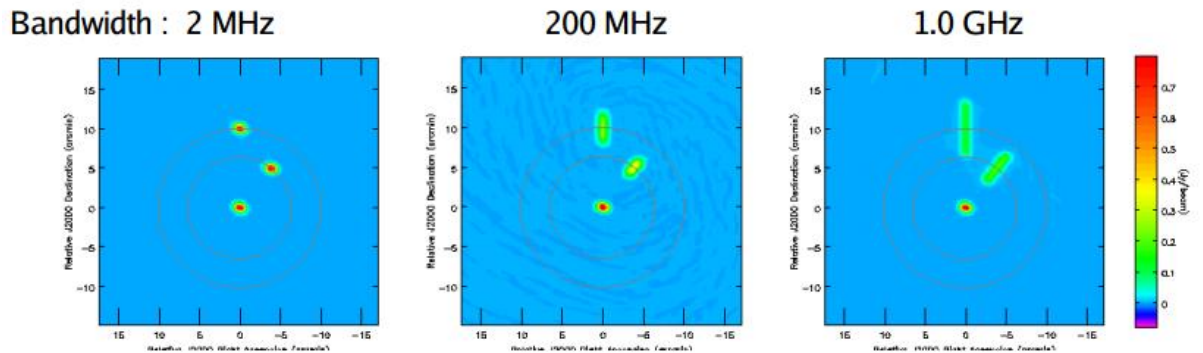
*Figure 3.13: Exaggerated schematic, taken from **Rau (2012)**, showing the effect of bandwidth smearing on 3 sources being observed at 2 GHz. The number above each diagram represents the bandwidth used for each observation and the contours represent 5 and 10 arcmin distances from the delay tracking centre. As it can be seen, larger bandwidths result in more bandwidth smearing.*

One of the main drawbacks of using a wide bandwidth is that the datasets get very large resulting in long computational times. One way to improve this is to average channels. Averaging visibilities over the observed bandwidth is equivalent to averaging over a radial region in the (u,v) plane. If the response of the interferometer varies significantly through this area, the structure corresponding to this variation will be reduced in amplitude and distorted. This effect is known as bandwidth smearing and can be seen in **Figure 3.13**.

On the (u,v) plane, frequency is indirectly plotted in the radial direction from the centre. Therefore after Fourier transformation, the resulting distortion from over-averaging is also in the radial direction, centred on the delay tracking centre. From arguments in **Taylor et al. (1999** Chapter 18), it can be shown that the smeared intensity distribution, $\tilde{I}(l,m)$, is given by:

$$\tilde{I}(l,m) = \int_0^\infty (B * I) \left(\frac{l\theta_0}{\sqrt{l^2+m^2}}, \frac{m\theta_0}{\sqrt{l^2+m^2}} \right) D \left(\sqrt{l^2+m^2} - \theta_0, \theta_0 \right) d\theta_0$$

Where B represents the dirty beam, I, represents the true intensity distribution and D is called the bandwidth distortion function. θ_0 is the radial co-ordinate of the delay tracking centre.

The bandwidth distortion function, D, only depends on the radial distance from the delay centre, with the width and amplitude of the distortion being dependent on radial distance and on the shape of the passband used in the observation. That is, sources far from the delay tracking centre are smeared more than those closer (see **Figure 3.13**).
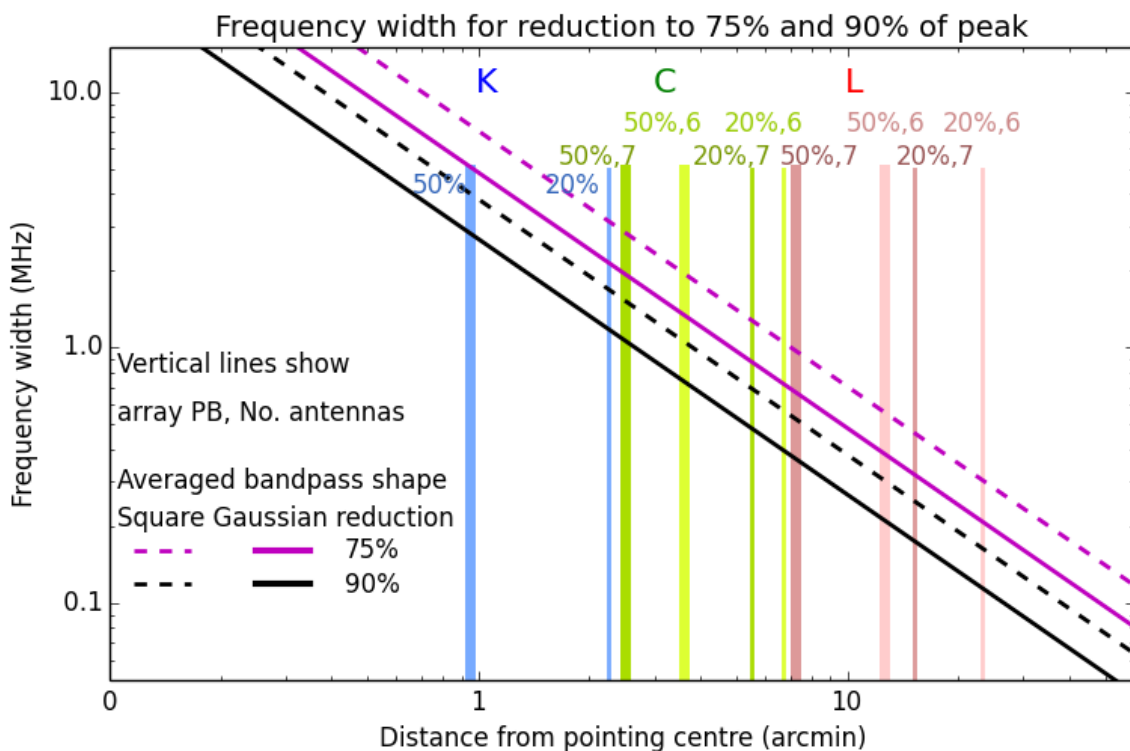
Figure 3.14: *Diagram produced using code developed by Anita Richards, showing how to minimise bandwidth smearing in e-MERLIN. The x-axis shows the distance from the pointing centre of the observation and the y-axis shows the frequency width averaged to. The vertical lines represent the primary beam in different wavelengths with different numbers of antennas. The diagonal lines represent the amplitude reduction due to averaging for different filter shapes with the solid line representing a Gaussian bandpass and the dotted line representing a square bandpass . The black lines represent a 10% amplitude reduction and the purple line represents a 25% reduction .*

The simplest way the distortion can be managed is by selecting the number of channels to average over so that the region of interest of the image remains undisturbed. If an affected source is not directly of interest, it can still be imaged and subtracted from the uv-data to reduce the sidelobes from the interesting region. For e-MERLIN, diagrams such as **Figure 3.14** can be used to estimate the degree of bandwidth smearing an image will sustain.

Time-Averaging Smearing

Aperture synthesis maximises (u,v) plane coverage using the Earth's rotation to change the locations of the constitute interferometers on the (u,v) plane. As a result, observation runs normally last for several hours and datasets get very large. To record the data and synthesize maps practically, the time needs to be averaged. Larger averaging intervals improve the computational time but over-averaging results in a distortion known as time-averaging smearing.

On the (u,v) plane, projected baselines rotate with time (as the Earth rotates) leading to elliptical tracks. After Fourier transformation the resulting distortion will be azimuthal, and the smearing will be perpendicular to bandwidth smearing (see **Figure 3.15**). This distortion will also be centred on the phase tracking centre of the image. As the phase of the response varies increasingly rapidly with distance from the phase-tracking centre, so too will the extent of smearing increase with distance from the phase-tracking centre. In other words, sources that are located far from the centre of a synthesized map will suffer more greatly from time-averaging smearing.
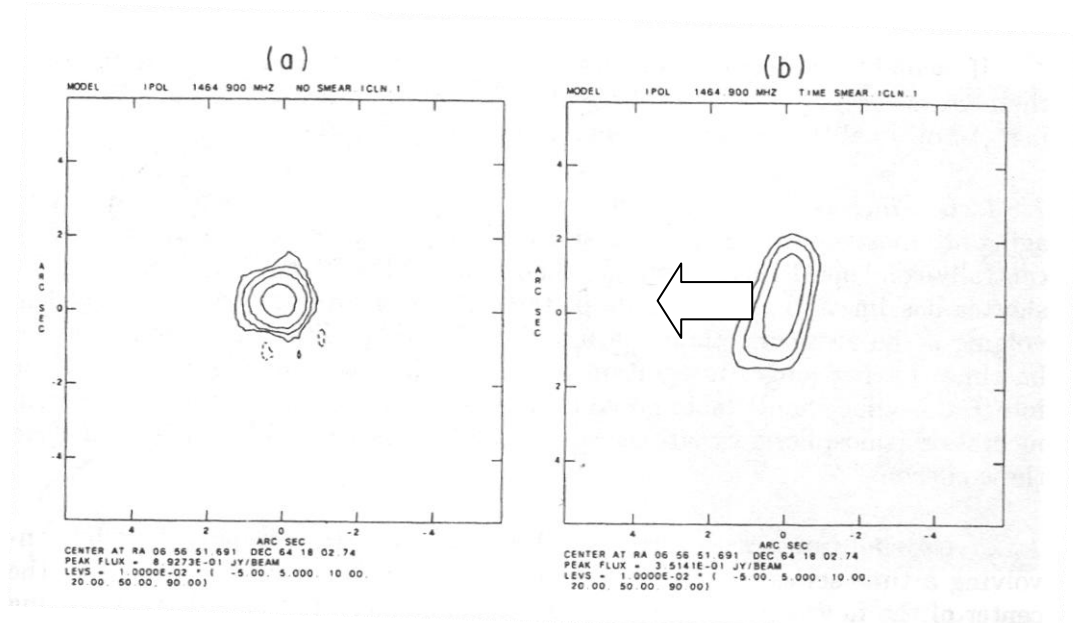
Figure 3.15: Images showing the effect of time-average smearing on a points source located ~500 synthesized beam widths west of the phase-tracking centre. The arrow represents the direction to the phase-tracking centre. The diagram on the left shows a cleaned image of a point source without time-averaging smearing and the image on the right shows the time-averaging smeared image. This diagram was taken from **Taylor et al. 1999**.

If a source is at a celestial pole, the (u,v) tracks traced out are circular with an angular velocity equal to that of the Earth's rotation. Samples of the (u,v) plane taken at longer baselines will be travelling faster than those at smaller baselines. Therefore longer averaging times result in longer baselines suffering more from time-averaging smearing than shorter baselines.

There are several techniques used to combat time-average smearing. The simplest way is to have very short averaging intervals. This will greatly reduce the smearing effect at the cost of computational time. Another solution is to take advantage of the baseline dependence of the distortion. Baseline dependent averaging can be used to reduce the volume of data by increasing the averaging interval at shorter baselines and having a shorter averaging interval at longer baselines. This has the advantage of reducing the amount of data whilst reducing the effects of time-averaging smearing.

Another solution that can be used is to image multiple fields on the sources of interest. As the distortion is a function of the separation from the phase-tracking centre, the phase-tracking centre can simply be moved before averaging to the other source. A large drawback of this technique is that multiple copies of the averaged dataset must be kept in order to see multiple sources. This technique only becomes practical if there are only a few sources and the averaging is large.
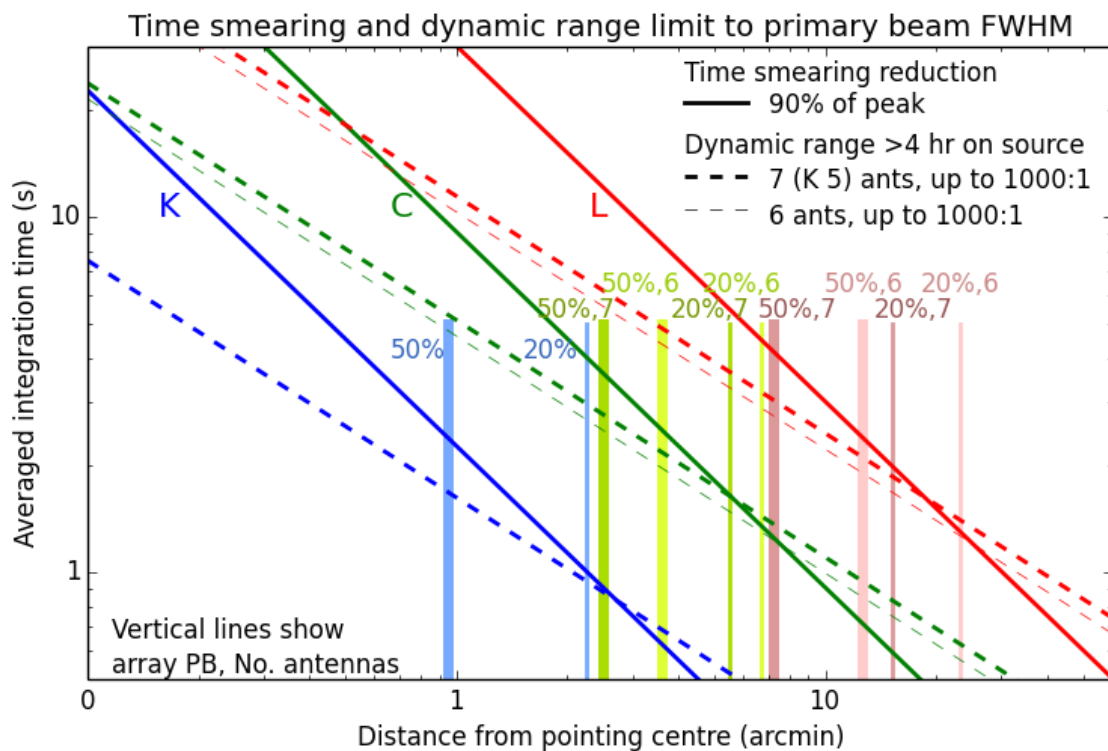
Figure 3.16: Diagram produced using code developed by Anita Richards, showing the extent of time smearing on e-MERLIN. The x-axis shows the distance from the pointing centre of the observation and the y-axis shows the averaging time interval. The vertical lines represent the primary beam at different wavebands with different numbers of antennas. The solid diagonal line represents a 10% amplitude reduction at different wavebands and the dotted line represents the a dynamic range of 1000:1 for different numbers of antennas.

Averaging time intervals for e-MERLIN can be determined by using diagrams similar to **Figure 3.16**.

3.6: Summary

Now that the interferometry data has been calibrated and imaged, it can now be used for scientific purposes. The steps described highlight the major steps required for the calibration although additional steps can be taken to correct for problems that can affect individual datasets.

4: Observations and Results

4.1: Observations

The observations of IC10 were carried out at 20cm wavelength (1.5 GHz) using the e-MERLIN (Multi-Element Radio Linked Interferometer Network) array in two observing runs, one in February 2013 and the other in November 2013. Both observations use 8 intermediate frequencies (IFs), each consisting of 128 channels at 500kHz resolution resulting in a total bandwidth of 512MHz. There were differences in each observing run which are detailed below:

February 2013

This observation was taken on February 9th 2013 with all telescopes operational for the duration of the observation. Over the 12 hour duration of the observation, the secondary calibrator 0027+5958 and IC10 were observed alternately, with 5mins on IC10 and 1 min on the secondary calibrator. The primary calibrator 0555+398 was observed at the start of the observation.

November 2013

This observation was taken on November 22nd 2013. For this observation, all telescopes apart from Cambridge were operational. Baselines with this telescope result in the largest baselines within the array, their absence causing a loss of both resolution and sensitivity compared with the February observation. However the observing consisted of 20 hours taken over a 3 day period. This observation follows the same pattern as the February observation using the same secondary calibrator, 0027+5958, with the primary calibrator 0555+398 being observed at the beginning of each run.

4.2: Data Reduction

The data from each observation were calibrated independently using the methods discussed in the calibration technique section of the thesis. Different problems were found with each data set and are detailed below:

February 2013

The calibration for the February dataset had very few problems. The calibrated data has some residual noisy visibilities which can be seen in **Figure 4.1**. There are very few of these left within the data (probably due to residual RFI) and so no additional attempt was made to remove them. After calibration, initial maps had a noise level of 35μJy.
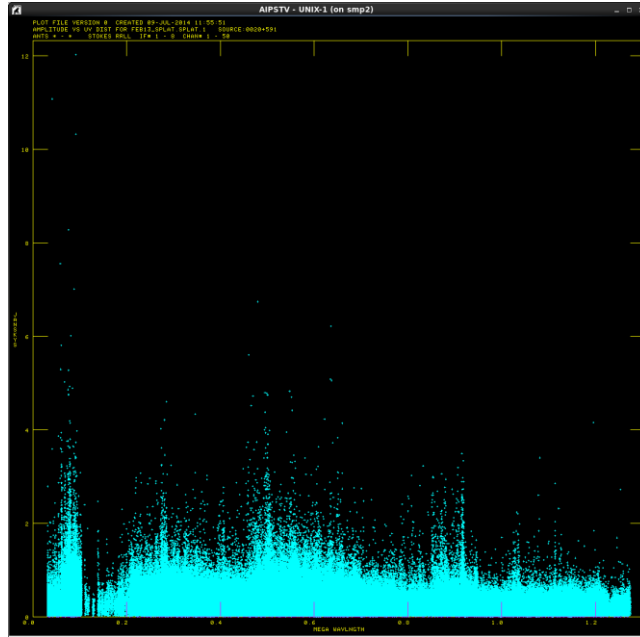
Figure 4.1: Diagram showing the February visibilities of IC10 plotted with baseline length on the x-axis and flux density plotted on the y-axis. The majority of the amplitudes lie below 4 Jy but there are still some visibillities which lie above this. These points are ascribed to RFI that has remained through the calibration process.
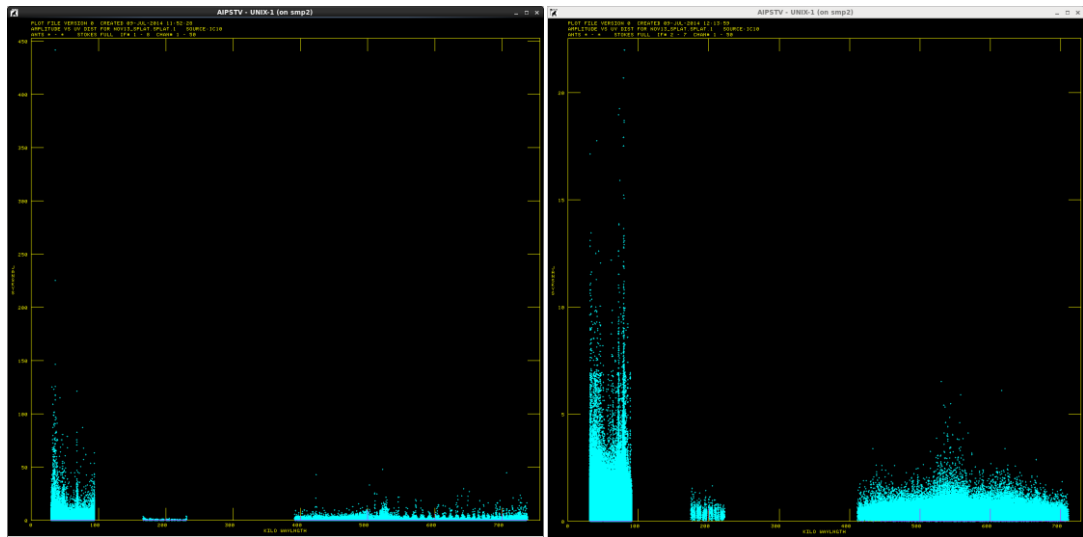
Figure 4.2: Diagrams showing the November visibilities of IC10 plotted with baseline length on the x-axis and flux density plotted on the y-axis. The diagram on the left shows the result if all the visibilities are plotted. The flux density measured at short baselines is much larger than that measured at longer baselines. The diagram on the right (note the difference in scales) shows the same visibilities if IFs 1 and 8 are removed. There is a slight improvement as some of the unreasonably large values are removed but there is still a spike in the flux density measured at shorter baselines. From the February 2013 dataset, we know this is not due to extended emission.

November 2013

The November dataset has many issues. Initial imaging revealed that the map has a noise level of 28μJy, however imaging of individual sources revealed that the flux density level is almost double that of the February dataset. Inspection of the visibilities taken in the November dataset (see **Figure 4.2**) revealed that there is still

a large amount of residual RFI-like noise. Removing particularly noisy IFs slightly improves the situation but the quality of the remaining data is still unacceptable. This may be the cause as well of the problems with the flux density calibration of this dataset. Although the flux density measurements remain unreliable, the positions of the sources and their morphology can still be trusted. Further scrutiny of the November dataset is planned for the near future.

Comparison of the flux density of the calibrators observed in these observations with the literature revealed that the February dataset is more likely correct and so, the rest of the analysis will be carried out using this dataset.

Source Subtraction

Many of the sources that were detected are background galaxies that only contribute unwanted sidelobes to the region of interest. In order to improve the final maps, these unwanted sources were removed from the (u,v) data. These sources were assumed to be no part of IC10 as they were located sufficiently far (>10 arcmins) from IC10 or they were identified in the literature as not associated with IC10. They are detailed in **Table 4.1**. These flux density values have not been corrected for primary beam attenuation.

Literature Name	RA (J2000)	DEC (J2000)	Peak Flux Density (mJy)	Integrated Flux Density (mJy)
NVSS J001914+592008	00 19 14.296	+59 20 08.199	0.179	1.38
NVSS J002008+591327	00 20 08.418	+59 13 30.381	0.233	0.716
NVSS J002100+591659	00 21 01.630	+59 17 00.886	0.690	1.83
NVSS J002108+591132	00 21 08.800	+59 11 33.444	4.39	12.0
NVSS J002146+591234	00 21 44.867	+59 12 38.141	0.330	1.34
NVSS J002152+592606	00 21 52.423	+59 26 05.938	0.484	2.71
NVSS J002204+591057	00 22 04.872	+59 10 58.005	0.385	1.05
NVSS J002054+591101	00 20 54.460	+59 10 51.318	0.986	2.14

Table 4.1: Properties of sources that were subtracted from the (u,v) datasets for both the February and November datasets. The results shown were taken from the February dataset. Each of the sources correspond to an NVSS source (**Condon et al. 1998**).

Averaging

After calibration, the data for IC10 was split from the data for the primary and secondary calibrators and averaged to improve the computational time. Using the averaging diagrams produced at e-MERLIN (see section **3.5.5**), the data was time averaged at intervals of 4.5s and every 2 channels were averaged together. Furthermore the first and last 10 channels within each IF were removed as these channels are increasingly noisy as the edge of the bandpass is approached.

Background Sources

One problem that affects studies at radio wavelengths is contamination from background sources. If a source is resolved, it is usually relatively simple, based on

its morphology to decide whether it is a contaminating background source or not. However, when unresolved they become indistinguishable from sources of interest. Therefore it is important to know roughly how many contaminating background sources with flux densities comparable to those expected to be found in IC10, we would expect to see in the area that IC10 occupies in order to assess the degree of contamination. Fortunately some of the brighter sources have already been classified and determined to be unassociated with IC10 (see **Table 4.1**) but fainter, unresolved sources that are unaccounted for in the literature can still pose as sources belonging to IC10.

One method used to determine the number of background sources is to use source counts from the literature. Source count plots present the typical number or radio sources per steradian as a function of flux density at a given frequency. Historically, source counts are used to probe cosmic evolution, but can also be used to estimate the number of expected sources in a given area of sky assuming that the Universe is isotropic and homogeneous. Through the analysis of the source counts presented in **Windhorst (2003)**, we would expect to find roughly 20 total background sources within a circular field of diameter 10 arcmins centred on IC10 with roughly 19 which could be confused with actual sources based on their expected flux densities. If we constrain this field of view to just the area that contains extended 20cm radio continuum emission (**Heesen et al. 2011**), this number reduces to roughly 9 total sources with 8 that can be confused with actual sources.

These values should thought about as an upper limit of the number of background sources that could be confused with sources within IC10. As e-MERLIN is only sensitive to very compact regions, many of these background sources will be resolved out and will not be observed. Additionally if we consider only radio sources that could be co-incident with regions of H-alpha emission, this number will reduce further as the effective area over which contamination would be occurring shrinks quite dramatically.

In the future, an additional test that could be performed is to use the data itself to estimate the number of background sources within IC10. This can be achieved by imaging a wide field around IC10 and counting the number of sources in the field that have a flux density greater than 3 times the local noise, i.e., the same criteria as used for those sources that are considered genuinely to belong to IC10. If we only consider sources out to where the primary beam attenuation is modest, we can count the number of sources that are not associated with IC10 and use this to infer how many contaminating sources would be expected in the field containing IC10.

All of the resolved sources, apart from source 6, are clearly associated with H-alpha emission which leads confidence to the assertion that these sources are a part of

IC10. However, some of the unresolved sources could more easily be mistaken for background galaxies. For the purpose of this study, we will assume they are all a part of IC10 because they are coincident with extended emission found in lower resolution maps (see **Heesen et al. 2011**) but in any future study, more care will be needed to be taken to demonstrate these sources are part of IC10.

4.3: Resulting Maps

The final map created from the data is shown in **Figure 4.3**. This map is created from a combination of the February and November datasets. Although the flux scale from the November dataset is not necessarily reliable, the positional data is unchanged and the map can be used to search for sources.

Sources were counted as being detected if they have a flux greater than three times the background noise of the map. Due to the large baselines in the e-MERLIN array, most of the extended emission is resolved out leaving only bright compact sources. The created maps mirror this with the maps being sparsely populated with bright compact sources. All of the sources found within this map are assumed to be a part of IC10. Most of the sources within the map are un-resolved.

Contour maps of individual sources can be found in **Figure 4.4**. These contour maps were created exclusively using the February dataset so that the flux scale is deemed reliable.

4.4: Data from Maps

The general properties of the sources derived from the maps is summarised in **Table 4.2**.

Source	RA (J2000)	DEC (J2000)	Peak Flux Density(mJy)	Integrated Flux Density (mJy)	Resolved?
1	00 20 17.268	+59 18 40.210	0.326 ± 0.043	15.5 ± 0.831	Resolved
2	00 20 27.153	+59 17 06.019	0.375 ± 0.041	4.54 ± 0.492	Resolved
3	00 20 26.805	+59 18 43.662	0.975 ± 0.074	0.975 ± 0.074	Unresolved
4	00 20 26.970	+59 17 28.722	0.566 ± 0.043	5.38 ± 0.651	Resolved
5	00 20 08.345	+59 15 40.262	1.09 ± 0.064	1.09 ± 0.064	Unresolved
6	00 20 14.937	+59 18 53.663	0.185 ± 0.040	8.06 ± 0.452	Resolved
7	00 20 19.332	+59 18 02.371	0.692 ± 0.19	0.692 ± 0.19	Unresolved
8	00 20 33.379	+59 19 42.896	0.233 ± 0.062	0.233 ± 0.062	Unresolved

Table 4.2*: Table showing the general properties of the sources associated with IC10 within the field observed. Size parameters of resolved sources are detailed in **Table 4.3**.*

Size measurements for the resolved sources are given in **Table 4.3**. Unresolved sources will be assumed to be much smaller than the convolving beam (0.19" x 0.16" or a physical size of 0.66 pc x 0.53 pc). Sources that are the same size as the convolving beam will appear resolved with a size a factor of $\sqrt{2}$ times larger than the convolving beam. For a further discussion on the sizes of the unresolved sources, see Section **5.4**.

Flux errors in **Table 4.2** for unresolved sources were found through the use of the *AIPS* task IMFIT, a program which fits a Gaussian to the data. Errors for resolved sources were estimated through the use of the task TVSTAT, a task which allows flux determinations to be found for sources of unusual morphology.

The dimensions of sources in IC10 (see **Table 4.3**) were found through the use of the task TVDIST. Errors were estimated from inaccuracies where the extended emission from each of the sources ends.
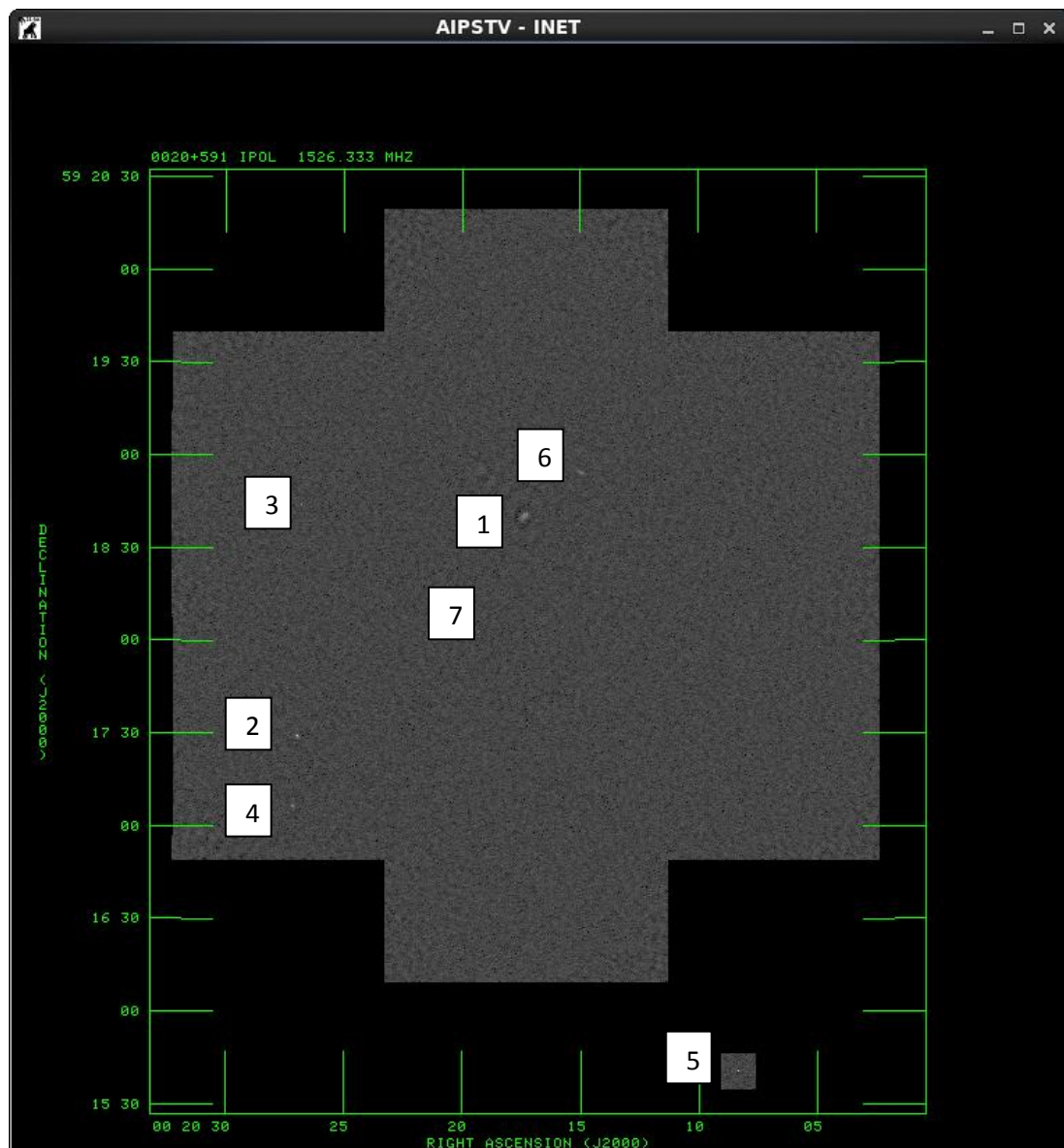
Figure 4.3*: Combined image from both the February and November data of the central region of IC10 taken at 20cm. One major source that was not included in this image has been added in the lower right corner of the image . The map has a resolution of 0.271" x 0.197" and has an rms of 27μJybeam[-1]. The sources are numbered according to the contour maps in **Figure 4.4** and **Table 4.2** with source 8 being located off to the north-west of the field . This map has not been corrected for primary beam attenuation.*
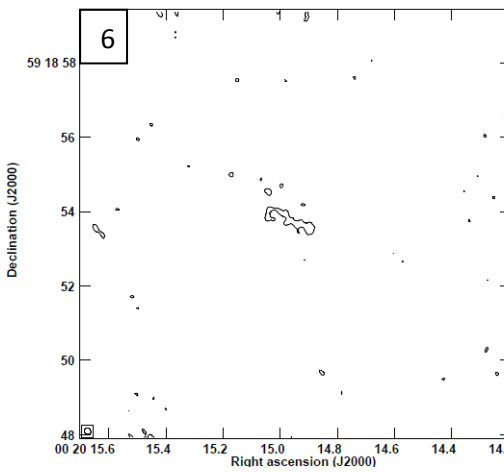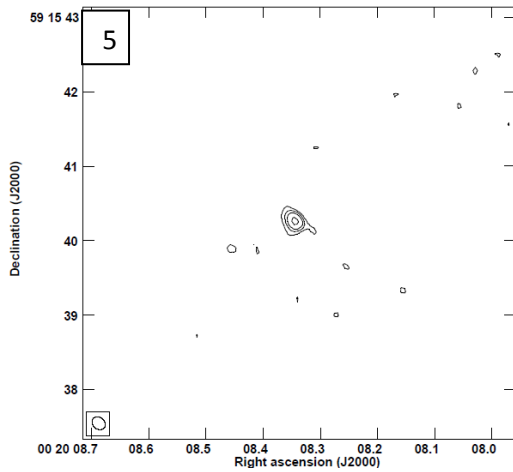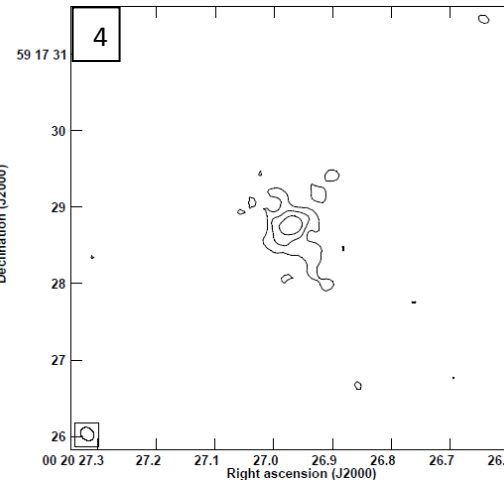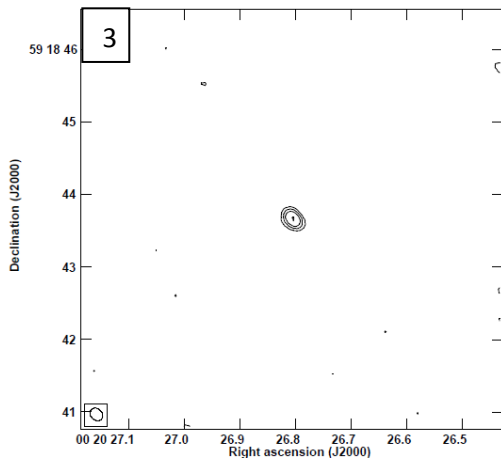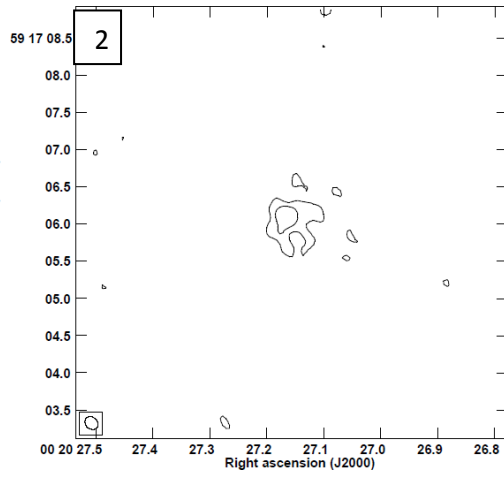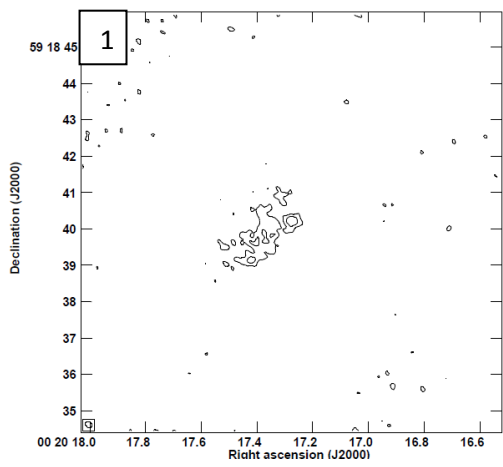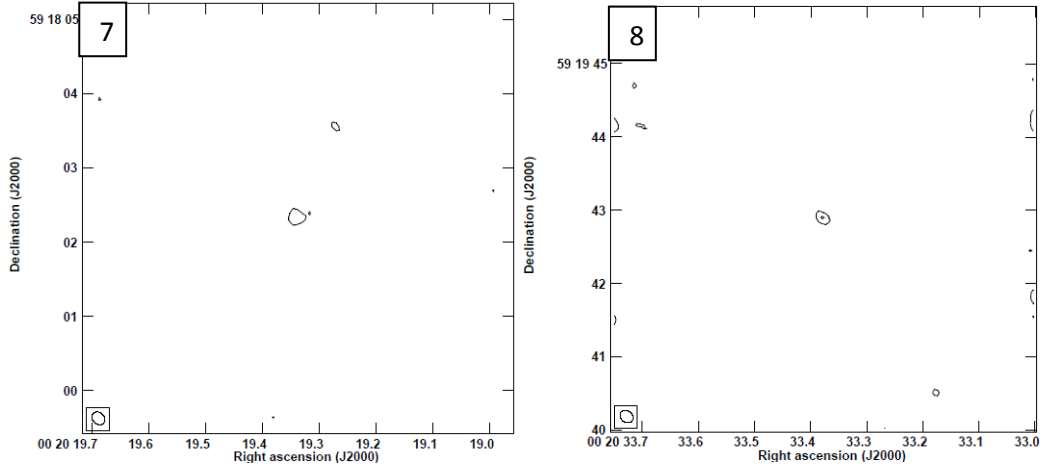
Figure 4.4: Contour maps of the various sources found within IC10. Each of the images has a resolution of 0.19" x 0.16" and a noise level of 35μJybeam^{-1}. The scale of the clean beam is represented in the bottom left corner of each image. The contour levels are at 3, 6, 10, 20, 40, 80, 150, 300 and 600 times the noise level. The number in the top left of each diagram is the identifying source number used in **Table 4.2** and the rest of the thesis.

Source	Major Axis (arcseconds)	Minor Axis (arcseconds)	Major Axis (pc)	Minor Axis (pc)	Position Angle (Degrees)
1	3.60	2.02	12.22	6.86	137
2	1.41	0.92	4.79	3.12	59
4	1.81	1.12	6.14	3.80	6
6	2.28	1.03	7.74	3.50	58

Table 4.3: Table presenting the dimensions of the resolved sources within IC10. The source dimensions were estimated by fitting an ellipse to the data with a major and minor axis being detailed as well as the position angle. IC10 is assumed to be at a distance of 0.7 Mpc (**Hunter et al. 2012**).

4.5: Primary Beam Attenuation Correction

The maps that have been created have not been corrected for primary beam attenuation and the measured flux densities need to be corrected. To correct for the primary beam, the distance each source is from the pointing centre is measured and then used with a model Gaussian of FWHM 30 arcmins (see section **3.5.4**). The corrected flux densities are given in **Table 4.4**.

Source	RA (J2000)	DEC (J2000)	Distance from pointing centre (arcmins)	Correction Factor	Corrected Peak Flux Density(mJy)	Corrected Integrated Flux Density (mJy)
1	00 20 17.268	+59 18 40.210	0.437	1.000306	0.326 ± 0.043	15.5 ± 0.831
2	00 20 27.153	+59 17 06.019	2.712	1.011860	0.379 ± 0.041	4.59 ± 0.498
3	00 20 26.805	+59 18 43.662	2.427	1.009487	0.984 ± 0.075	0.984 ± 0.075
4	00 20 26.970	+59 17 28.722	2.517	1.010207	0.572 ± 0.043	5.43 ± 0.658
5	00 20 08.345	+59 15 40.262	3.407	1.018781	1.11 ± 0.065	1.11 ± 0.065
6	00 20 14.937	+59 18 53.663	0.887	1.001262	0.185 ± 0.040	8.07 ± 0.453
7	00 20 19.332	+59 18 02.371	0.544	1.000474	0.692 ± 0.190	0.692 ± 0.190
8	00 20 33.379	+59 19 42.896	4.285	1.029870	0.240 ± 0.064	0.240 ± 0.064

Table 4.4: *Table showing the corrected flux for the various sources within IC10. The distance from the pointing centre is also detailed as well as the derived correction factor. The size of the sources will not change due to the primary beam.*

5: Discussion

5.1: Introduction

In this section, the results found in section **4** will be analysed and compared to values found in the literature. The nature of each detected source will be evaluated along with some applications of the data such as calculating the star formation rate and interpreting the e-MERLIN data on the non-thermal superbubble (**Yang & Skillman 1993**). Analysis is carried out in a similar format to that described in **Fenech et al (2008)**, **Beswick et al. (2006)**, and **Fenech et al (2010)**.

5.2: Source Nature

One of first steps in the analysis of the data is to determine the nature of each of the observed sources. This information can then be used to analyse IC10 including estimating star formation rates and plotting SNR on a $\Sigma - D$ diagram. There are several different pieces of information that can be used such as the spectral index and maps at other wavelengths in the literature. This evidence will be presented here and discussed to find the nature of each source.

<u>Spectral Index</u>

The spectral index is a useful diagnostic for the nature of radio sources. As discussed in section **2**, each radiation mechanism has a characteristic spectral index of the form $S \propto \nu^{\alpha}$. The radiation mechanisms are closely related to the types of sources and so, the spectral index can be used to determine the type of source observed through the emission mechanism. A steep negative spectral index indicates synchrotron emission (closely associated with SNR) , a flat spectral index indicates Bremsstrahlung (closely associated with HII regions) and a positive spectral index at wavelengths shorter than a few mm indicates black body (or grey body) emission (closely associated with dust).

Source	RA (J2000)	DEC (J2000)	Estimated Spectral Index
1	00 20 17.268	+59 18 40.210	(0) - (-0.2)
2	00 20 27.153	+59 17 06.019	(0) - (-0.2)
3	00 20 26.805	+59 18 43.662	(-1) - (-1.2)
4	00 20 26.970	+59 17 28.722	(-0.4) - (-0.6)
5	00 20 08.345	+59 15 40.262	(-1) - (-1.2)
6	00 20 14.937	+59 18 53.663	(-0.6) - (-0.8)
7	00 20 19.332	+59 18 02.371	(0) - (-0.2)
8	00 20 33.379	+59 19 42.896	(-0.8) - (-1.0)

Table 5.1: *Table showing the position and estimated spectral index of the sources found within IC10. The spectral indices are estimated through the use of **Figure 5.1**.*

In order to determine the spectral index of a source, information is required at two different wavelengths. In this observation however, information is only available at 20cm wavelength. In the absence of other wavelengths, the spectral indices of the

sources environment will be estimated using the spectral index map from **Heesen et al. (2011)** which is shown in **Figure 5.1**.The extracted spectral index information is given in **Table 5.1**.
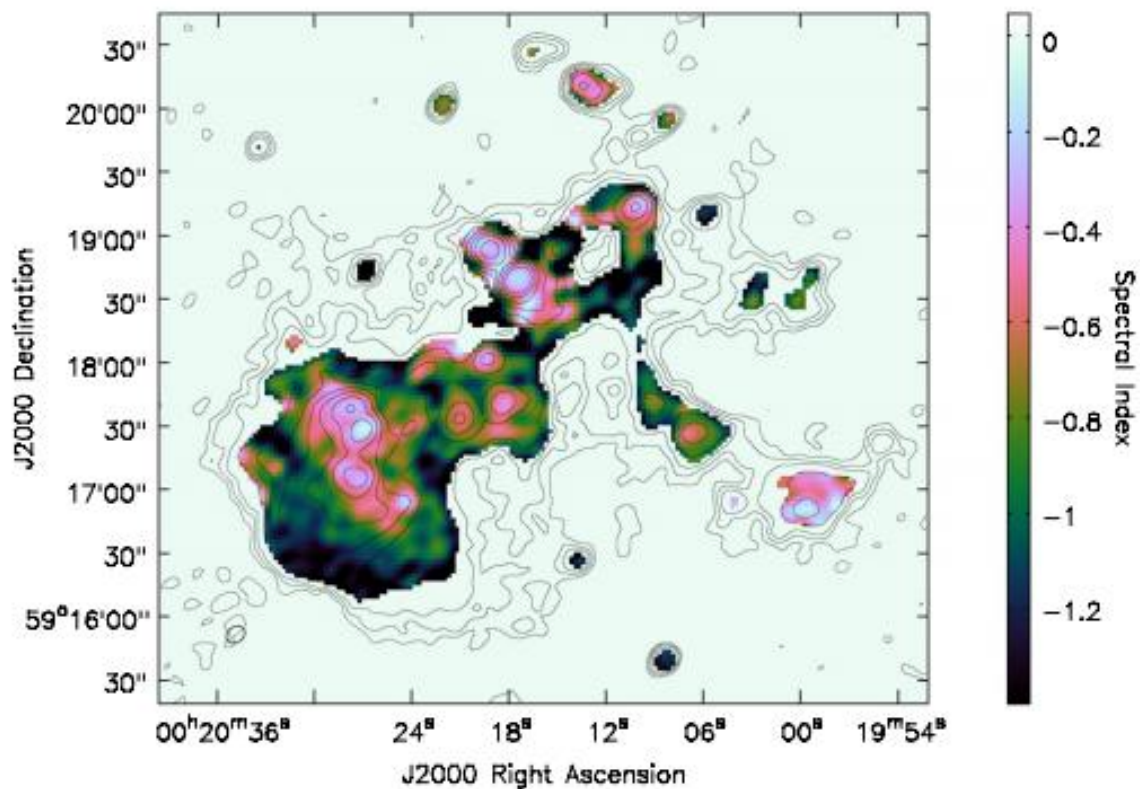
*Figure 5.1: Radio spectral index map taken from **Heesen et al. (2011)**. The map is colour coded at 9.4"x 7.3" resolution. The contours show the radio continuum emission at 6cm wavelength.*

HI Maps

HI maps show where the neutral hydrogen resides within a source. They can be used to show where there are over densities of hydrogen which are closely related to regions of current star formation. The maps can also be used to determine the rotation speeds of galaxies. The positions of the sources will be compared with the HI map taken by **Hunter et al. (2012)** and is shown in **Figure 5.2**.

Comparisons with the HI maps show that all of the detected sources follow the filamentary structure of the hydrogen within IC10. There are several 'holes' within the map which are thought to be created by multiple SNe following periods of massive star formation. The bright patch at the centre of the map appears to be where gas is accumalating or has recently done so and is a region of intense star formation. This position also corresponds to the location of the non-thermal super bubble discussed in **Yang & Skillman (1993)**.

66

The positions of sources 1, 2 and 4 correspond to regions of high hydrogen density. Source 1 is located on one of the filaments between two 'holes' in the HI emission and could be a star forming region that is due to the hydrogen being locally compressed. Sources 2 and 4 are both located at the same position as the bright region of active star formation.
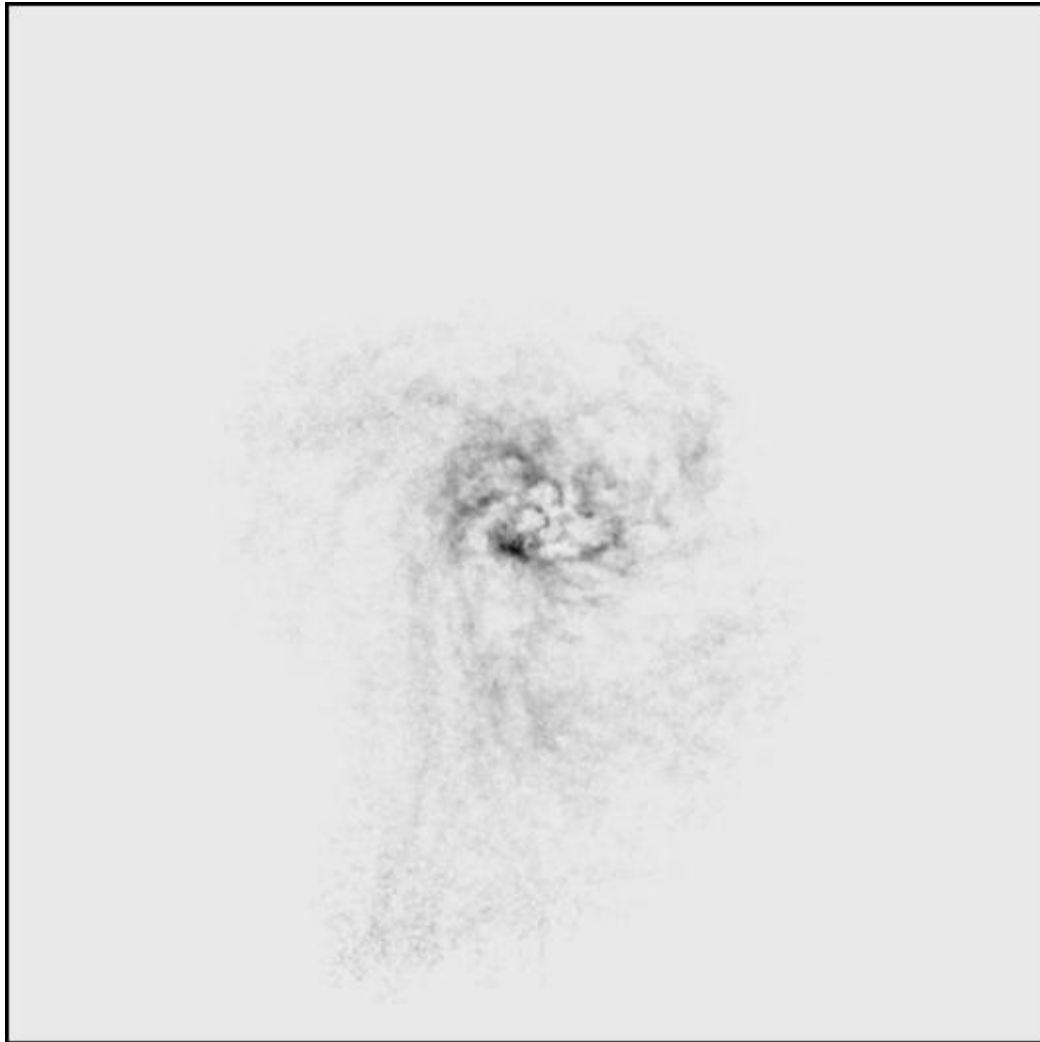
*Figure 5.2: Inverted HI map of IC10 taken by **Hunter et al. (2012)**.*

<u>Hα Maps</u>

Hα maps highlight the locations of excited hydrogen, which is closely associated with regions of active star formation (e.g. **Kennicutt 1998)**. The positions of the sources will be compared to Hα maps produced by **Hunter & Elmegreen (2004)** which are given in **Figure 1.1**.

The positions of sources 1, 2, and 4 again correspond to regions of strong Hα emission. This further strengthens the evidence that these sources are associated with regions of active star formation.

Brightness Temperature

Another parameter that can be investigated is the brightness temperature of the source. The brightness temperature can be estimated through the use of the Rayleigh-Jeans approximation (see section **2.4**). The equation for brightness temperature is given by:

$$T_b = \frac{c^2}{2k\nu^2} I_\nu$$

Where c is the speed of light, k is Boltzmann's constant, ν is the central frequency of the observation and I_ν is the intensity of a source. The intensity of a radio source can easily be found dividing the flux by the solid angle of the source. Sources that are dominated by thermal processes will have a brightness temperature equal to the physical temperature of the gas whereas non-thermal sources will have a high brightness temperature that is not linked to a physical temperature. Estimated brightness temperatures are given in **Table 5.2** and brightness temperature maps of the resolved sources are shown in **Figure 5.3**.

Source	Peak Brightness Temperature (K)
1	3,600
2	4,100
3	>17,100
4	6,000
5	>19,100
6	2,200
7	>12,100
8	>4,000

Table 5.2: *Table displaying the estimated brightness temperature per beam for each of the detected sources.*

The brightness temperature of the unresolved sources is likely an underestimate as the source may be many times smaller than the convolving beam. In order to gain accurate brightness temperatures, unresolved sources need to be resolved which can be attained through the use of very long baseline interferometry (VLBI).

Morphology & Classification

The final step in determining the nature of each source is to consider the morphology. Contour maps of each source can be found in **Figure 5.4**. Each source will be analysed individually and the classifications are summarized in **Table 5.3**.

Source 1

Source 1 is the largest radio source found and falls towards the centre of IC10. The source is resolved, with a roughly elliptical shape, and is dominated by extended emission. The source has a flat spectral index and is associated with emission at both HI and Hα wavelengths. The brightness temperature maps reveal that the source 1 has a brightness temperature of the order of 3000K and has an unusual morphology with a peak in the north-east corner of the source. This is strong evidence that source 1 is a compact HII region linked to ongoing star formation.
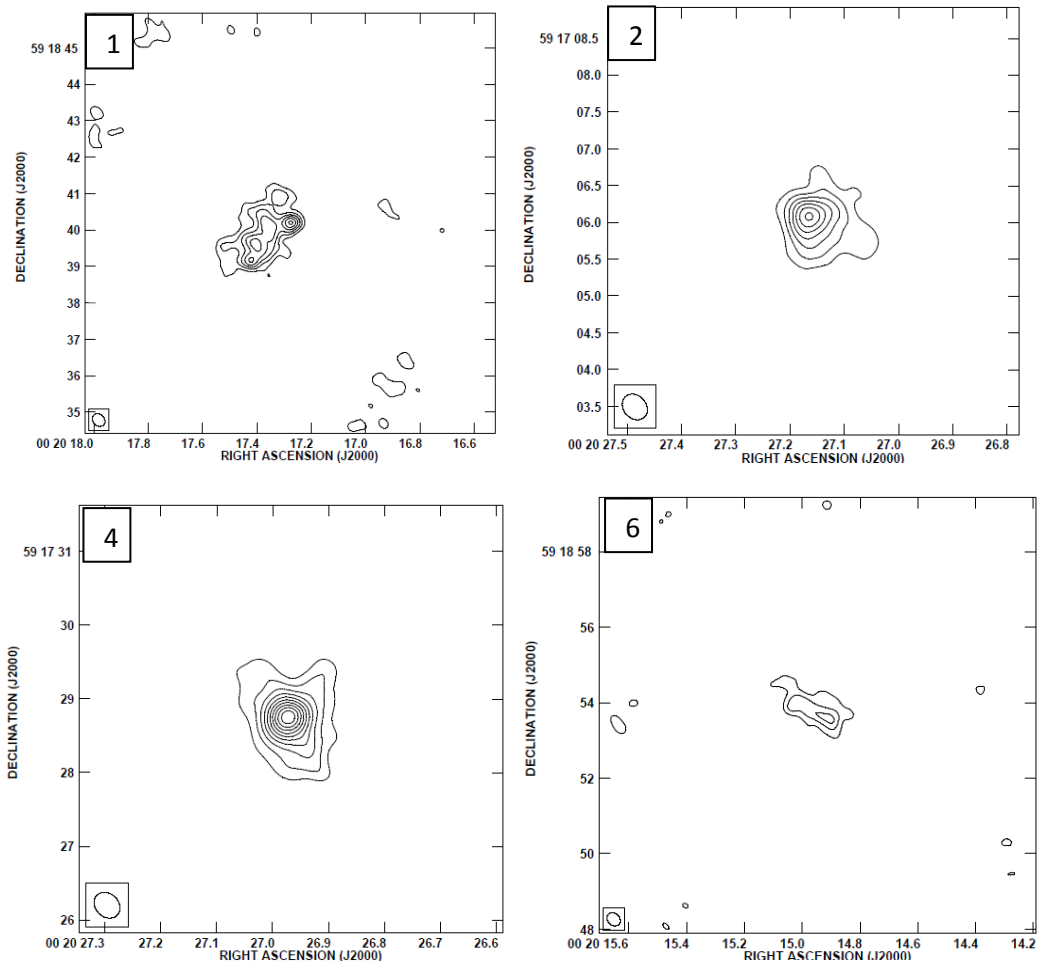
Figure 5.3: *Brightness temperature maps of the 4 resolved sources located within IC10. Each source is numbered in the same way as in section 5. The beam size is 0.38594 x 0.31306 and the contours are set at 1000, 1500, 2000, 2500, 3000, 3500, 4000, 4500, 5000, 5500 and 6000K.*

Source 2

Source 2 is a resolved source found towards the south-west of IC10. The source is roughly circular and is much smaller than source 1. Source 2 has a flat spectral index and is also associated with emission at both HI and Hα wavelengths. This source is located just north of the non-thermal super bubble described in **Yang & Skillman (1993)** and is located within the bright HI concentration. The brightness temperature map of source 2 show that it has a brightness temperature of the

order 4000K, concentrated on the centre of the source. The above evidence suggests that source 2 is an HII region.

<u>Source 3</u>

Source 3 is a bright unresolved source and is found in the north-west of IC10. The source has a steep negative spectral index and does not appear to be associated with any strong emission in Hα. The brightness temperature of source 3 reveals it has a brightness temperature of >17000K. As the source is unresolved, this could be a major underestimate of the true brightness temperature. This is good evidence that source 3 is an evolved SNR.

<u>Source 4</u>

Source 4 is another resolved source that is located towards the south-west of IC10, close to source 2 and the super bubble described by **Yang & Skillman (1993)**. This source has a slightly negative spectral index and is associated with Hα emission. HI maps show that this source is located within the bright concentration where also source 2 is found. Comparison with the literature shows that there is a large number of Wolf-Rayet stars located just south of this source. The brightness temperature map shows that source 4 has a temperature of order 5000K. This evidence suggests that source 4 is an HII region and the location of ongoing star formation within IC10

<u>Source 5</u>

Source 5 is a bright source that is located towards the south-east of IC10. This source is unresolved with a steep negative spectral index. This source is not associated with any significant Hα emission. The brightness temperature of source 5 is larger than 19000K, and could be much higher as the source is unresolved. This evidence suggests that source 5 is a SNR.

<u>Source 6</u>

Source 6 is a resolved source located towards the centre of IC10, close to source 1. Source 6 has an unusual morphology, appearing to be elongated in the east-west direction. The source is not associated with any significant Hα emission and appears to be at a connecting point between filaments on the HI map. Source 6 has a negative spectral index according to the spectral index maps. The brightness temperature maps show that the brightness temperature of source 6 is quite low, roughly 2000K. Due to the unusual morphology and low brightness temperature, this source will be classified as an HII region.

Source 7

Source 7 is a dim unresolved source located just south of the centre of IC10. Spectral index maps show that the environment the source is located in has a flat spectral index and Hα maps show that there is faint Hα emission at its position. The brightness temperature of source 7 reveals that this source has a temperature of at least 12000K but as the source is unresolved, it could be much larger. Due to the unresolved nature of source 7, it will be classified as a SNR which has exploded within a HII region.

Source 8

Source 8 is a dim source located towards the north-west of IC10. The source is compact and unresolved and comparison with the spectral index maps reveals that the source has a steep negative spectral index. This source is not associated with any Hα emission and the brightness temperature reveals a temperature of >4000K. As the source is unresolved, the brightness temperature could be much higher. As this source is unresolved and has a steep negative gradient it will be classified as a SNR.

Source	Classification
1	HII Region
2	HII Region
3	SNR
4	HII Region
5	SNR
6	HII Region
7	SNR
8	SNR

Table 5.3: Summary of the classifications of the various sources within IC10.

Now that the sources have been classified, further analysis can be carried out on the different types of sources such as plotting the SNR on a $\Sigma - D$ diagram or estimating star formation rates.

5.3: Star Formation and Supernova Rates

It is possible to estimate the star formation rate (SFR) and supernova rate for a given galaxy from radio luminosity due to the tight correlation between radio continuum and far infrared (FIR) emission (**Condon 1992**). The most widely held explanation for the correlation suggest that massive stars dominate FIR emission and that the supernova rate determines the radio luminosity as the main contribution to the radio luminosity is non-thermal synchrotron emission accelerated in the shock wave from SNR (see section **2.7**). A major problem that has been discovered is that if the radio luminosity of the entire galaxy is simply divided by the luminosity of a typical SNR, the resulting supernova rate is far too large (**Gehrz et al. 1983**). This problem can be resolved by taking into account the

shock mechanisms to accelerate the cosmic ray electrons and that cosmic ray electrons can continue to accelerate long after the SNR becomes undetectable.

Assuming a Salpeter initial mass function, integrating over all stars from 0.1 $M_\odot$ to 100 $M_\odot$, a conversion factor can be determined to represent the SFR of a galaxy. Adapted from **Yun, Reddy & Condon (2001)**, this is given by:

$$SFR(M_\odot yr^{-1}) = 5.6 \pm 1.7 \times 10^{-22} L_{1.5GHz}(WHz^{-1})$$

Similarly the supernova rate, ν_{SN}, of a galaxy can be determined from the SFR using:

$$\left(\frac{\nu_{SN}}{yr^{-1}}\right) \sim 0.041 \left[\frac{SFR(M \geq 5M_\odot)}{M_\odot yr^{-1}}\right]$$

This equation only depends on star formation from stars that are larger than 5 $M_\odot$ because only these massive stars are capable of generating supernova explosions. The SFR of these massive stars can be estimated through:

$$\left[\frac{SFR(M \geq 5M_\odot)}{M_\odot yr^{-1}}\right] = \left(\frac{L_{1.5GHz}}{3.79 \times 10^{21}WHz^{-1}}\right)$$

These last two equations were adapted from **Condon (1992)**.

Now that equations for star formation and supernova rates have been found, they can be applied to the sources found within IC10.

The total flux recovered from the observed sources within the e-MERLIN observations is equal to 36.62 $\pm$ 3.88 mJy. Using the above equations, this corresponds to a SFR of 0.0014 $\pm$ 0.00037 $M_\odot yr^{-1}$ and a supernova rate of $\nu_{SN} \sim 0.000022 yr^{-1}$.

This star formation rate is likely to be an underestimate of the true star formation rate within IC10 due to a several effects, including the nature of the interferometry observation and the low density nature of dwarf galaxies themselves.

Similarly to how the largest baselines determine the smallest resolution of an image, the shortest baselines determine the largest detectable scales. Due to the additive properties in the Fourier domain, an absence of a measurement on the (u,v) plane has the effect on the maps as if a map is subtracted made with another telescope which measures precisely these gaps. For example, a telescope consisting of only long baselines will not measure the (u,v) plane close to the origin, resulting in complete insensitivity to any extended emission from the source. Likewise a telescope that only measures short baselines will not measure the (u,v) plane far from the origin, resulting in a lack of sensitivity to small scale structure. The only way to recover all flux from a source is to use single dish measurements, i.e.

measure emission at the origin of the (u,v) plane. A good measure of the largest resolvable angular scale is given by the relationship:

$$\theta_{Max} \approx \frac{0.6\lambda}{b_{min}}$$

Where λ is the wavelength of the observation and b_{min} is the shortest baseline within an array.

For the observations detailed, the shortest baselines (around 11 km) result in a maximum angular scale of roughly 2 arcsec. The central region of IC10 is roughly 11 arcmin across and so most of the extended emission associated with IC10 is resolved out.

Due to the low mass of dwarf galaxies, they do not possess a strong gravitational potential. Therefore as massive stars explode as supernova within dwarf galaxies, the expanding shock fronts can sweep up interstellar gas and potentially push it out of the galaxy entirely. Magnetic fields will also be swept up in this process as well as their coupled cosmic ray electrons, allowing them to escape the dwarf galaxy before they have radiated all of their available energy. This reduces the non-thermal luminosity of the galaxy and leads to the measured star formation rate at radio wavelengths to be an underestimate of the true star formation rate. This effect will affect all studies into the star formation rate of IC10 and other dwarf galaxies at radio wavelengths.

Observations using the J-VLA by **Heesen et al. (2015)** reveal much more extended emission within IC10. The observations were taken in D-array at L-Band with a shortest baseline of roughly 40m. This corresponds to a maximum angular scale of roughly 10 arcmins. These observations resolve nearly all of the extended emission within the central region of IC10. The maps reveal a total flux density of 200mJy, corresponding to a SFR of $0.0062 \pm 0.0002 \ M_\odot yr^{-1}$ and a supernova rate of $\nu_{SN} \sim 0.00027 yr^{-1}$.

Additionally, single dish observations by **White& Becker (1992)** using the Green Bank Telescope reveal a total flux density of 319mJy at 1.4GHz, corresponding to a SFR of $0.0099 \pm 0.0027 \ M_\odot yr^{-1}$ and a supernova rate of $\nu_{SN} \sim 0.00043 \ yr^{-1}$.

The SFR determined by the e-MERLIN observations is roughly a factor of 10 times lower than that found by **White & Becker (1992)**. **Hunter & Elmegreen (2004)** measure the SFR to be $0.049 \ M_\odot yr^{-1}$ through the use of Hα emission, significantly larger than that found in the radio studies.

Another source of information for finding the star formation rate of IC10 is to count the number of SNR that have been detected within this study. If we assume that a

SNR is detectable for roughly 10^4yrs, and note that 4 SNR have been detected, the supernova rate is determined to be $v_{SN} \sim 0.0004 \ yr^{-1}$. We can put this value back into the above equations to determine a star formation rate. This rate comes out at $\approx 0.02 \ M_\odot yr^{-1}$ which is compatible with that found by both **Heesen et al. (2015)** and **White & Becker (1992)** and is much closer to the value derived from Hα observations.

These results indicate that the measured SFR by e-MERLIN is indeed an underestimate of the SFR of IC10. All of these results show that IC10 has a relatively low current SFR and indicate that it is in a post-starburst phase. This suggestion is backed up by the appearance of an abundance of holes in the HI maps (**Figure 5.2**) which are created in violent bursts of star formation associated with galaxies that have undergone a starburst.

5.4: Σ-D Relationship

A further form of analysis that can be applied to the detected SNR is to plot them on a surface brightness (Σ) to diameter (D) diagram. However, the SNR found within this study are unresolved and therefore it is not possible to measure the diameter or surface brightness of these SNR. All we can do is place limits on where the source will appear on the Σ-D diagram. If the sources where resolved, we would follow the analysis as follows.

The mean surface brightness at a specific radio frequency, Σ_v, is distance independent and is an intrinsic property of the SNR (**Shklovskii 1960**). The relationship has the form:

$$\Sigma_v = AD^\beta$$

Where D is the diameter of the SNR and A and β are constants.

It is possible to use this relationship to obtain distance estimates to nearby galaxies (**Clark & Caswell 1976**), however there are several significant problems (**Green 1984**). The main problem with using the Σ-D relationship is that there is a large degree of uncertainty in the independent distance measurements in the Milky Way to each SNR. Associations of SNR with other objects used for distance estimation such as HI regions and molecular clouds cannot always be made with great confidence. Another problem that arises is that there may be a range of intrinsic brightness for SNR at the same distance. This is due to the variety of environments that SNe occur in and the differences in the progenitor stars (**Allakhverdiev et al. 1983**). There may be several linear diameters which return the same surface brightness increasing uncertainty in the measurements. However, observationally complete SNR samples reveal that the surface brightness decreases with increased diameter.

The Σ-D relationship at 1 GHz (excluding Cas A) is given in **Case & Bhattacharya (1998)** as:

$$\Sigma_{1GHz} = 2.07^{+3.10}_{-1.24} \times 10^{-17} D^{(-2.38\pm0.26)} W m^{-2} Hz^{-1} sr^{-1}$$

The spectral index of each SNR can be used to scale the observed surface brightness to 1 GHz. Then the SNR can be plotted on a Σ-D diagram and be used to estimate information about the galaxy such as the distance.

In order to resolve the SNR, observations can be undertaken at a shorter wavelength using the e-MERLIN array. Observations at λ=6cm for instance would improve the resolution by a factor of roughly 3. Another solution is to use VLBI (Very Long Baseline Interferometry) to improve the resolution.
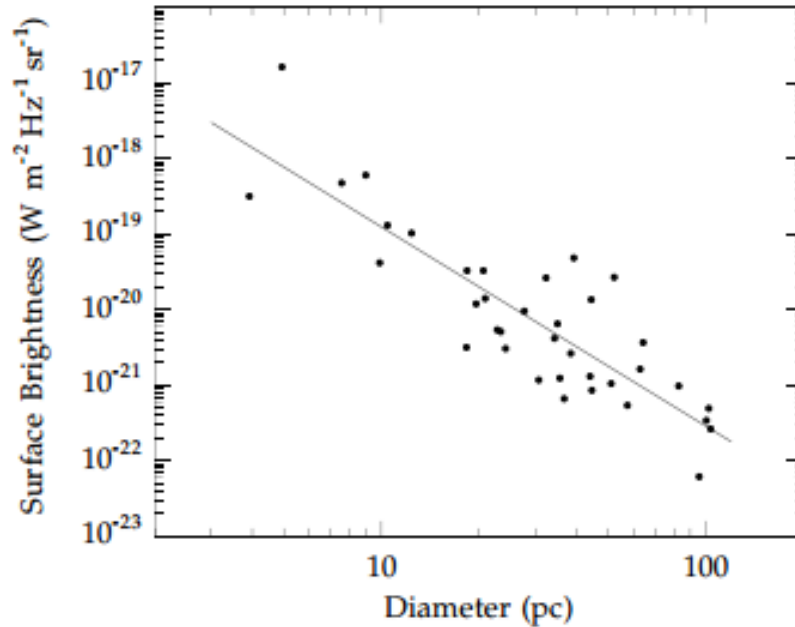
Figure 5.4: *Σ-D relationship taken from* ***Case & Bhattacharya (1998)***. *This diagram was constructed using SNR with known distances (including Cas A).*

5.5: Non-Thermal Superbubble

One of the major interesting features of IC10 is the non-thermal superbubble (NTSB). There have been many suggestions for the origin of the NTSB with explanations including that it is the result of many supernova remnants (**Yang & Skillman 1993**) or that it is the result of a hypernova remnant (**Lozinskaya & Moiseev 2007**).

Heesen et al. (2015) suggests that as massive stars are the major cause of stellar feedback, carving hot bubbles into the ISM, and these stars normally form in groups, these bubbles start to overlap and merge into a much larger structure. The wind from massive Wolf-Rayet stars power early expansion of the bubble and the

following supernovae shock the interior resulting in thermal X-Ray and synchrotron emission. Further discussions of superbubbles can be found in **Krause et al. (2014)**.

The non-thermal superbubble found within IC10 contains a large number of Wolf-Rayet stars (**Massey & Holmes 2002**), reinforcing the suggested cause of the superbubble. We would expect that with the large number of Wolf-Rayet stars there would be the presence of several supernova remnants within the NTSB. However, the high resolution maps produced from these observations show no compact sources associated with this region. This can be explained by considering how a SNR can be seen. SNRs can be detected through the observation of the expanding shock wave, which results from the interaction of the supernova with the surrounding interstellar medium. In the case of IC10, the star formation and subsequent SNe could by now have rarefied the interstellar medium. A SNR in this rarefied medium would not be detected as the shockwave has nothing to interact with and will quickly travel through this medium to the edge of the superbubble where it will catch up with shockwaves from other SNR. This superimposed shockwave is detectable at lower resolutions (see **Heesen et al. (2015)** but because of e-MERLIN's large baselines, it is resolved out.

A further point of interest is that there appears to be the origins of an HI hole within the superbubble. This hole is analogous to the other HI holes found within IC10 and is a result of the SNe resulting from intense star formation.

5.6: Summary

The analysis of the data shows that the collected data is consistent with data found in the literature. However, more information is required to further probe IC10 at high resolutions, such as additional observation data at a different radio wavelength to determine accurate spectral indices. Additionally , VLBI could be used to perform a resolved study of observed SNR.

6: Conclusion and Future Plans

This project reports on high spatial resolution (0.66 pc x 0.53 pc) observations at a radio continuum wavelength of λ=20cm (ν = 1.5GHz) of the nearby dwarf irregular galaxy IC10. The aim of the project was to study extragalactic star formation in dwarf galaxies through observations of HII regions and SNR. The processes which trigger star formation on these small scales are not currently well understood in the context of dwarf galaxies. IC10 is regarded in the literature to be in a starburst phase, making it an ideal place to study these processes.

After reviewing the different radiation mechanisms that contribute to the 20cm band, such as free-free and synchrotron radiation, we presented the data calibration and reduction process, concentrating on those processes related to e-MERLIN observations that would affect the final maps. These final maps were analysed to determine the nature of each source as well as gain an insight into IC10 as a whole.

We detected 8 sources within our final maps which were classified using the spectral index, morphology and brightness temperature of each source. The 4 extended sources were classified as HII regions and the 4 unresolved sources were classified as SNR. Three of the four detected HII regions coincide with known regions of active star formation whereas the detected SNR appear to be distributed more randomly. Further analysis of each individual SNR is limited by the resolution of the study, which could be remedied through the use of higher frequency e-MERLIN at λ=6cm or additional VLBI observations.

We used our results to estimate star formation and supernova rates base on the e-MERLIN data only. We did this by summing the detected flux from the observed source and then, using the Condon relationships to estimate a SFR and SNe rate. Because e-MERLIN observations lack short baselines, this grossly underestimates the star formation and supernova rates. However, estimating the supernova rate from counting the SNR and some reasonable assumption as to the length of time they typically would be detectable yields a similar value that is consistent with the literature.

We studied in detail the non-thermal superbubble. This region is associated with the bulk of current star formation activity in IC10. The literature reveals the presence of many Wolf-Rayet stars within this region, however neither the superbubble nor any SNR are detected with e-MERLIN. Although no SNR are detected within this region, its origin is attributed to one or multiple supernovae. The intense star formation associated with this region has blown away the interstellar medium, leaving the stars in a rarefied medium. When we observe a SNR, we are actually seeing the interacting shock front with the ISM. If the ISM is

rarefied, we do not expect to see this interaction. Another factor is that e-MERLIN is insensitive to large scale structure, meaning the superbubble could simply be resolved out.

In order to further understand the nature of the observed sources, additional observations at different wavelengths are required. Additional observations of IC10 at λ=6cm using e-MERLIN would improve the resolution of the final maps roughly by a factor of 3 potentially resolving some of the unresolved sources allowing the morphology of the unresolved sources to be studied. Although the morphology can be used to classify each source, ideally the spectral index would be used on unresolved or slightly resolved sources. The sources that are more extended would require JVLA A-array observations (ideally with the Pie Town VLA antenna included) taken at 20cm and 6cm. Such observations would fill the gap in the uv-plane between our e-MERLIN data and the lower resolution JVLA data on IC10 published by **Heesen et al. (2015)**.

The shorter baselines will provide sensitivity to the more extended emission within IC10 and, with the longer baselines added in, will provide us with a map containing all spatial frequencies, out to the longest baselines observed. We will use this to investigate the relation between the unresolved sources as seen in the e-MERLIN maps with the larger scale ISM distribution. Additional VLBI observations could also be sought to further probe the morphology of those sources that remain unresolved for e-MERLIN.

In the medium term, this work will be continued into investigating a much wider range of dwarf and spiral galaxies within the LeMMINGs (Legacy e-MERLIN Multi-Band Imaging of a complete Nearby Galaxies Survey) sample. LeMMINGs has many aims including the calibration of star formation levels within galaxies. There is a long standing issue with how to calibrate either global radio or IR emission as a measure of star formation and how this calibration varies with galaxy type and environment. This can be achieved by identifying star formation products within major galaxies (i.e. HII regions, super star clusters, planetary nebulae, supernovae and supernova remnants) and use them to directly infer star formation rates. These sources can also be used to trace early stages of stellar evolution and place constraints on the levels of star formation at different stages in the evolution of individual galaxies.

References

Allakhverdiev, A. O., Guseinov, O. Kh., Kasumov, F. K., Iusifov, I. M. 1983, Ap&SS, 97, 287

Barbon, R., Ciatti, F., Rosino, L. 1979, A&A, 72, 287

Bell, A. R. 2004, MNRAS, 353, 550

Bell, E. F. 2003, ApJ, 586, 794

Beswick R. et al. 2006, MNRAS, 369, 1221

Borissova, J. Georgiev, L. Rosado, M., Kurtev, R., Bullejos, A., Valdez-Gutiérrez, M. 2000, A&A, 363, 130

Bottinelli, L., Gouguenheim, L., Heidmann, J. 1972, A&A, 18, 121

Bracewell, R. N. 2000, *The Fourier Transform and its Application*, 3rd Edition, Singapore: McGraw-Hill Higher Education

Branch, D., Nomoto, K. 1986, AA&A, 164, L13

Brant, W. N., Ward, M. J., Fabian, A. C., Hodge, P. W. 1997, MNRAS, 291, 709

Brinks, E. 1990, in *The Cool Phase of the Interstellar Medium: Cool Gas*, eds. H. A. Thronson Jr. & J. M. Shull

Brinks, E., Bajaja, E. 1986, A&A, 169, 14

Case, G. L., Bhattacharya, D. 1998, ApJ, 504, 761

Chevalier, R. A. 1982, ApJ, 259, 302

Chevalier, R. A. 1998, ApJ, 499, 810

Clark, B. G. 1973, VLA Scientific Report, 107, 1

Clark, B. G. 1980, A&A, 89, 377

Clark, D. H., Caswell, J. L. 1976, MNRAS, 174, 267

Cole, S., Aragon-Salamanca, A., Frenk, C. S., Navarro, J. F., Zepf, S. E. 1994, MNRAS, 271, 781

Condon, J. J. 1992, ANRAA, 30, 575

Condon, J. J., Cotton, W. D., Greisen, E. W., Yin, Q. F., Perley, R. A., Taylor, G. B., Broderick, J.J. 1998, AJ, 115, 1693

Condon, J. J., Ransom, S. M. 2007, *Essential Radio Astronomy*, (Online), Avaliable: http://www.cv.nrao.edu/course/astr534/ERA.shtml (20/08/14)

Dawber, M. 2013, *Classical Physics II*, (Online), Avaliable: http://www.ic.sunysb.edu/Class/phy141md/doku.php?id=phy142:lectures:16, (20/08/14)

de Vaucouleurs, G., Ables, H. 1965, PASP, 77, 457

de Vaucouleurs, G., Freeman, K. C. 1972, Vistas Astrom, 14, 163

Dean, J. F., Davies, R. D. 1974, MNRAS, 170, 503

Deharveng, L., Schuller, F., Anderson, L. D., Zavagno, A., Wyrowski, F., Menten, K. M., Bronfman, L., Testi, L. et al. 2010, A&A, 523, 6D

Elmegreen, B. G. 2012, in IAU Symp. 284, ed. R. J. Tuffs, & C. C. Popescu (Cambridge: Cambridge Univ. Press), 317

Epstein, E. E. 1964, AJ, 69, 490

Fenech, D. M., Muxlow, T. W. B., Beswick, R. J., Pedlar, A., Argo, M. K. 2008, MNRAS, 391, 1384

Fenech, D., Beswick, R., Muxlow, T. W. B., Pedlar, A., Argo, M. K. 2010, MNRAS, 408, 607

Flynn, C. 2005, *Astrophysics II*, (Online), Avaliable: http://www.astro.utu.fi/~cflynn/astroII/l4.html. (20/08/14)

Gehrz, R. D., Sramek, R. A., Weedman, D. W. 1983, ApJ. 267, 551

Gil de Paz, A., Madore, B. F. 2005, ApJS, 156, 345

Gouguenheim, L. 1969, A&A, 3, 281

Green, D. A. 1984, MNRAS, 209, 449

Hecht, E. 2002, *Optics*, 4th Edition, San Francisco: Pearson Education

Heesen, V. et al. 2015, MNRAS, 447, L1

Heesen, V., Rau, U., Rupen, M. P., Brinks, E., Hunter, D. A. 2011, ApJL, 739, L23

Hodge, P., Lee, M. G. 1990, PASP, 102, 26

Högbom, J. A. 1974, A&AS, 15, 417

Hubble, E. P. 1936, *The Realm of the Nebulae*, New Haven: Yale University Press

Huchra, J. P., Vogeley, M. S., Geller, M. J. 1999, ApJS, 121, 287

Huchtmeier, W. K. 1979, A&A, 75, 170

Hunter, D. A., Elmegreen, B. G. 2004, AJ, 128, 2170

Hunter, D. et al. 2012, AJ, 144, 134

Jarrett, T. H., Chester, T., Cutri, R., Schneider, S. E., Huchra, J. P. 2003, AJ, 125, 525

Jeans J. H. 1902, Royal Society of London Philosophical Transactions Series A, 199, 1

Jewett, J. W., Serway, R. A. 2008*, Physics for Scientists and Engineers with Modern Physics*, 7th Edition, Brooks/Cole CENTAGE Learning

Karachentsev, I. D., Tikhonov, N. A. 1993, A&AS, 100, 227

Kennicutt, R. C. 1998, ApJ, 498, 541

Kim, M. et al. 2009, ApJ, 703, 816

Klein, U., Gräve, R., Wielebinski, R. 1983, A&A, 117, 332

Krause, M., Diehl, R., Böhringer, H., Freyberg, M., Lubos, D. 2014, A&A, 566, A94

Lagos, C. D. P., Padilla, N. D., & Cora, S. A. 2009, MNRAS, 397, L31

Lin, C. C., & Shu, F. H. 1964, AJ, 140, 646

Lozinskaya, T. A., Egorov, O. V., Moiseev, A. V., Bizyaev, D. V. 2009, AstL, 35, 730

Lozinskaya, T. A., Moiseev, A. V. 2007, MNRAS, 381, L26

Marzke, R. O., & da Costa, L. N. 1997, AJ, 113, 185

Massey, P. Armandroff, T. E. 1995, AJ, 109, 2470

Massey, P., Armandroff, T. E., Conti, P. S. 1992, AJ, 103, 1159

Massey, P., Holmes, S. 2002, ApJ, 580, L35

Mateo, M. L. 1998, ARA&A, 36, 435

Mathewson, D. S., Ford, V. L., Dopita, M. A., Tuohy, I. R., Long, K. S., Helfand, D. J. 1983, IAUS, 101, 541

Mayall, N. U. 1935, PASP, 47, 317

Maza, J., & van den Bergh, S. 1976, ApJ, 204, 519

Muxlow, T. (No Date), *Wide-Field Imaging*, (Online), Avaliable: http://www.mpifr-bonn.mpg.de/1041116/Muxlow_WideField.pdf

Nidever, D. L. et al. 2013, ApJL, 779, L15

Pacholczyk, A. G. 1970, *Radio Astrophysics: NonThermal Processes in Galactic and Extragalactic Sources*, San Francisco: W.H. Freeman and Company

Pasham, D. R., Strohmayer, T. E., Mushotzky, R. F. 2013, ApJL, 771, L44

Philips, A.C. 2010, *The Physics of Stars*, 2nd Edition, Chichester: John Wiley & Sons

Porter, A. C., Filppenko, A. V. 1987, AJ, 93, 1372

Prestwich, A. H. et al.2007, ApJ, 669, L21

Rau, U. 2012, *NRAO: Thirteenth Synthesis Imaging Workshop*, (Online), Avaliable: http://www.aoc.nrao.edu/~rurvashi/DataFiles/Talk_TSIW_WideBandImaging.pdf, (02/08/14)

Roberts W. W. 1969, ApJ, 158, 123

Roberts, M. S. 1962, AJ, 67, 431

Saha, A., Hoessel, J. G., Krist, J., Danielson, G. E. 1996, AJ, 111, 197

Sanna, N. et al. 2008, ApJ, 688, L69

Schaeffer, R., Casse, M., Cahen, S. 1987, ApJ, 316, L31

Schroeder, D. V. 1999, *Winter Meeting of the American Association of Physics Teachers*, (Online), Avaliable: http://physics.weber.edu/schroeder/mrr/MRRtalk.html (20/08/14)

Schwab, F. R. 1984, *Indirect Imaging. Measurement and Processing for Indirect Imaging.*, New York: Cambridge University press

Schwab, F. R., Cotton, W. D. 1983, AJ, 88, 688

Searle, L., & Zinn, R. 1978, ApJ, 225, 357

Shklovskii, I. S. 1960, SvA, 4, 243

Shostak, G. S. 1974, A&A, 31, 97

Shostak, G. S., Skillman, E. D. 1989, A&A, 214, 33

Silk, J., & Mamon, G. A. 2012, RAA, 12, 917

Silverman, J. M., Filippenko, A. V. 2008, ApJ, 678, L17

Spyromilio, J. 1994, MNRAS, 266, L61

Steinmetz, M., & Navarro, J. F. 2002, NewA, 7, 155

Swift, L. 1887, AN, 117, 217

Taylor, G. B., Carilli, C. L., Perley, R. A. 1999, *Synthesis Imaging In Radio Astronomy II*, San Francisco: Astronomical Society of the Pacific Conference Series

Tikhonov, N. A., Galazutdinova, O. A. 2009, AstL, 35, 748

Toomre, A. 1964, ApJ, 139, 1217

Vaduvescu, O., McCall, M. L., Richer, M. G. 2007, AJ, 134, 604

Wang, Q. D., Whitaker, K. E., Williams, R. 2005, MNRAS, 362, 1065

Weiler, K. W., Panagia, N., Sramek, R. A., Van Dyk, S. D., Stockdale, C. J., Williams, C. L. 2010, MmSAI, 81, 374

Weiler, K. W., Williams, C. L., Panagia, N., Stockdale, C. J., Kelley, M. T., Sramek, R. A., Van Dyk, S. D., Marcaide, J. M. 2007, ApJ, 671, 1959

Weiler, K.W., Panagia, N., Sramek, R.A. 1990, ApJ, 364, 611

Weisz, D. R. et al. 2014, ApJ, 789, 147

White, R. L., Becker, R. H. 1992, ApJS, 79, 331

Wilcots, E. M., Miller, B. W. 1998, AJ, 116, 2363

Wilson, A. S., Weiler, K. W. 1976, A&A, 49, 357

Wilson, C. D., Welch, D. L., Reid, I. N., Saha, A., Hoessel, J. 1996, AL, 111, 1106

Wilson, T.L., Rohlfs, K., Hüttemeister, S. 2009, *Tools of Radio Astronomy*, 5th Edition, Berlin: Springer-Verlag

Windhorst, R. A. 2003, New Astronomy Reviews, 47, 357

Wrigley, N. 2011, *Estimating the Primary Beam of the e-MERLIN Array in L-Band*, (Online), Avaliable:http://www.radionet-eu.org/fp7wiki/lib/exe/fetch.php?media=na:reporting:emerlin_beam_2011_jan_30_4pm.pdf

Yahil, A., Tammann, G. A., Sandage, A. 1977, ApJ, 217, 903

Yang, H., Skillman, E. D. 1993, AJ, 106, 1448

Yun, M. S., Reddy, N. A., Condon, J. J. 2001, ApJ, 554, 803

Appendix A: Spectral Power Distribution of Bremsstrahlung

The following derivation was taken from the Essential Radio Astronomy Course by the NRAO (**Condon & Ransom 2007**).

Single Electron-Ion Interaction

Consider the radiation emitted when an electron passes by a much more massive ion with charge number Z, where $Z = 1$ for a singly ionized atom like hydrogen. Each electron-ion interaction will generate a single pulse of radiation.
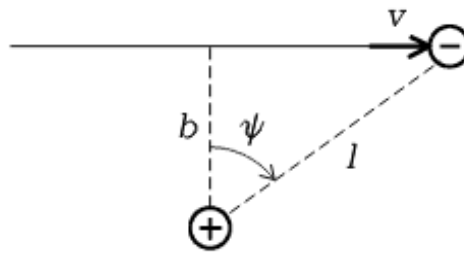
*Figure A.1: Schematic showing an electron pass by a stationary ion. Low energy photons are generated by weak scatterings where the velocity vector changes little. Diagram taken from **Condon & Ransom (2007)**.*

Figure A.1 illustrates this situation where v is the velocity of the particle, l is the separation of the two particles, b is the impact parameter (physically the closest approach between the two particles).

As radio radiation is low energy, we can assume that the path that the electron takes is nearly straight as it interacts with the ion and that the velocity of the electron will stay roughly constant.

The Coulomb force between the two particles is given by:

$$F_c = m_e \dot{v} = \frac{Ze^2}{4\pi\varepsilon_0 l^2}$$

The electron will be accelerated both parallel and perpendicular to the direction that the electron is travelling in. These can be found from the geometry of the above diagram:

$$F_\parallel = m_e \dot{v}_\parallel = \frac{Ze^2}{4\pi\varepsilon_0 l^2} \sin\psi = \frac{Ze^2}{4\pi\varepsilon_0 b^2} \sin\psi \cos^2\psi$$

$$F_\perp = m_e \dot{v}_\perp = \frac{Ze^2}{4\pi\varepsilon_0 l^2} \cos\psi = \frac{Ze^2}{4\pi\varepsilon_0 b^2} \cos^3\psi$$

As Larmor radiation at large distances depends almost entirely on the perpendicular component of the electric field at large distances, we only need to consider the

perpendicular acceleration between the two particles. Therefore the power from the interaction using Larmor's equation is given by:

$$P = \frac{e^2 \dot{v}_\perp{}^2}{6\pi\varepsilon_0 c^3} = \frac{e^2}{6\pi\varepsilon_0 c^3}\left(\frac{Ze^2\cos^3\psi}{4\pi\varepsilon_0 m_e b^2}\right)^2$$

The total energy, W, emitted by the pulse is therefore:

$$W = \int_{-\infty}^{\infty} P \; dt = \frac{Z^2 e^6}{96\pi^3\varepsilon_0{}^3 c^3 m_e{}^2 b^4}\int_{-\infty}^{\infty}\cos^6\psi \; dt$$

In order to solve this integral, it is necessary to change the variables to ψ. From the interaction diagram it can be seen that:

$$v = \frac{dx}{dt}$$

and:

$$\tan\psi = \frac{x}{b}$$

It can therefore be shown that:

$$dt = \frac{bd\psi}{v\cos^2\psi}$$

Using this and using the symmetry of even functions yields:

$$W = \frac{Z^2 e^6}{48\pi^3\varepsilon_0{}^3 c^3 m_e{}^2 b^3 v}\int_{0}^{\frac{\pi}{2}}\cos^4\psi \; d\psi$$

This can be evaluated to give the power emitted from a single electron-ion interaction characterized by the impact parameter, b, and the velocity, v:

$$W = \frac{Z^2 e^6}{256\pi^2\varepsilon_0{}^3 c^3 m_e{}^2}\left(\frac{1}{b^3 v}\right)$$

The pulse of radiation is emitted over a time roughly equal to the collision time in the above interaction, $\tau \approx \frac{b}{v}$. The power spectrum associated with this pulse is roughly flat over all frequencies up until a cut-off frequency, $v_{max} \approx \frac{v}{2\pi b}$ and then falls at higher frequencies. The power spectrum of a pulse is the Fourier transform of the pulse timescale. In this case, the pulse is short and therefore the power spectrum is very broad. All of the radio emission from this interaction lies within this flat range.

We can make the approximation that the power spectrum of such a pulse is flat up until $v_{max} = v$ and is zero at higher frequencies. The average power per unit frequency can be written as:

$$W_\nu \approx \frac{W}{\nu_{max}} = \frac{Z^2 e^6}{128\pi\varepsilon_0{}^3 c^3 m_e{}^2}\left(\frac{1}{b^2 v^2}\right)$$

So far we have only considered the interaction between a single electron-ion interaction. Now we need to find the distributions for v and b to evaluate the radio emission from an ionized plasma.

For Multiple Electron-Ion Interactions

In Local Thermodynamic Equilibrium (LTE), the average kinetic energies of the electrons and ions is equal, as electrons have much less mass than the ions, their speeds are much higher. The ions are essentially stationary during the interaction.
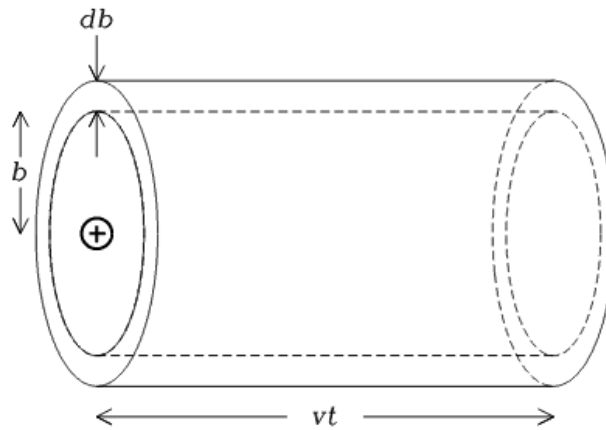
*Figure A.2: Schematic showing the geometry used to work out the number of electrons passing close to an ion. Diagram taken from **Condon & Ransom (2007)**.*

The number of electrons with speed between v and $v + dv$ passing a stationary ion within the impact parameter range b and $b + db$ during the time interval t is equal to the number of electrons within this cylindrical shell (see **Figure A.2**), which is given by:

$$N_e(2\pi b\, db)vf(v)dv$$

where N_e is the number density of electrons and $f(v)$ is the speed distribution of the electrons.

The total number of encounters per unit volume per unit time is simply this number multiplied by the number of ions in the unit volume, N_i:

$$N(v,b)dv\, db = (2\pi b\, db)vf(v)dv\, N_e N_i$$

The spectral power emitted at a frequency, ν, will be $4\pi\varepsilon_\nu$, where ε_ν is the emission co-efficient from radiative transfer. Therefore:

$$4\pi\varepsilon_\nu = \int_{b=0}^{\infty}\int_{v=0}^{\infty} W_\nu(v,b)N(v,b)dv\, db$$

After substituting in the values already derived for W_ν and N, we arrive at this expression:

$$4\pi\varepsilon_v = \frac{Z^2 e^6 N_e N_i}{64\varepsilon_0{}^3 c^3 m_e{}^2} \int_{v=0}^{\infty} \frac{f(v)}{v} dv \int_{b=0}^{\infty} \frac{db}{b}$$

Velocity Distribution

To start we can solve the velocity dependent interegral. As the plasma is in LTE, we can assume that the electrons follow a non-relativistic Maxwellian velocity distribution:

$$f(v) = \frac{4v^2}{\sqrt{\pi}} \left(\frac{m}{2kT}\right)^{\frac{3}{2}} \exp\left(-\frac{mv^2}{2kT}\right)$$

The integral can be solved to find:

$$\int_{v=0}^{\infty} \frac{f(v)}{v} dv = \left(\frac{2m_e}{\pi kT}\right)^{\frac{1}{2}}$$

Here is where the thermal dependence of this type of radiation comes in as the velocity distribution depends on the temperature of the gas.

Impact Parameter Range

The solution for the impact parameter integral is harder to find as this integral diverges, therefore limits must be set on the values of the impact parameter.

$$\int_{b_{min}}^{b_{max}} \frac{db}{b} = \ln\left(\frac{b_{max}}{b_{min}}\right)$$

In order to find b_{min}, we consider the net momentum impulse:

$$\Delta P = \int_{-\infty}^{\infty} F \, dt = \int_{-\infty}^{\infty} eE \, dt$$

using $E_\perp = E \cos\psi$ (the parallel component is antisymetric about the origin), the equation changes to:

$$\Delta P = Ze^2 \int_{-\infty}^{\infty} \frac{\cos^3\psi}{b^2} \, dt$$

Using the same substitution as earlier, the integral changes to:

$$\Delta P = \frac{Ze^2}{bv} \int_{\frac{\pi}{2}}^{\frac{\pi}{2}} \cos\psi \, d\psi = \frac{2Ze^2}{bv}$$

The maximum momentum transfer during the interaction is when the electron bounces back from the charged ion. This has a momentum change of twice the initial momentum of the electron, so equating and rearranging for b yields:

$$b_{min} \approx \frac{Ze^2}{m_e v^2} \approx \frac{Ze^2}{3kT}$$

This is a purely classical way of finding the closest approach. From quantum mechanics, the uncertainty principle also implies a limit which is much lower than this classical limit. But this will only need to be taken into account in an extremely cold plasma.

To find the estimate for the maximum value the impact parameter can take is to consider the largest value of b that can generate a significant amount of power at a relevant frequency. From the power spectrum of a single pulse, the power drops after the frequency $v \approx \frac{v}{2\pi b}$. Therefore the maximum value for b is:

$$b_{max} \approx \frac{v}{2\pi v} \approx \left(\frac{3kT}{m_e}\right)^{\frac{1}{2}} \frac{1}{2\pi v}$$

The ratio of b_{max} to b_{min} is approximately:

$$\frac{b_{max}}{b_{min}} \approx \left(\frac{3kT}{m_e}\right)^{\frac{3}{2}} \frac{m_e}{2\pi Z e^2 v}$$

Constructing a Spectrum

Finally, we can bring these all together to find the free-free emission coefficient:

$$\varepsilon_v = \frac{Z^2 e^6 N_e N_i}{256\pi\varepsilon_0{}^3 c^3 m_e{}^2}\left(\frac{2m_e}{\pi kT}\right)^{\frac{1}{2}} \ln\left(\frac{b_{max}}{b_{min}}\right)$$

As the gas is in LTE, we can use Kirchhoff's law to find the absorption coefficient using the blackbody brightness law:

$$\kappa_v = \frac{\varepsilon_v}{B(T)}$$

At low frequencies, using the Rayleigh-Jeans approximation, this can be written as:

$$\kappa_v = \frac{\varepsilon_v c^2}{2kT v^2} = \frac{1}{v^2 T^{\frac{3}{2}}}\left[\frac{Z^2 e^6}{\varepsilon_0{}^3 c}N_e N_i \frac{1}{\sqrt{(\pi m_e k)^3}}\right]\frac{\sqrt{2}}{512}\ln\left(\frac{b_{max}}{b_{min}}\right)$$

Because the ratio of b_{max} to b_{min} also depends of frequency, the absorption coefficient is proportional to $v^{-2.1}$ and not just v^{-2}.

To find the total opacity, τ_v, we need to integrate κ_v over the line of sight:

$$\tau_v = \int -\kappa_v ds \propto \int \frac{N_e N_i}{v^{2.1}T^{\frac{3}{2}}} ds$$

At low frequencies, the optical depth increases and the ionized plasma behaves like a blackbody with a spectral index of α≈2. At higher frequencies, the optical depth drops and the plasma becomes transparent.

From radiative transport (**Brinks 1990**), the flux density per unit frequency can be written as:

$$S_\nu \propto \frac{2kT\nu^2}{c^2} \tau_\nu \propto \nu^{-0.1} T^{-\frac{1}{2}}$$

That is, at higher frequencies, the plasma will have a spectral index of α≈-0.1. This is a very important result that can be used for classifying emission in the radio spectrum. This spectrum is also dependent on the temperature of the plasma.

Figure A.3 shows a log-log plot of the spectrum. At lower frequencies, the plasma behaves like a blackbody. This area of the spectrum is not normally used in astronomy because of the high optical depth at low frequencies. At higher frequencies, the spectrum has a much flatter spectrum .
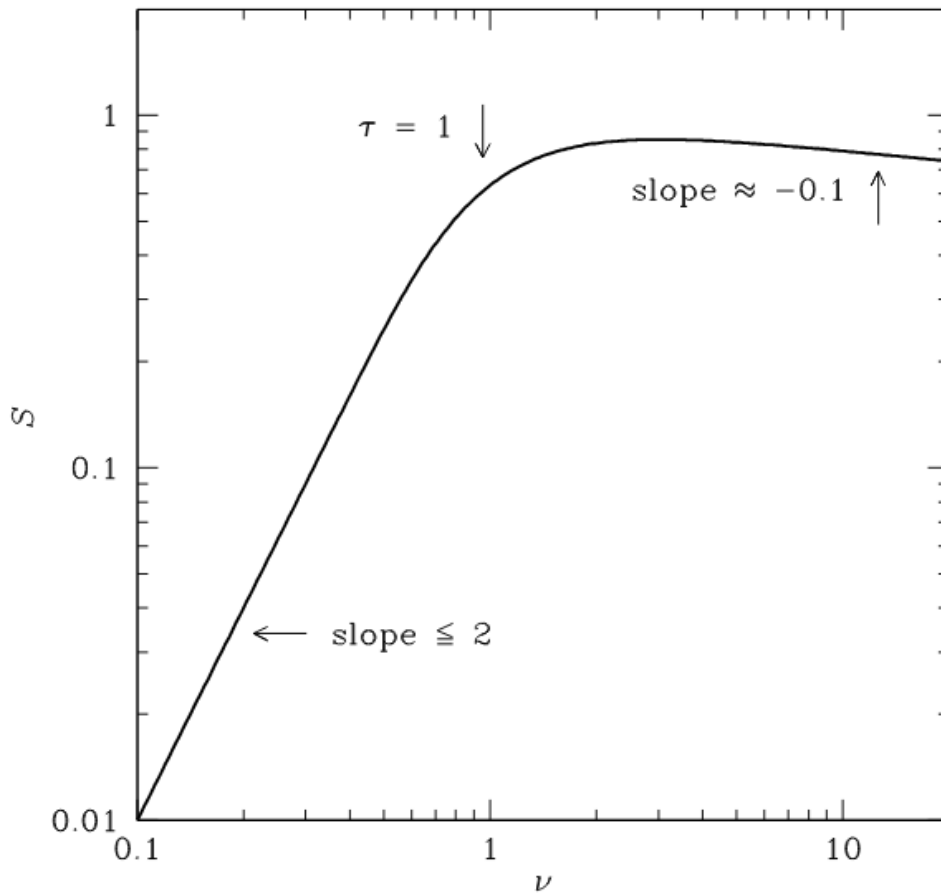
*Figure A.3: Diagram showing the radio spectrum for a HII region. At low frequencies, it behaves like a blackbody with a spectral index α ≈ 2. At the frequency where the optical depth approaches 1, the function turns over to a spectral index of α − 0.1. Diagram was taken from **Condon & Ransom (2007)**.*

Appendix B: Spectral Power Distribution of Synchrotron Emission

The following derivation was primarily taken from the Essential Radio Astronomy course by the NRAO (**Condon & Ransom 2007**), with other sources being cited as they arise.

Motion of a Charged Particle in a Uniform Magnetic Field

This section of the derivation was adapted from **Longair (pg 161-162)**.

First we need to find the motion of a charged particle in a magnetic field. Consider the simple case of a charged particle of rest mass m_0, charge number Z, and a velocity $\boldsymbol{v}$, travelling in a uniform magnetic field $\boldsymbol{B}$ (see **Figure B.1**). The bold font signifies a vector quantity.
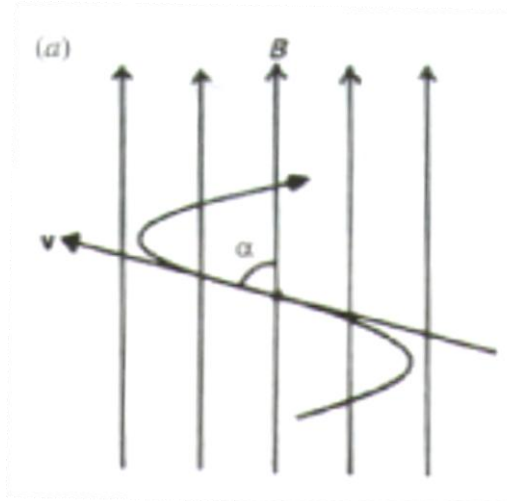
Figure B.1: A simplified schematic of the motion of a charged particle through a magnetic field, taken from Longair pg 194 . Here the velocity vector **v** and the magnetic field vector **B** are shown along with the pitch angle α. As the particle travels through the magnetic field, it follows a helical path following the direction of the magnetic field.

The motion of the charged particle can be found by equating Newton's second law to the Lorentz force law. Newton's second law is given by:

$$\boldsymbol{F} = \frac{d\boldsymbol{p}}{dt} = m_0 \boldsymbol{a}$$

Where $\boldsymbol{p}$ is the momentum of the charged particle, m_0 is the rest mass of the particle and $\boldsymbol{a}$ is the acceleration that it experiences. As we are dealing with a particle moving at relativistic speeds, it is necessary to use relativistic momentum which is given by:

$$\boldsymbol{p} = \gamma m_0 \boldsymbol{v}$$

Where γ is the Lorentz factor (see Appendix C). Substituting this into Newton's second law yields:

$$F = \frac{d\boldsymbol{p}}{dt} = \gamma m_0 \frac{d\boldsymbol{v}}{dt} + \frac{m_0 \boldsymbol{v}}{c^2} \gamma^3 \left(\boldsymbol{v} \cdot \frac{d\boldsymbol{v}}{dt} \right)$$

The Lorentz force law is given by:

$$F = Ze(\boldsymbol{v} \times \boldsymbol{B})$$

Where e is the charge on an electron. Equating this to the Lorentz force law yields:

$$\gamma m_0 \frac{d\boldsymbol{v}}{dt} + \frac{m_0 \boldsymbol{v}}{c^2} \gamma^3 \left(\boldsymbol{v} \cdot \frac{d\boldsymbol{v}}{dt} \right) = Ze(\boldsymbol{v} \times \boldsymbol{B})$$

From the cross product, we see that the force exerted on the charged particle perpendicular to the velocity vector $\boldsymbol{v}$. Therefore the dot product in the above equation becomes 0. The equation simplifies to:

$$\gamma m_0 \frac{d\boldsymbol{v}}{dt} = Ze(\boldsymbol{v} \times \boldsymbol{B})$$

We can expand the vector cross product and rearrange for a formula for the acceleration of the particle:

$$\frac{d\boldsymbol{v}}{dt} = a_\perp = \frac{Ze|\boldsymbol{v}||\boldsymbol{B}|\sin\alpha}{\gamma m_0}$$

α is the pitch angle between the velocity vector, $\boldsymbol{v}$, and the magnetic field vector, $\boldsymbol{B}$ (see **Figure B.1**) and $a_\perp$ is the acceleration, which is perpendicular to the magnetic field and the velocity vector.

The charged particle will follow a circular path dictated by the velocity component perpendicular to the magnetic field, but the velocity component parallel to the magnetic field will not change. Therefore the charged particle will follow a helical path in the direction of the magnetic field vector. We can equate the perpendicular acceleration to centripetal acceleration associated with a circular path:

$$a_\perp = \frac{v_\perp^2}{r} = \frac{Ze|\boldsymbol{v}||\boldsymbol{B}|\sin\alpha}{\gamma m_0}$$

Where $v_\perp$ is the component of the velocity vector perpendicular to the magnetic field and r is the radius of the circular path that the charged particle takes.

From this equation, the relativistic gyro-radius, r_G, relativistic angular gyro-frequency, ω_G, and the relativistic gyro-frequency, v_G, can be found and are given by:

$$r_G = \frac{\gamma m_0 |\boldsymbol{v}| \sin\alpha}{Ze|\boldsymbol{B}|}$$

$$\omega_G = \frac{Ze|\boldsymbol{B}|}{\gamma m_0}$$

$$v_G = \frac{Ze|\boldsymbol{B}|}{2\pi\gamma m_0}$$

90

Equivalently for a non-relativistic particle, the gyro-radius, r_B, the angular gyro-frequency, ω_B, and gyro-frequency, ν_B, are given by:

$$r_B = \frac{m_0 |\boldsymbol{v}| \sin \alpha}{Ze|\boldsymbol{B}|} = \gamma r_G$$

$$\omega_B = \frac{Ze|\boldsymbol{B}|}{m_0} = \frac{\omega_G}{\gamma}$$

$$\nu_B = \frac{Ze|\boldsymbol{B}|}{2\pi m_0} = \frac{\nu_G}{\gamma}$$

Power Emitted From an Electron Moving Within A Magnetic Field

Now that the motion of the particle has been determined, we can find the power emitted through this motion by using the Larmor equation. We will use an electron for the following calculations, $Z = 1$ and $m_0 = m_e$.

The Larmor equation is only valid in inertial frames where the charged particle's velocity is much lower than the speed of light. To find the results in other inertial frames, the results need to be transformed through a Lorentz transform. Using primed co-ordinates to describe an inertial frame where the electron is nearly at rest, the Larmor equation is given by:

$$P' = \frac{e(a_\perp')^2}{6\pi\varepsilon_0 c^3}$$

Where P' is the total power emitted in the charged particles frame of reference, ε_0 is the permittivity of free space and $a_\perp'$ is the perpendicular acceleration in the charged particle's frame of reference. The conversion factor to transform the acceleration to the observers frame is:

$$a_\perp = \frac{a_\perp'}{\gamma^2}$$

Therefore the Larmor equation changes to:

$$P' = \frac{ea_\perp{}^2\gamma^4}{6\pi\varepsilon_0 c^3}$$

The next step is to transform from P' to P. It turns out that the power is the same in all frames of reference (see Appendix C). Therefore the power observed is given by:

$$P = \frac{ea_\perp{}^2\gamma^4}{6\pi\varepsilon_0 c^3} = \frac{e\gamma^4}{6\pi\varepsilon_0 c^3}\left(\frac{e|\boldsymbol{v}||\boldsymbol{B}|\sin\alpha}{\gamma m_e}\right)^2$$

This can be rewritten using the Thompson cross section σ_T, the magnetic energy density, U_{mag} and the beta factor, β, each given by:

$$\sigma_{\mathrm{T}} = \frac{e^4}{6\pi\varepsilon_0{}^2 c^4 m_e{}^3}$$

$$U_{mag} = \frac{B^2}{2\mu_0}$$

$$\beta = \frac{v}{c}$$

Using these substitutions lead to:

$$P = 2\sigma_{\mathrm{T}}c\beta^2 U_{mag}\gamma^2 \sin^2\alpha$$

High energy relativistic electrons in radio sources can have lifetimes of thousands of years before losing their ultra-relativistic energies, lower energy relativistic electrons can have much longer lifetimes. They are scattered repeatedly by magnetic field fluctuations and charged particles in the environment and the distribution of pitch angles gradually becomes random. It is therefore useful to find the average synchrotron power $\langle P \rangle$ per electron in an ensemble of electrons with the same Lorentz factor γ but random pitch angles. This is given by:

$$\langle P \rangle = 2\sigma_{\mathrm{T}}c\beta^2 U_{mag}\gamma^2 \langle\sin^2\alpha\rangle$$

The average value of $\sin^2\alpha$ is $\frac{2}{3}$. Therefore the average synchrotron power emitted by a relativistic electron is:

$$\langle P \rangle = \frac{4}{3}\sigma_{\mathrm{T}}c\beta^2 U_{mag}\gamma^2$$

Synchrotron Spectrum of a Single Electron

To find the synchrotron spectrum from a single electron, we must first consider the angular distribution of the radiation in the observers frame. Unfortunately due to the relativistic nature of the system, this is no easy task. Relativistic aberration causes the radiation to be beamed in the direction of motion in the observers frame (see **Figure B.2**).

*Figure B.2: A visualisation of the relativistic aberration of a particle travelling to the left at relativistic speeds compared to the power pattern from Larmor radiation. The dashed line represents the power pattern in the electron's frame of reference and is that of a simple dipole associated with Larmor radiation. The solid line represents the power pattern observed in an observer's inertial frame. Diagram taken from **Condon & Ransom (2007)**.*

From the Lorentz transforms we can find the directional transformation factors for an electron moving in the x direction. Again the prime notation refers to the electron's frame of reference. The velocity in the observer's frame of reference is given by:

$$v_x = \frac{v_x' + v}{1 + \frac{\beta v_x'}{c}}$$

$$v_y = \frac{v_y'}{\gamma\left(1 + \frac{\beta v_x'}{c}\right)}$$

If we consider synchrotron photons emitted with speed c at an angle θ' from the x' axis, we can find the x' and y' projections of the photons speed on the x' and y' axis:

$$\cos\theta' = \frac{v_x'}{c}$$

$$\sin\theta' = \frac{v_y'}{c}$$

For the observer's frame, for the same photons we have:

$$\cos\theta = \frac{v_x}{c}$$

$$\sin\theta = \frac{v_y}{c}$$

Combing the transformation equations with the projections yields:

$$\cos\theta = \frac{\cos\theta' + \beta}{1 + \beta\cos\theta'}$$

$$\sin\theta = \frac{\sin\theta'}{\gamma(1 + \beta\cos\theta')}$$

In the electron's frame, the Larmor equation predicts a power pattern that is proportional to $\cos^2\theta'$ which are zero at $\theta' = \pm\frac{\pi}{2}$. In the observer's frame, the zeros are transformed to much smaller angles:

$$\sin\theta = \frac{\sin\theta'}{\gamma(1 + \beta\cos\theta')} \approx \frac{1}{\gamma} \approx \theta$$

At speeds close to the speed of light, the angle gets confined to a very narrow beam, within the angle $\frac{2}{\gamma}$.

The observer will only see a short pulse of radiation, emitted when the electron is moving directly towards the observer. This can be expressed as a fraction of the orbit as:

$$\frac{2}{2\pi\gamma} = \frac{1}{\pi\gamma}$$

The duration of the observed pulse is shorter than the time the electron needs to cover this fraction of the orbit. This is because the electron is only visible when it is moving directly

towards the observer with a speed approaching c. In the observer's frame, the electron almost keeps up with the radiation it is emitting.
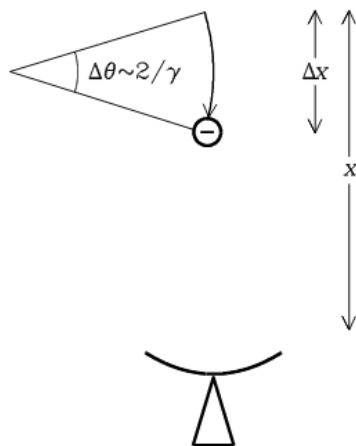
Figure B.3: Schematic showing the geometry of an observer watching the electron spiral around the magnetic field at a distance x. The beamed radiation pattern will sweep past the observer but will only be observable within the angle $\frac{2}{\gamma}$. In this diagram, the electron will travel a distance Δx towards the observer whilst it is observable. Diagram taken from **Condon & Ransom (2007)**.

The pulse time, Δt_p, is found by subtracting the time taken from the end of the observed pulse from the start of the observed pulse. From the **Figure B.3** it can be found to be:

$$\Delta t_p = \frac{\Delta x}{v} + \frac{(x - \Delta x)}{c} - \frac{x}{c} = \frac{\Delta x}{v}\left(1 - \frac{v}{c}\right)$$

Where the first term represents the time taken by the electron to cover the distance Δx, the second term is the light travel time from the electron position at the end of the pulse and the third is the light travel time from the electron at the beginning of the pulse. The pulse time is a factor of $\left(1 - \frac{v}{c}\right)$ slower than the time it takes for the electron to travel the distance Δx. The faster the electron is travelling, the stronger this factor becomes.

In the relativistic limit as $v \to c$:

$$\left(1 - \frac{v}{c}\right) = \left(1 - \frac{v}{c}\right)\frac{1 + \frac{v}{c}}{1 + \frac{v}{c}} = \frac{1 - \frac{v^2}{c^2}}{1 + \frac{v}{c}} \approx \frac{1}{2\gamma^2}$$

Therefore the time for the observed pulse changes to:

$$\Delta t_p = \frac{\Delta x}{v}\frac{1}{2\gamma^2} = \frac{\Delta \theta}{\omega_B}\frac{1}{2\gamma^2} = \frac{1}{\gamma^3 \omega_B} = \frac{1}{\gamma^2 \omega_G}$$

If we allow for the motion of the electron parallel to the magnetic field, we can replace the total magnetic field with is perpendicular component, $B \sin \alpha$. Therefore the final expression for the pulse time is:

$$\Delta t_p = \frac{1}{\gamma^2 \omega_G \sin \alpha}$$

As the electron is rotating around the magnetic field, the power received as a function of time is a very spiky pattern of spaced narrow pulses (see **Figure B.4**). To find the power spectrum, we need to take a Fourier transform of these pulses.
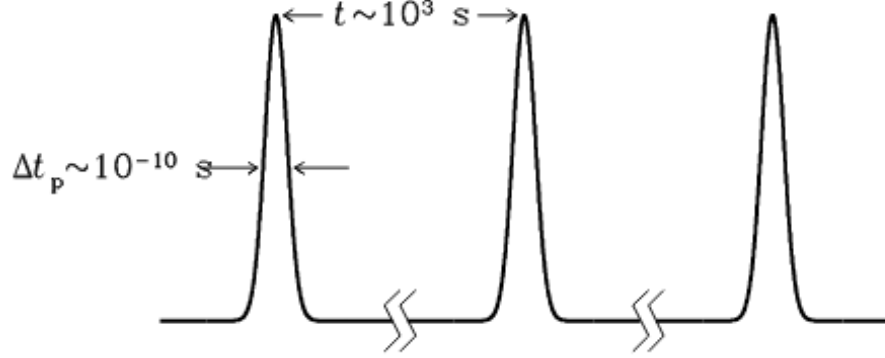
Figure B.4: *Diagram showing the power as a function of time. Each spike corresponds to when the electron is travelling towards the observer. These spikes will occur with a frequency equal to the relativistic gyro-frequency, ν_G. Diagram taken from* **Condon & Ransom (2007)** .

We can take a short cut in calculating the Fourier transform by noting that the pulse train is a convolution of the profile of an individual pulse with a Shah function (see **pg 577 of Bracewell**). The Shah function is a series of evenly spaced delta functions and is given by:

$$III(^t/_{\Delta t}) = \sum_{n=-\infty}^{\infty} \delta[(^t/_{\Delta t}) - n]$$

From the convolution theorem, the Fourier transform of the pulse train is equal to the Fourier transform of one pulse multiplied by the Fourier transform of the Shah function.

As the pulses are spaced relatively widely apart, the Fourier transform reveals a continuous, flat spectrum. The spectrum is flat at low frequencies and tapers off at frequencies above ν_{max} due to the Fourier nature of this calculation. ν_{max} is given by:

$$\nu_{max} \approx \frac{1}{2\Delta t_p} \approx \pi \gamma^2 \nu_G \sin \alpha$$

After a lengthy calculation, the synchrotron power spectrum for a single electron comes out as:

$$P(\nu) = \frac{\sqrt{3}e^3 B \sin \alpha}{m_e c^2} \left(\frac{\nu}{\nu_c}\right) \int_{\nu/\nu_c}^{\infty} K_{5/3}(\eta)d\eta$$

where $K_{5/3}$ is a modified Bessel function and ν_c is the critical frequency which is given by:

$$\nu_c = \frac{3}{2}\gamma^2 \nu_G \sin \alpha$$

95

The spectrum is plotted in **Figure B.5**. For a full mathematical derivation see **pg 77-86 of Pacholczyk**.
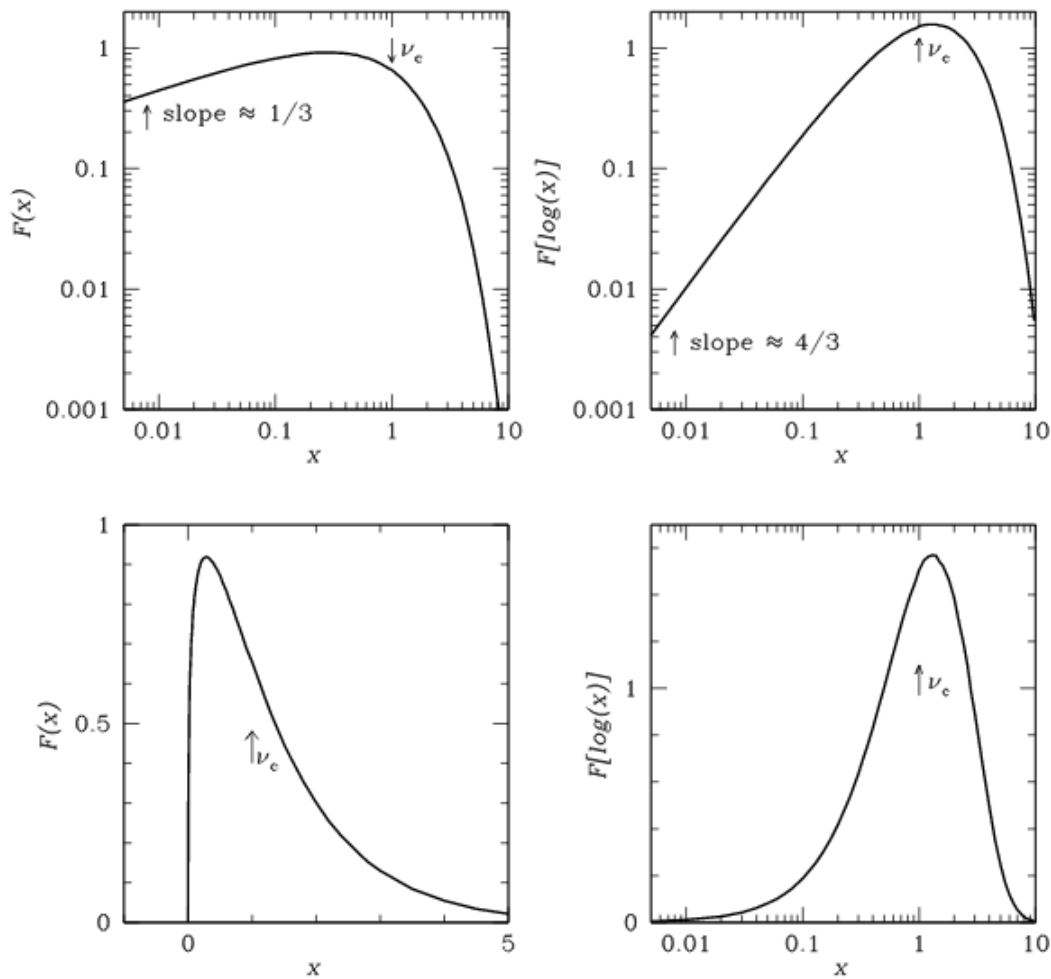
Figure B.5: *Here are four ways to plot the synchrotron spectrum in terms of $F(x) = x \int_x^\infty K_{5/3}(\eta)d\eta$. The lower left panel shows the spectrum plotted on linear axis, the upper left diagram shows the spectrum plotted on a logarithmic scale, the power per unit $\log x$ is plotted on a logarithmic axis and the lower right diagram shows the power per unit $\log x$ plotted on a linear axis. Each diagram reveals different information about the source. On the linear diagram, the low frequency area is obscured. Re-plotting on a logarithmic axis reveals more information about the low frequency area but does not make it clear that most of the power is emitted at $x \approx 1$. The power per unit $\log x$ plotted on a logarithmic axis diagram makes it clear that most of the power is emitted at $x \approx 1$. The final diagram shows that there is a significant amount of emission at low frequencies which is lost in the linear diagram.*

The spectrum of a single electron has a logarithmic slope $\approx \frac{1}{3}$ at low frequencies, a broad peak near the critical frequency and falls sharply at high frequencies. The areas under the curves in the two lower diagrams are proportional to the power radiated in a given frequency range. Together they show that about half of the power is radiated at frequencies lower than the critical frequency and about half is emitted at frequencies higher than the critical frequency.

Synchrotron Spectrum from an Ensemble of Electrons

Now that we have the power spectrum for a single electron, we can find the power spectrum from a distribution of electrons. If we make the rough approximation that each electron radiates all of its power at a single frequency close to the critical frequency, then the emission coefficient of synchrotron radiation from an ensemble of electrons is:

$$\varepsilon_\nu d\nu = -\frac{dE}{dt} N(E) dE$$

Where ε_ν is the frequency dependent emission coefficient and $N(E)$ is the number of electrons per unit volume with energies between E and $E + dE$. As this is a non-thermal process, the energy distribution of the ensemble of electrons can be approximated roughly by a power law:

$$N(E) dE \approx k E^{-\delta} dE$$

Where E is the energy of the electrons, k is a constant and δ is the injection spectrum slope.

The energy is given by:

$$E = \gamma m_e c^2 \approx \left(\frac{\nu}{\nu_G}\right)^{\frac{1}{2}} m_e c^2$$

And differentiating with respect to frequency yields:

$$\frac{dE}{d\nu} \approx \frac{m_e c^2}{2\nu_G^{\frac{1}{2}}} \nu^{-\frac{1}{2}}$$

Substituting the average power per electron as well as the above equations into the equation for the emission co-efficient yields:

$$\varepsilon_\nu \approx \left(\frac{4}{3}\sigma_T c \beta^2 U_{mag} \gamma^2\right)\left(k E^{-\delta}\right)\left(\frac{m_e c^2}{2\nu_G^{\frac{1}{2}}} \nu^{-\frac{1}{2}}\right)$$

We can eliminate all energy terms in the above equation in terms of $\left(\frac{\nu}{\nu_G}\right)$ and ignore the constants, resulting in the proportionality:

$$\varepsilon_\nu \propto \left(\frac{\nu}{\nu_G}\right) B^2 \left(\frac{\nu}{\nu_G}\right)^{\frac{-\delta}{2}} (\nu\nu_G)^{-\frac{1}{2}}$$

As $\nu_G \propto B$, we eventually arrive at:

$$\varepsilon_\nu \propto B^{\frac{\delta+1}{2}} \nu^{\frac{1-\delta}{2}}$$

Hence the spectral index of a synchrotron source is:

$$\alpha = \frac{1 - \delta}{2}$$

That is, the spectral index depends on the initial energy spectrum of the electrons. The magnetic field also plays a part in determining the power spectrum from an ensemble of electrons and this too depends on the initial energy spectrum of the electrons.

$$\alpha = \frac{1 - \delta}{2}$$

Appendix C: Lorentz Transformations

The Lorentz transformations are equations that transfer to different frames of reference whilst keeping the speed of light, c, constant in all frames. The following was taken from the NRAO Essential Radio Astronomy Course (**Condon & Ransom 2007**).

Assuming that the laws of physics are the same in all inertial frames, we consider two inertial co-ordinate frames S and S'. S is at rest and S' is moving with a constant velocity, v, along the common x axis. We can set zero points on clocks so that $t = t' = 0$ at the instant $x = x'$. Therefore (x, y, z, t) might be co-ordinates in the rest frame of an observer and (x', y', z', t') for an inertial frame moving with the instantaneous velocity of a particle.
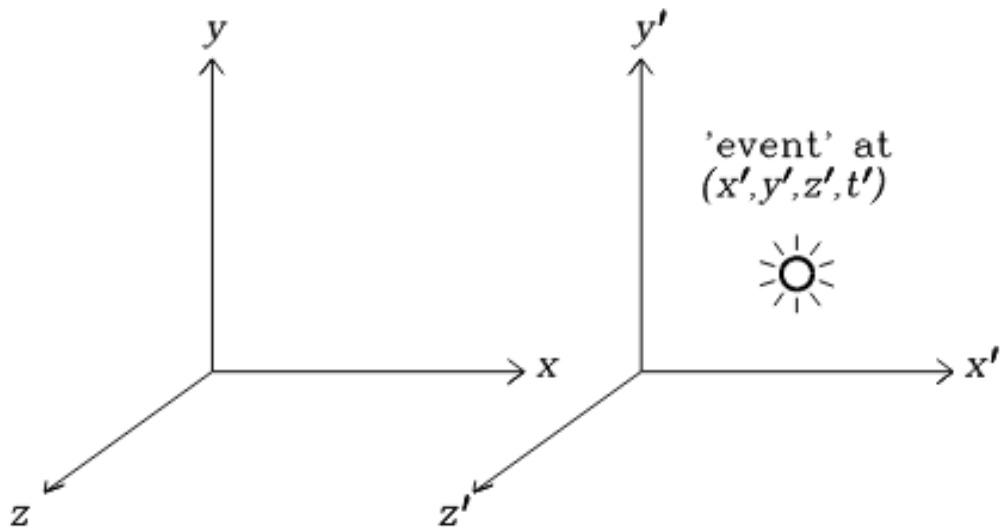
*Figure C.1: Diagram showing the co-ordinate systems used in the Lorentz transform. Taken from **Condon & Ransom (2007)**.*

For a particle moving in the positive x direction, the transformation equations from the moving frame to the stationary frame are given by:

$$x = \gamma(x' + vt')$$

$$y = y'$$

$$z = z'$$

$$t = \gamma\left(t' + \frac{\beta x'}{c}\right)$$

Where the prime notation represents the measurements in the moving frame (stationary with respect to the particle) and the un-primed represents the measurements in the stationary (observers) frame. γ is the Lorentz factor which is given by:

$$\gamma = \frac{1}{\sqrt{1 - \frac{v^2}{c^2}}}$$

and the factor β is given by:

$$\beta = \frac{v}{c}$$

Power Invariance

The power radiated by a moving particle can be found by using the Lorentz transformation equations. If we imaging two electrons of mass m_e, one at rest in the un-primed frame and the other at rest in the primed frame. If one of the electrons is displaced on the y-axis, the electrons will interact as they pass each other and each accelerate in the $\pm y$ direction. The observers will see each electron move in the y direction but the electron in the primed reference frame will move a factor of γ slower. Invoking momentum conservation, the observers conclude that the electron in the primed frame has a factor of γ more energy than the un-primed electron, i.e.:

$$E = \gamma E'$$

Therefore the power from the electron can be written as:

$$P = \frac{dE}{dt} = \frac{dE}{dt'}\frac{dt'}{dt} = \frac{dE}{dE'}\frac{dE'}{dt'}\frac{dt'}{dt} = \gamma P'\frac{1}{\gamma} = P'$$

This reveals that the power emitted is the same in all frames regardless of the velocity of the moving frame. Hence the power is known as Lorentz invariant.